Defra/Environment Agency
Flood and Coastal Defence R&D Programme

Integrated Research Results on Hydrobiosedimentary Processes in Estuaries

Final Report of the Estuary Process Research Project (EstProc): Algorithms and Scientific Information

R&D Technical Report FD1905/TR3



Environment Agency

defra
Department for Environment Food and Rural Affairs

Defra / Environment Agency
Flood and Coastal Defence R&D Programme

Integrated Research Results on Hydrobiosedimentary Processes in Estuaries

Final Report of the Estuary Process Research Project (EstProc): Algorithms and Scientific Information

R&D Technical Report FD1905/TR3

Authors: Estuary Process Consortium for the Fluvial, Estuarine and Coastal Processes Theme:

Produced January 2006

Statement of use
This report provides information for Defra, the Environment Agency and their consultants about estuarine processes and constitutes an R&D output from the Joint Defra / Environment Agency Flood and Coastal Erosion R&D Programme. It is intended for use by experienced modellers who are able to exercise judgement on the applicability of the work to specific situations. Reliance on the information in this report is not a substitute for the necessary expertise or site specific studies and investigations. This report is a contribution to research generally and it would be imprudent for third parties to rely on it in specific applications without first checking its suitability. Various sections of this report rely on data supplied or drawn from third party sources. The members of the EstProc Consortium accept no liability for loss or damage suffered by Defra or the Environment Agency or third parties as a result of errors or inaccuracies in such third party data.

Dissemination status
Internal: Released internally
External: Released to public domain

Keywords: estuary, geomorphology, sedimentary processes

Research contractor: Richard Whitehouse, HR Wallingford HR Wallingford Ltd, Howbery Park, Wallingford, Oxon, OX10 8BA, UK Direct dial: +44 (0)1491 822434 e-mail: r.whitehouse@hrwallingford.co.uk

Project Officer: Jonathan Rogers, Mouchel Parkman.

Publishing organisation
Defra – Flood Management Division
Ergon House,
Horseferry Road
London SW1P 2AL
Tel: 020 7238 3000 Fax: 020 7238 6187
www.defra.gov.uk/environ/fcd

Published by the Department for Environment, Food and Rural Affairs. Printed in the UK, March 2006 on recycled material containing 80% post-consumer waste and 20% totally chlorine-free virgin pulp.

PB No. 11546

Collaboration Statement

The report was prepared by the EstProc Consortium comprising: HR Wallingford (lead), Proudman Oceanographic Laboratory, Professor Keith Dyer / University of Plymouth, St Andrews University, Gatty Marine Laboratory (Sediment Ecology Research Group), ABP marine environmental research, WL | Delft Hydraulics, Plymouth Marine Laboratory, University of Cambridge, Cambridge Coastal Research Unit, University of Southampton, School of Ocean and Earth Sciences, Digital Hydraulics Holland B.V., and Centre for Environment, Fisheries and Aquaculture Science.

SUMMARY

The EstProc project has delivered fundamental new research on estuarine hydrodynamics, sedimentology and ecological processes. More than 30 algorithms are presented under one of the following 9 headings. Each one is denoted with a reference code, EP1 through EP30, and some are subdivided further. In summary:

- Modelling of waves in estuaries contains algorithms EP1 to EP6
- Prediction of the impact of extreme events and major anthropogenic influences contains algorithms EP7 to EP9
- Results obtained from the interrogation of data contains algorithms EP10 to EP12
- Representation of near bed stresses contains algorithms EP13 to EP15
- Transport of mixed sediments contains algorithm EP16
- Understanding of the sediment transport profile contains algorithms EP17 to EP19
- Understanding of general sedimentary processes contains algorithms EP20 to EP26
- Biological process parameters that effect stability, erodibility and deposition of sediments contains algorithms EP27 to EP29
- Methodology for including effect of biological processes into morphological models contains algorithms EP30 to EP31

The algorithms presented are at two levels of development:

1. Concepts or derivations based on data or theory; and,
2. Concepts or derivations based on data or theory that have been implemented and tested against other data.

In each case the scientific background and range of validity of the algorithm is discussed. Many of these algorithms can be implemented into numerical models. Example applications which have used some of the new algorithms are discussed in the associated EstProc Report FD1905/TR2.

For more information contact the project leader, Dr Richard Whitehouse at HR Wallingford (r.whitehouse@hrwallingford.co.uk or tel: +44 (0)1491 835381), or contact the originating organisation responsible for the individual algorithm.

More information on the project and a copy of this report can be obtained from the website: www.estproc.net or from the Defra website: www.defra.gov.uk

Key reports produced by the project

EstProc Consortium (2002). Estuary Process Research Project (EstProc): Inception Report. Report prepared by the Estuary Process Consortium for the Defra and Environment Agency Joint Flood and Coastal Processes Theme. Report No FD1905/TR1.

EstProc Consortium (2004). Integrated Research Results on Hydrobiosedimentary Processes in Estuaries. Final Report of the Estuary Process Research Project (EstProc). R&D Technical Report prepared by the Estuary Process Consortium for the Fluvial, Estuarine and Coastal Processes Theme. Report No FD1905/TR2 – Synthesis Report.

EstProc Consortium (2004). Integrated Research Results on Hydrobiosedimentary Processes in Estuaries. Final Report of the Estuary Process Research Project (EstProc). R&D Technical Report prepared by the Estuary Process Consortium for the Fluvial, Estuarine and Coastal Processes Theme. Report No FD1905/TR3 – Algorithms and Scientific Information.

EstProc Consortium (2004). Integrated Research Results on Hydrobiosedimentary Processes in Estuaries. Final Report of the Estuary Process Research Project (EstProc). R&D Technical Report prepared by the Estuary Process Consortium for the Fluvial, Estuarine and Coastal Processes Theme. Report No FD1905/TR4 – Metadata Report.

CONTENTS

Appendices

1. INTRODUCTION

The EstProc project FD1905 has delivered fundamental new research on estuarine hydrodynamics, sedimentology and ecological processes. This report has been written by the EstProc Consortium to present the wide range of algorithms produced during the research programme, 2001-2004. It was prepared as part of the deliverable requirements of the Estuary Processes Research Project funded by Defra under contract FD1905 within the Defra and Environment Agency Joint Flood and Coastal Processes Theme. EstProc is one of the ERP2 projects.

Further details of the project are presented in two other reports:

Integrated Research Results on Hydrobiosedimentary Processes in Estuaries
Final Report of the Estuary Process Research Project (EstProc)
R&D Technical Report prepared by the Estuary Process Consortium for the Fluvial, Estuarine and Coastal Processes Theme
Report No FD1905/TR2 – Synthesis Report

- This describes the scientific achievements of the project and presents example applications of the new algorithms.

and

Integrated Research Results on Hydrobiosedimentary Processes in Estuaries
Final Report of the Estuary Process Research Project (EstProc)
R&D Technical Report prepared by the Estuary Process Consortium for the Fluvial, Estuarine and Coastal Processes Theme
Report No FD1905/TR4 – Metadata Report

- This catalogues the metadata from input data used in the project.

The structure of the present report is as follows:

Chapter 2 introduces and presents more than 30 algorithms developed during the research project.

The algorithms are presented under 9 headings:

2.1 Modelling of waves in estuaries
2.2 Prediction of the impact of extreme events and major anthropogenic influences
2.3 Results obtained from the interrogation of data
2.4 Representation of near bed stresses
2.5 Transport of mixed sediments
2.6 Understanding of the sediment transport profile
2.7 Understanding of general sedimentary processes
2.8 Biological process parameters that effect stability, erodibility and deposition of sediments
2.9 Methodology for including effect of biological processes into morphological models

The project was not contracted to produce source code or .exe files so they were not provided. The project took the more flexible approach of providing algorithms that

were not platform specific which could then be coded up by individual modellers on their specific platform.

For more information contact the project leader, Dr Richard Whitehouse at HR Wallingford (r.whitehouse@hrwallingford.co.uk or tel: +44 (0)1491 835381), or contact the originating organisation/contact person responsible for the individual algorithm, indicated in the title line of the algorithm:

HRW - HR Wallingford
POL - Proudman Oceanographic Laboratory
UOP - University of Plymouth
GML - St Andrews University, Gatty Marine Laboratory (Sediment Ecology Research Group),
ABP - ABP marine environmental research,
WLD - WL | Delft Hydraulics,
PML - Plymouth Marine Laboratory,
CCRU - University of Cambridge, Cambridge Coastal Research Unit,
UOS - University of Southampton, School of Ocean and Earth Sciences,
DHH - Digital Hydraulics Holland B.V., and
CEFAS - Centre for Environment, Fisheries and Aquaculture Science.

More information on the project and a copy of this report can be obtained from the website: www.estproc.net or from the Defra website: www.defra.gov.uk

2. ALGORITHMS AND METHODS

This chapter presents the key scientific outputs of the project which are new algorithms and methods for implementation in numerical models of estuarine processes and associated analysis. It begins with a section summarising the aim, format and contents. The algorithms presented are at two levels of development:

1. Concepts or derivations based on data or theory; and,
2. Concepts or derivations based on data or theory that have been implemented and tested against other data.

Where possible the following information has been presented, especially for level 3 algorithms.

- The name and aim of method/algorithm;
- The scientific background/ justification/validation;
- Information on how the work in EstProc has improved our understanding of this topic;
- Statement as to how the method/algorithm be implemented;
- Statement of the algorithm or method in formulaic form suitable for implementation in a model - specifying inputs/outputs/limits of applicability/provide graphical information to justify algorithm;
- Specification of any gaps in knowledge identified

Some of the algorithms remain qualitative in nature.

The algorithms are presented under each of the 9 topics outlined in chapter 1. For ease of identification each algorithm, regardless of whether it is level 1, 2 or 3, has been assigned a unique code, EP1 through to EP30 with EP signifying EstProc.

Unless otherwise stated, standard SI units are expected for the quantities described.

The results are presented with best intentions to provide methods for use in estuarine studies but reliance on the information in this report is not a suitable substitute for necessary expertise and site-specific studies and investigations. Third parties should not rely on the algorithms without fully testing and validating them.

2.1 Summary of algorithms

The following table illustrates the state of development of the algorithms in the following sections:

Algorithm Number	Short title	Originator	Level 1	Level 2
EP1	Waves in estuaries during tides	HRW		Y
EP2	Waves in estuaries	POL		Y
EP3	Waves, friction and vegetation	CCRU		Y
EP4	Waves, dissipation and vegetation	DHH	Y	
EP5	Vegetation friction factor	WLD		Y
EP6	Wave height limit on flats/marsh	CCRU	Y	
EP7	Porosity method for flow	HRW		Y
EP8	Raster method for flow	ABP		Y
EP9	Analytical relations for estuaries	POL	Y	
EP10	Estuarine parameters from data	PML	Y	
EP11	Turbulence and sediment mixing	UOP	Y	
EP12	Dimensional relations of estuaries	UOP	Y	
EP13	Wave-current bed shear stress	HRW		Y
EP14	Moveable bed roughness	ABP		Y
EP15	Near bed stresses	PML		Y
EP16	Mixed sediment transport	WLD		Y
EP17	Analytical sediment profile	HRW	Y	
EP18	Mass settling flux flocculated seds	UOP		Y
EP19	1-D and 2-D generic models	POL	Y	
EP20	Sediment mixing in estuaries	WLD		Y
EP21	Gravitational circulation	WLD		Y
EP22	Sediment-induced density currents	WLD		Y
EP23	‘Stress exposure’ correction for sand	SOES	Y	
EP24	Day-night stability of sandy seds	SOES	Y	
EP25	Bed update strategy selection	WLD	Y	
EP26	Characteristic estuarine values	POL	Y	
EP27	Sediment-biology interaction	ABP		Y
EP28	Biological process parameters	PML		Y
EP29	Index for biological stabilisation	SOES	Y	
EP30	Waves and marsh edge configuration	CCRU	Y	
EP31	Accretion on marshes with creeks	CCRU	Y	

2.2 Modelling of waves in estuaries

2.2.1 EP 1 - Algorithm for single point wave generation and transformation models (HRW-Tozer)

Aim To improve the representation of waves in estuaries with regard to changes in wave activity occurring over the tide

Scientific background
Waves in estuaries can comprise of locally generated waves and more distantly generated waves that propagate into the estuary from offshore. Both sets of waves are subject to a wide range of physical processes that makes their prediction difficult. Waves generated within the estuary will depend on the growth area, which may change shape during the tidal cycle, and the wind. These locally generated waves, and those that are generated more distantly that propagate into the estuary, will be subject to the processes of shoaling, refraction, reflection, diffraction, blocking, white-capping, and depth induced breaking. All these processes will depend on the currents and water levels associated with the tides.

There are, presently, a wide number of computational wave models that represent some of these processes, but none that represent all. Recent advances over the last 10 years has led to the development of a group of phase averaged spectral wave models that can be regarded as the present state of the art in coastal area wave models. These models are based on the research and development of models devised for wave modelling on a global scale, but with considerable research and development, that is ongoing, to incorporate representations of the shallow water processes characteristic of the coastal environment. These types of models are computationally intensive and in prediction of a long term time series of wave conditions remain impracticable. Simpler models exist, that are sufficiently computationally efficient, but at the expense of not representing as many of the physical processes.

The algorithm below describes a method for improving the representation of changes due to the tidal cycle in simple point wave models.

Improvement in understanding
The new method improves on existing methods because:

- it can improve the accuracy of the wave predictions, by accounting for the change in generation area occurring over the tide

But:

- there is an associated increase in setup and run time which will be a function of the number of water levels in the tidal cycle considered.

Implementation
The algorithm is based on point models such as HINDWAVE that require only fetch lengths, wind speeds and directions as input.

Algorithm

INPUTS
Time series of water levels at times corresponding to model input wind data
Bathymetric detail over generation area.

OUTPUTS
Time series of wave predictions for different states of the tide that, dependent on water level, can be combined to provide a more representative prediction of wave conditions at a point.

To account for locally generated waves.
1. Measure fetch lengths radially from the point of interest to the intersection with land.
2. For fetches that extend over shallow banks their length should be restricted beyond the shallow banks so that the broken wave height can not be exceeded. Estimates of the broken wave height of 0.55 times the water depth and fetch lengths can be approximated from the standard JONSWAP curves published in a variety of sources.
3. Run the wave generation model for a time series of wind conditions to produce a set of time series of predicted waves.
4. Repeat steps 1 to 3 for a range of tidal levels to produce a time series of predicted wave conditions.
5. Combine the set of time series of predicted wave conditions dependent on the appropriate water level to produce a final time series of predicted locally generated wave conditions.

To account for the transformation of more distantly generated waves into the area of interest
1. Modify the wave model grid by introducing islands in areas where significant energy dissipation due to wave breaking is expected to occur, i.e. where the significant wave height of the offshore waves are reduced to a negligible amount or are small compared with the locally generated significant wave height.
2. Run the wave transformation model using the time series of offshore wave conditions.
3. Repeat steps 1 and 2 for different water levels.
4. Combine the sets of time series of predicted transformed waves from offshore dependent on water level to produce a final time series of predicted transformed wave conditions.
5. Combine the time series of locally generated and transformed offshore wave conditions on an energy basis.

Limits of applicability
The algorithm only applies to models that do not already include energy dissipation due to wave breaking.

Validation
The effectiveness of the algorithm was investigated using a HINDWAVE-TELURAY model of the Outer Thames Estuary (Tozer et al, 2004). Model results were compared against a reference data set based on measured wave conditions at a single point. For

The Outer Thames Estuary, HINDWAVE-TELURAY resulted in predictions of significant wave height and mean periods with rms errors within 0.6m and 0.7s respectively. This can be compared with the results from the spectral wave models SWAN (version 40.11) and TOMAWAC (V5P2) run for the same area, in which the rms errors in predicted significant wave height and mean periods were between 0.2 to 0.5m and 1 to 2s, respectively.

Conclusions

With suitable calibration data this algorithm is capable of providing a reasonable representation of the nearshore wave climate where, due to present computational constraints and the number of variables, the use of spectral wave models, such as SWAN or TOMAWAC would not be viable.

References

Tozer, N.P., Grey, S.M. and Ellam, T.J., (2004) Wave modelling in estuaries with regard to changes in wave activity occurring over the tide, HR Wallingford Report TR141, May 2004.

2.2.2 EP2 - Parametric modelling of waves in estuaries (POL - Wolf)

Parametric Modelling of Waves in Liverpool Bay and Dee Estuary
J.Wolf, POL Report ID162, November 2003

Aim The need for 'rules' to guide long-term cellular morphological models for open coasts and estuaries has led to this attempt to derive simple parameters relating wave height to offshore boundary conditions, wind-speed, fetch and water depth. The SWAN model is regarded for this purpose as producing the 'real' wave field. Actually, due to model limitations, this will not be correct, but it is interesting to see how close an approximation to a complex model can be achieved by a parametric model.

Approach
The SWAN model has been run for a set of scenarios, with a grid resolution of less than 200m (1/600° by 1/400°), for the Liverpool Bay area including part of the Mersey Estuary and most of the Dee Estuary (the bathymetry for the latter is rather crude in the upper part of the Dee – a new bathymetry survey should be available soon). This model contains an area of open coast as well as an estuary (see Figure 1). Several scenarios of wind-driven waves were run with SWAN (versions 40.11 and 40.31), combinations with separate wind sea and swell have not been examined. Three wind-speeds were chosen: 5m/s, 15m/s and 25m/s, approximately representing the background (every day) wave conditions, the once a year winter storm and the 1 in 100 year storm. Three water levels were used in combination with these wind-speeds viz. mean sea level, mean high water springs (MHWS) and mean low water springs, giving a total of 9 model runs. In fact the mean sea level runs were sufficient to characterise the response. Various parameterisations were derived for the wave height and peak period in terms of water depth, wave boundary conditions and wind speed, attempting to use only local variables.

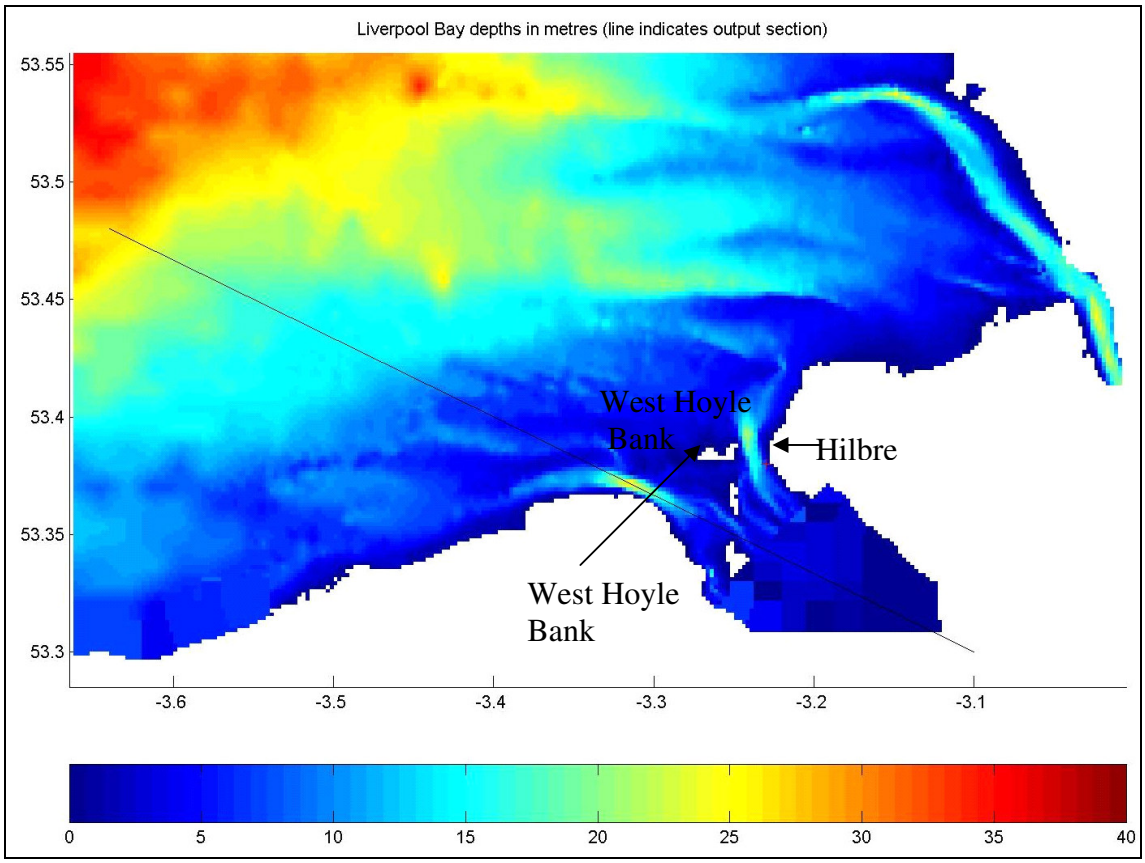

Figure 1 Liverpool Bay SWAN model depths at mid-tide. The colour scale provides a key for depths in metres and the coordinates are degrees longitude and latitude. Black line indicates section along which detailed model output has been selected

Offshore wave boundary conditions in approximate equilibrium with the selected wind were chosen. The wind is assumed constant over the whole area, always from NW, with 10-m wind-speeds of 5, 15 and 25 m/s respectively. The wave field in SWAN is therefore driven by a combination of the boundary forcing and the local wind. The 3 wind scenarios are summarized in Table 1.

Table 1 SWAN model scenarios

	Ws(m/s)	Hs(m)	Tp(s)
Low waves	5	0.7	4
Medium waves	15	4.9	9.2
High waves	25	7.4	11.6

The open coast and estuary are immediately seen to behave differently. The two regimes partition very nicely by means of the peak wave period. Figure 2 shows a map of peak period from SWAN for the 15m/s wind case. Outside the estuary the peak period is determined by the boundary input value. There is some transmission of the offshore wave forcing (mainly down the Mostyn and Hilbre channels) but much of the

wave energy inside the estuary is driven by the local wind. As a result the two regimes were parameterized separately.

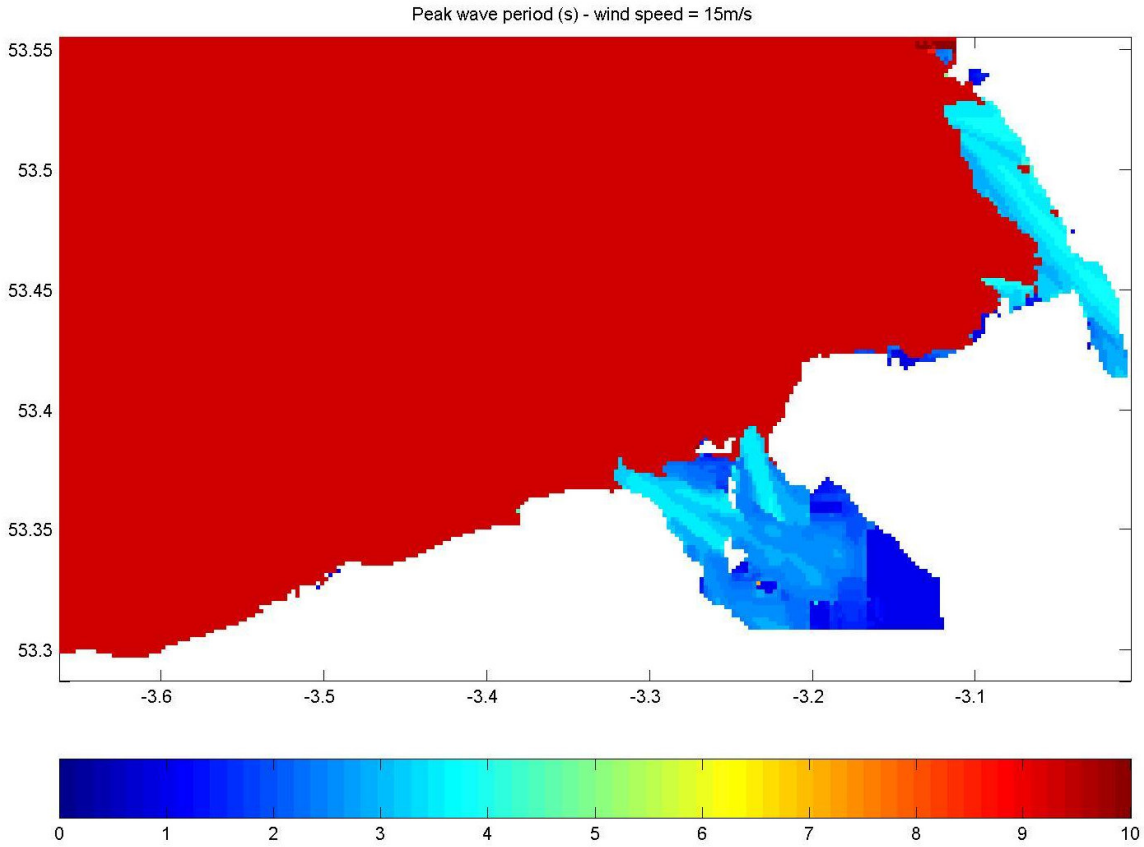

Figure 2 Peak period from SWAN – wind-speed = 15 m/s. The colour scale provides a key for period in seconds and the coordinates are degrees longitude and latitude

Open coast

As waves approach the shore, there is observational evidence for a self-similar wave spectrum to be applicable, which accounts for the redistribution of energy as the waves shorten e.g Tucker and Pitt (2001), p. 337. The peak period remains constant, equal to the value specified at the open boundary. Two options were tested for significant wave height, *Hs*, based on either the Tucker or Kitaigorodskii (TMA) scaling factor.

TMA self-similarity scaling

The TMA scaling factor, comes from fitting a standard spectral shape to wave measurements in shallow water (see Bouws et al, 1985). A depth-dependent scaling factor, φ, is applied to the deep water JONSWAP spectrum. The TMA spectrum can be written:

$$S_{TMA}(\omega,h) = S_J(\omega,h)\phi(\omega_h)$$

with $\phi(\omega_h) = \dfrac{\tanh^2(kh)}{1+2kh/\sinh(2kh)}$ also known as the Kitaigorodskii scaling factor

where $\omega_h = \omega\sqrt{h/g} = \sqrt{kh\tanh(kh)}$ is a non - dimensional frequency and (1)

$S_J(\omega,h) = G(\omega)\alpha\, g^2\omega^{-5}\exp[-(5/4)(\omega_p/\omega)^4]$

is the deep - water JONSWAP spectrum

with $G(\omega) = \gamma^{\exp[-(\omega-\omega_p)^2/2\sigma^2\omega_p^2]}$, $\sigma = \sigma_a$ for $\omega < \omega_p$ and $\sigma = \sigma_b$ for $\omega > \omega_p$

Here, *h* is the water depth and *g* is the acceleration due to gravity.

Tucker's method

Tucker (1994) showed that the nearshore wave height for storm-generated waves could be scaled with the inverse of the peak wavenumber. This is equivalent to assuming constant steepness, so that H_S is proportional to *1/k*. We can then use the formula:

$$H_s = H_{sb}\frac{k_{pb}}{k_p}, \tag{2}$$

where H_{sb}, k_{pb} are the wave height and wavenumber on the boundary, respectively.

The linear dispersion relation, $\omega = \sqrt{gk\tanh(kh)}$, relates wavenumber ($k$=2π/wavelength) and frequency (ω=2π/period), but must be solved iteratively. The following approximation can be used to calculate the peak wavenumber, given the wave period, to within 2% (ref?).

$$k_p = \frac{{\omega_p}^2}{g\tanh^{2/3}({\omega_h}^{3/2})} \quad \text{where} \quad \omega_h = \omega_p\sqrt{\frac{h}{g}}. \tag{3}$$

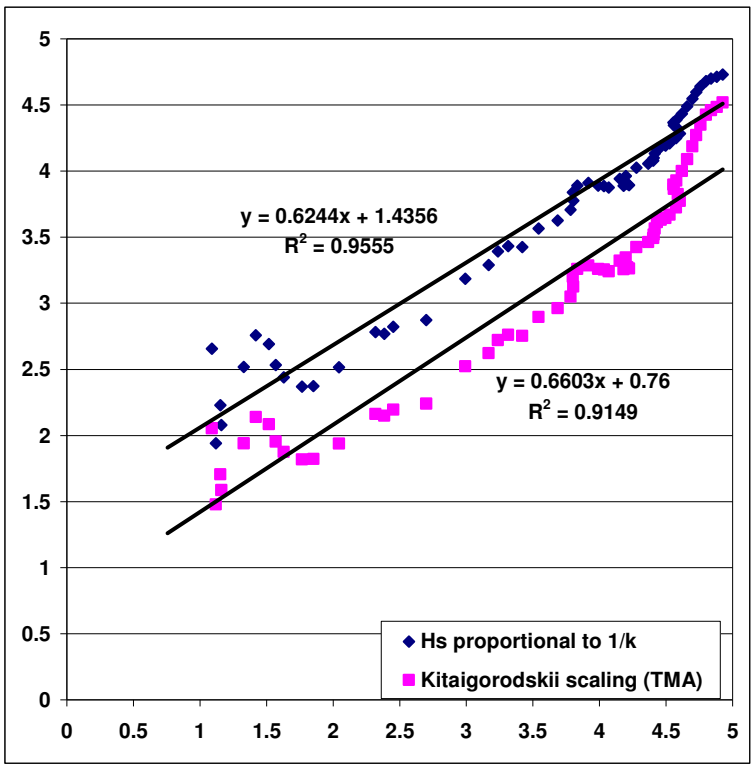

Figure 3 Comparison of scaling methods – axes show wave heights in metres

Figure 3 shows the fit between parametric and SWAN model wave heights along the section shown in Figure 1. Tucker's method (dark blue diamonds) gives a slightly better fit than TMA (magenta diamonds), although both start to break down for low wave heights, very near shore, which will be discussed later. As it is also simpler to calculate, Tucker's scaling was selected for the open coast parameterisation.

Estuary

The formulae for fetch-limited growth in shallow water from the Shore Protection Manual (SPM), USACE (1984), are:

$$H_S = 0.283\frac{U_a^{\,2}}{g}\alpha\,\tanh(0.00565\sqrt{\bar{f}}\,/\alpha), \quad T_P = 7.54\frac{U_a}{g}\beta\,\tanh(0.0379\sqrt[3]{\bar{f}}\,/\beta) \qquad (4)$$

where $\alpha = \tanh(0.53\bar{d}^{\,0.75})$, $\beta = \tanh(0.833\bar{d}^{\,0.375})$. The non-dimensionalised depth and fetch respectively are $\bar{d} = hg/U_a^{\,2}$, $\bar{f} = fg/U_a^{\,2}$ and the effective wind-speed $U_a = 0.71(1.1U_{10})^{1.23}$. Here, f is the fetch in metres, and U_{10} is the wind speed at 10m above the sea surface. These equations were used to parameterise the wave height and period for the Dee and Mersey estuaries. The fit along the part of the model sections within the Dee is shown in Figure 4 and is very good. Two calculations were made, one with a variable fetch calculated from just inshore of the West Hoyle Bank, and the other with a constant 5km fetch. The latter was found to be as good as using the realistic fetch and simplifies the parameterisation as fetch need not be calculated for different wind direction.

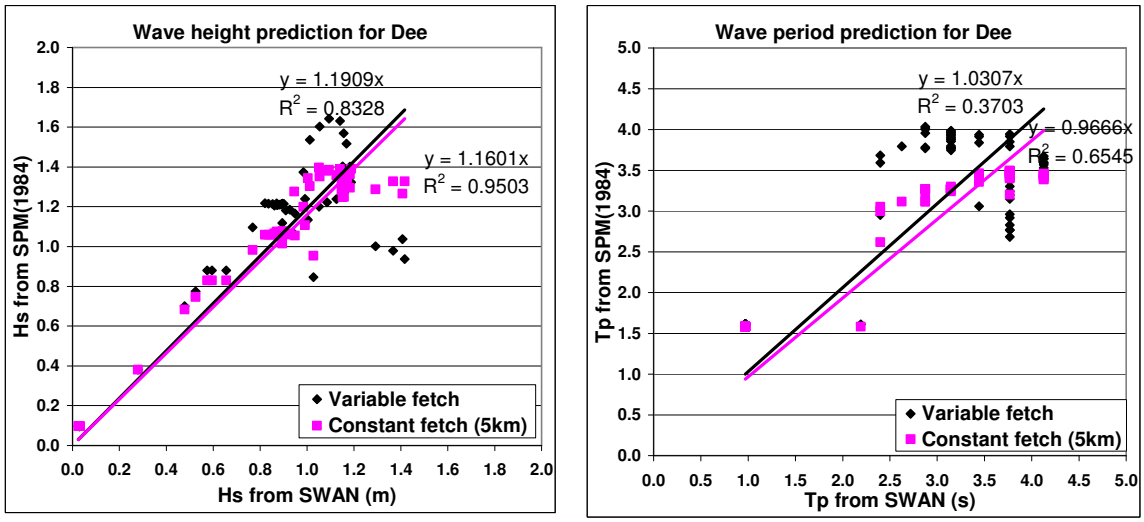

(a) **(b)**

Figure 4 (a) Wave height and (b) period in the Dee fitted using the SPM formulae

Nearshore zone

The open coast model breaks down when the depth drops below about 10m. In this region wave breaking limits wave height, the wave spectra become bimodal with both local wind-sea and boundary forcing (acting like swell) both being important. It is in this region that the complexity of a model like SWAN cannot easily be parameterized. A better fit was achieved by including a crude wave dissipation, related to wave height, Hs/h and water depth. By trial and error the following formula was applied:

$$H_s' = H_s - H_{sds}, \text{ where } H_{sds} = 2.5 H_s \frac{H_s}{h} \exp(-0.3h) \quad (5)$$

This nearshore zone still shows the largest discrepancy between the parametric and SWAN model. Figure 5 shows the correction to the wave heights achieved for the high wave case which required the largest correction.

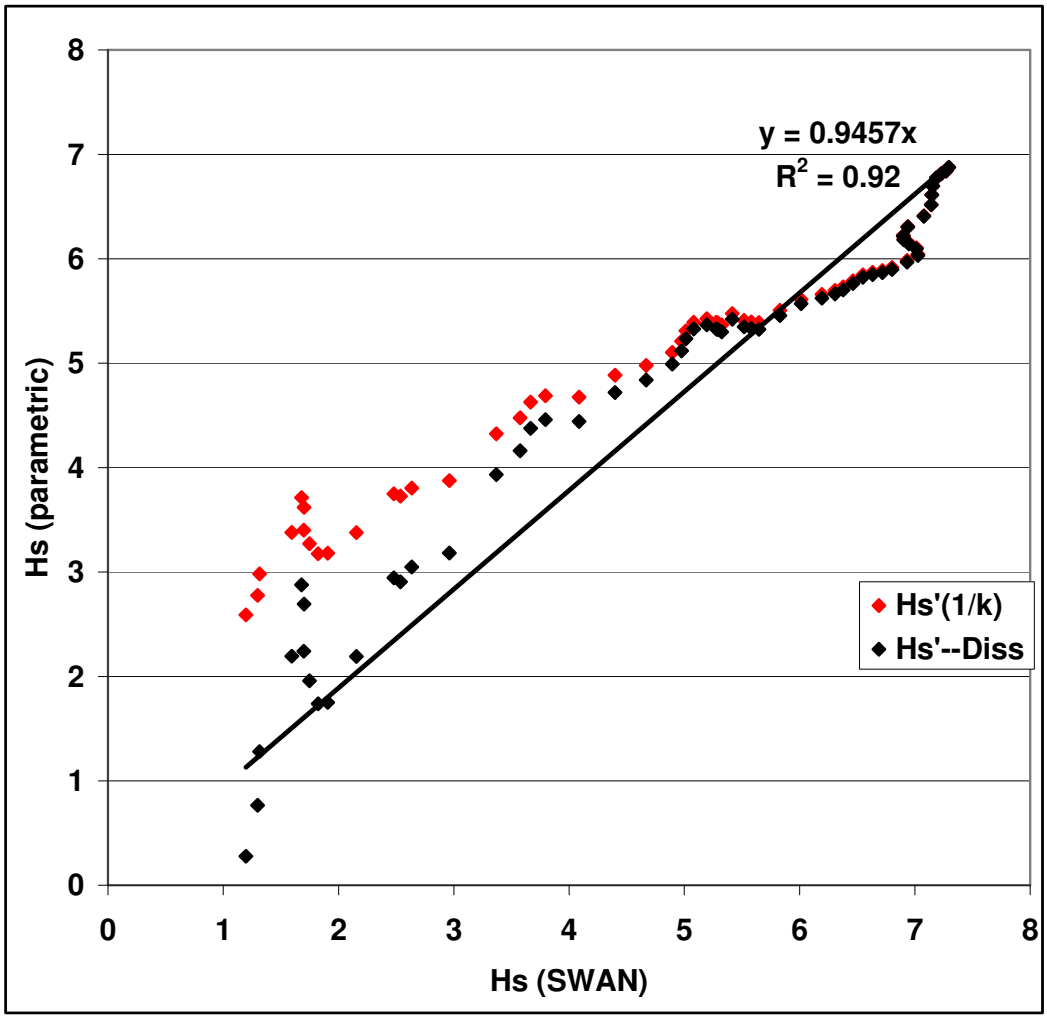

Figure 5 Parametric versus SWAN wave height in metres along a section
The lowest wave heights correspond to the points nearest the coast. The red diamonds are the uncorrected wave heights and the black diamonds are the wave heights after a correction for wave dissipation has been made.

The depth is not necessarily decreasing monotonically towards the coast and the spectra in this region are bimodal. Therefore there is a limit to the applicability of these simple models in this zone.

Results

After application of the above formulae: (2) and T_p = constant for the open coast, (4) for the estuary and applying the dissipation correction (5) a reasonable agreement is obtained for the parametric and SWAN model. Figure 6 shows the comparison for the 15m/s case.

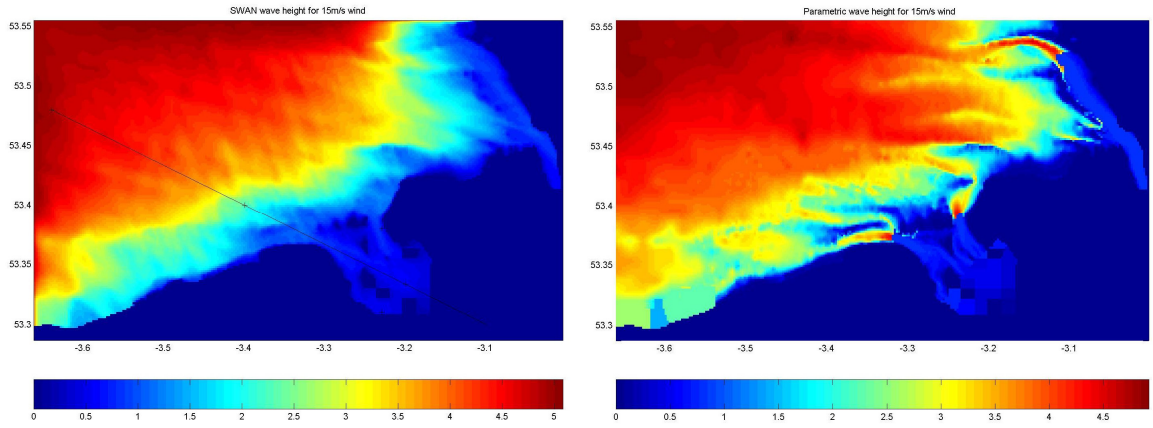

Figure 6 SWAN (left) and parametric model (right) wave height for 15m/s wind. The colour scale provides a key for wave height in metres and the coordinates are degrees longitude and latitude

The r.m.s. errors for the 5m/s, 15m/s and 25m/s wind speeds were 0.05m, 0.41m and 0.55m respectively, or less than 10% of the mean wave height. The main discrepancies in wave height occur in the nearshore zone, within the 10m contour, as illustrated in Figure 7.

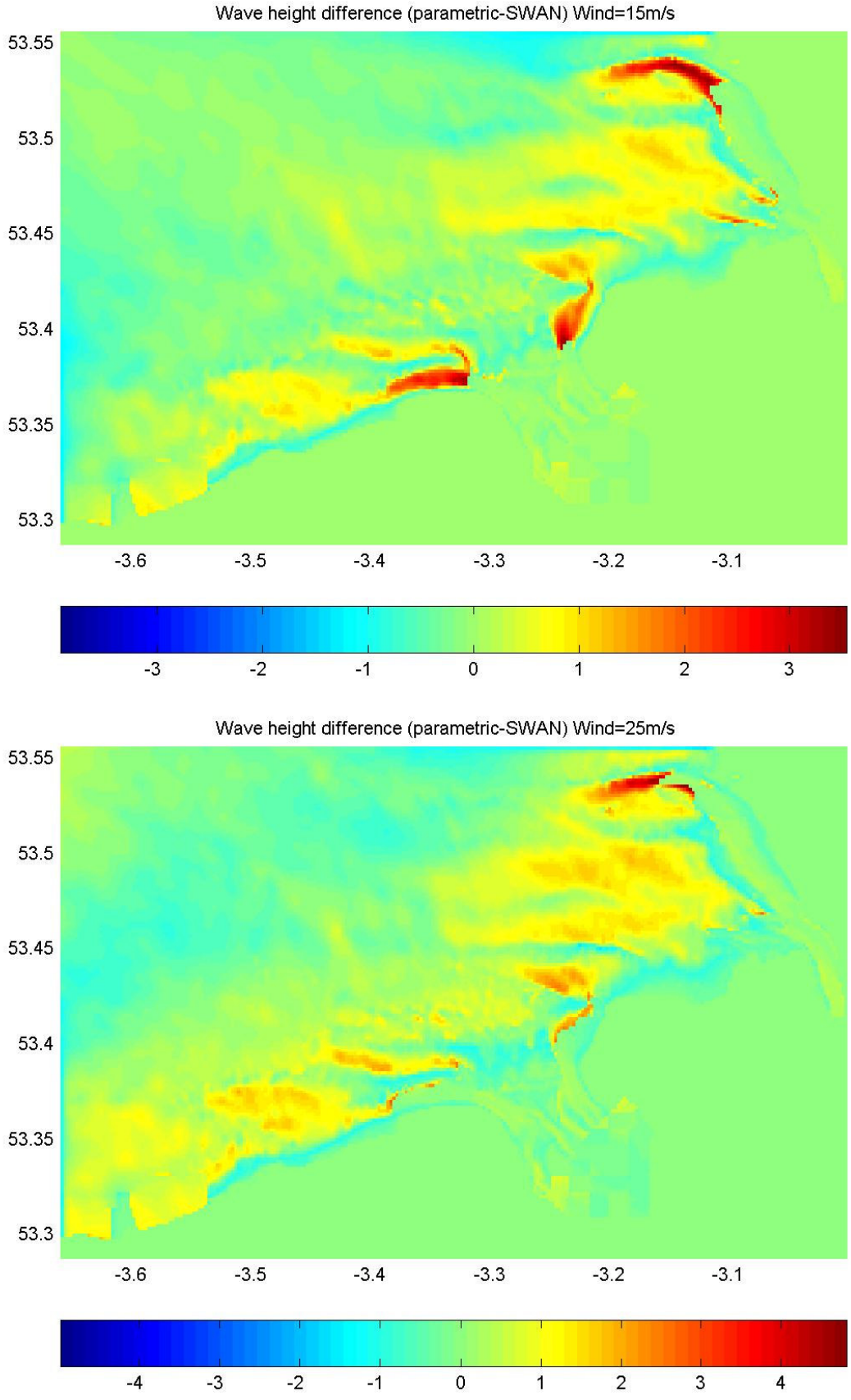

Figure 7 Difference between parametric and SWAN model wave height in metres for three scenarios – low, medium and high waves. The coordinates are degrees longitude and latitude

Conclusions

1. The open coast and estuary behave differently. The Dee estuary is sheltered behind the West Hoyle Bank. (This presumably is true for most estuaries to a greater or lesser degree behind flood and ebb shoals). The open coast exhibits a constant peak period to very near the coast, and is mainly controlled by the boundary forcing except within the 10m contour. The estuary experiences some transmission of boundary forcing plus mainly local wave generation by wind.
2. Self-similarity scaling, with a constant peak period can be used to predict the open coast conditions. It is possible to use the Tucker or Kitaigorodskii (TMA) scaling. Tucker's formula effectively assumes constant steepness ak, so that H_S is proportional to $1/k$.
3. The parametric formulations for fetch-limited wave growth, e.g. SPM formulae, work well for the estuary.
4. The discrepancies are largest in the nearshore zone and the entrances of the main channels of the estuary. There is likely to be some transmission of waves along the channels. In very shallow water near the coast (less than 10m) the attenuation due to dissipation processes, bottom friction and depth-limited breaking, becomes important and in this zone the full complexity of processes requires a more detailed model such as SWAN.

References

Bouws, E., Gunther, H., Rosenthal, W. and Vincent, C.L. 1985. Similarity of the wind wave spectrum in finite depth water 1. Spectral form. Journal of Geophysical Research, 90, C1, 975-986.

Tucker, M.J. 1994. Nearshore waveheight during storms. Coastal Engineering, 24, 111-136.

Tucker, M.J. and Pitt, E.G. 2001. Waves in Ocean Engineering. Elsevier Ocean Engineering Book Series, volume 5. 521pp. Amsterdam: Elsevier, 2001.

USACE. 1984. Shore Protection Manual Vol 1. 4th edition. Washington D.C. US Army Corps of Engineers Coastal Engineering Research Centre, 1984.

2.2.3 EP3 - Algorithms for vegetated marsh surface friction coefficient (CCRU-Turner)

Aim To create a new friction coefficient for implementation within the SWAN (Simulating Waves Nearshore) model. To enable the model to calculate changes in wave parameters, not only through the inclusion of the bathymetric profile but also through the inclusion of wave energy attenuation due to roughness introduced by i) the morphology of the mudflat-saltmarsh transition and ii) the vegetation canopy structure of saltmarshes lying high in the tidal frame.

Scientific Background
Rather than creating a new wave model, it was decided that the best use of the resources available in EstProc was to create an algorithm that would perform well within the existing Delft-3D SWAN model (version 40.11).

The SWAN model is a third generation spectral model developed by a team at Delft University of Technology (Netherlands), and is designed for use between the area along the coastal seas covered by the WAMDI model (which can only be used validly for resolutions of 20-30 km and in water depths of 20-30 m (Komen *et al*., 1994)). SWAN is designed for use between water depths of 20-30 m and the highest astronomical tide level. SWAN is a Eulerian model and is based on the action balance equation:

$$\frac{\partial}{\partial t}N + \frac{\partial}{\partial x}C_x N + \frac{\partial}{\partial y}C_y N + \frac{\partial}{\partial \sigma}C_\sigma N + \frac{\partial}{\partial \theta}C_\theta N = \frac{S}{\sigma}$$

From the left, the first term represents local rate of change of action density N in time, the second and third terms represent the propagation in x and y (space) with C_x and C_y (the propagation velocities in space). The fourth term represents the shifting of relative frequency due to variations in water depth and currents while the fifth term represents depth induced refraction.

The right hand term is the energy source term, which accounts for:

- generation
- dissipation
- non-linear interactions between waves (triads and quadruplets).

The SWAN model has been extensively tested and validated. Thus, for example, project JERICHO which used satellite data and buoy data with SWAN to examine how changes in wave behaviour in deep water translate into shallow water. However, this project, like all other previous projects employing SWAN, concentrated on waves over a large area (e.g. greater than 15 km^2). There was thus a need to evaluate the performance of SWAN over relatively short distances (10s to 100s meters) and in very shallow water depths (< 1 m).

Benefits from EstProc
The focus of this component of EstProc was to test the performance of SWAN over relatively short distances (ca. 200 m) and shallow water depths (< 1 m) of the upper intertidal profiles at Dengie, Essex, UK.

Firstly, the bottom friction coefficients included within the model were evaluated. These are: JONSWAP coefficient (Hasselmann 1973), the coefficient of Madsen *et al.* (1988), and the coefficient of Collins (1972). The JONSWAP coefficient is an empirically based constant, the Madsen coefficient is derived from a complicated eddy viscosity model, and the Collins coefficient is a non-linear formulation based on drag (Booij *et al* 1999); it is only possible for one of these coefficients to be employed within the model for each SWAN run. It was decided to use the Collins coefficient as this could include not only variations in vegetation density induced roughness over the transect but also an element of vegetation height (Booij pers. comm. 2003).

Justification
The attenuation was calculated based on the Collins' drag law (Collins 1972). The equation used in the SWAN model for the Collins' drag law is:

$$C_{bottom} = C_f \cdot g \cdot U_{rms}$$

Where C_f is the friction coefficient (the default of this value in SWAN is 0.015), g is the gravitational acceleration and U_{rms} is the wave-induced orbital velocity at the bottom of the water column (Booij *et al*., 1999).

The Collins coefficient was originally derived for water depths exceeding the shallow film of water which covers a saltmarsh during inundation, and in its unmodified state the Collins drag law does not explicitly include any representation of bottom friction due to the presence of vegetation. As part of the EstProc study, the aim was to modify the coefficient to more accurately reflect the observed wave attenuation over saltmarshes in the UK, and also in combination with EstProc work in The Netherlands. This was achieved by first comparing observed wave attenuation with predicted attenuation using the SWAN model and changing the value of C_f to improve the statistical fit between predicted and observed attenuation. Subsequently, it was found that the new, improved, value of C_f could be approximated by multiplying a series of vegetation characteristics, namely:

- stem diameter, vegetation height, and the density of vegetation observed on the marsh.

The coefficient created by the EstProc team (known as Cf_{veg}) thus replaces the C_f term in Collins' drag law in the model, and is based on specific and detailed data on the vegetation structure:

- the average plant stem diameter (d) (in meters) in the square metre monitored
- the number of plants (not stems) per metre square (n)
- the average height of the plants (in meters) in one square metre (h_{veg}).

The Cf_{veg} term is calculated from these parameters simply as:

$$Cf_{veg} = C_w \cdot d \cdot n \cdot h_{veg}$$

Where Cw is a drag term. In its present form, Cf_{veg} is easily incorporated into the SWAN model as it simply replaces C_f, with the strength of the coefficient changed by the Cf_{veg} value.

Inputs

- Seaward boundary H_s (m)
- Seaward boundary T_p (secs)
- Bathymetry (m)
- Water depth (m).

For the vegetation coefficient:

- The average plant stem diameter (d) (in meters) in the square metre monitored (m)
- The number of plants (not individual stems) per metre square (n)
- The average height of the plants (in meters) in one square metre (h_{veg}) (m)
- The drag term C_w.

Outputs

Pattern of wave spectra and wave parameters such as H_s and T_p along a cross-shore transect from the seaward boundary landwards.

Validation

The above method was calibrated using data from just one tidal inundation of the Dengie marshes, Essex, England and the marshes of Paulinaschor, Scheldt estuary, The Netherlands. The model was then tested on 14 other tides from Dengie (Figure 1) and other tides in Paulinaschor. This model has recently been tested on 9 further tides from a second phase (July 2001 – April 2002) of data collection on saltmarsh inundation events from the Dengie Peninsula (which has been processed under the EstProc project). As can be seen in Figure 1, the model predictions of wave attenuation were comparable to those in Phase 1 of the dataset.

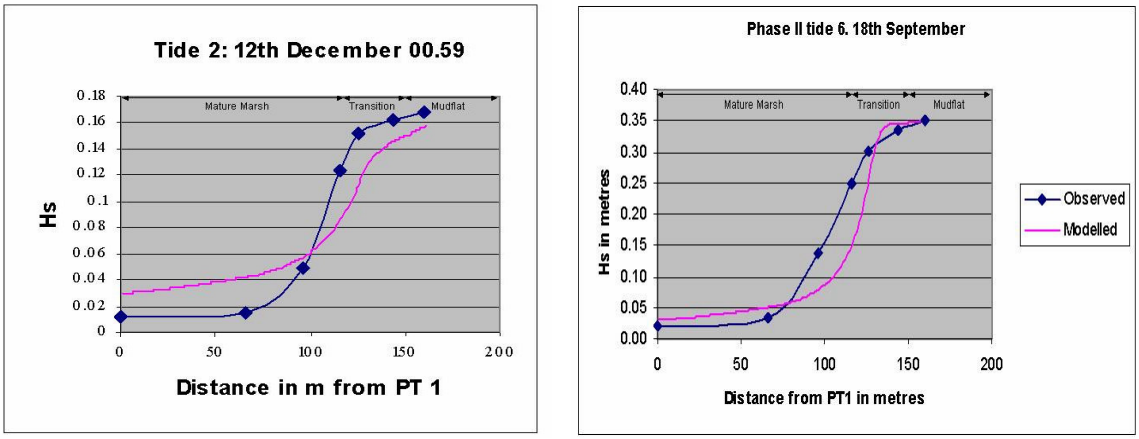

Figure 1 Plotted comparisons of observed Hs at Dengie (blue, with data points) and SWAN predicted Hs (pink), one from each phase of data collected at the Tillingham site. PT1 is pressure transducer 1 located near to the seawall and distance is measured in offshore direction

A)

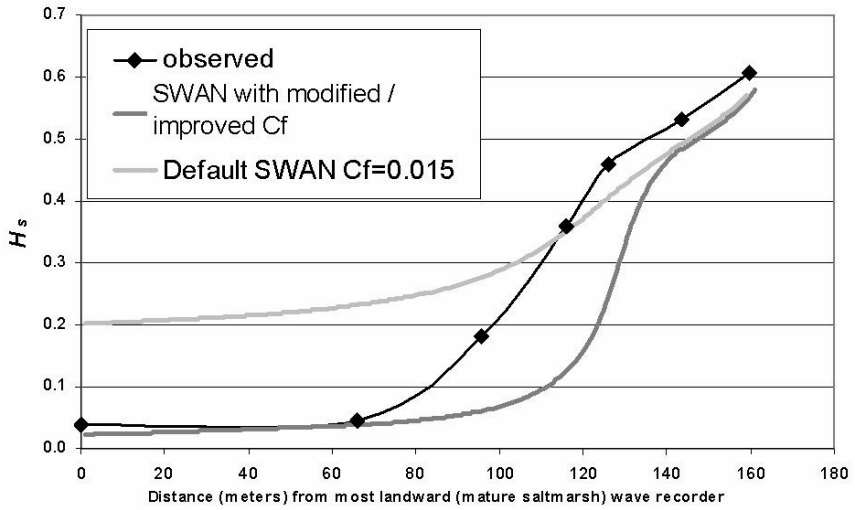

B)

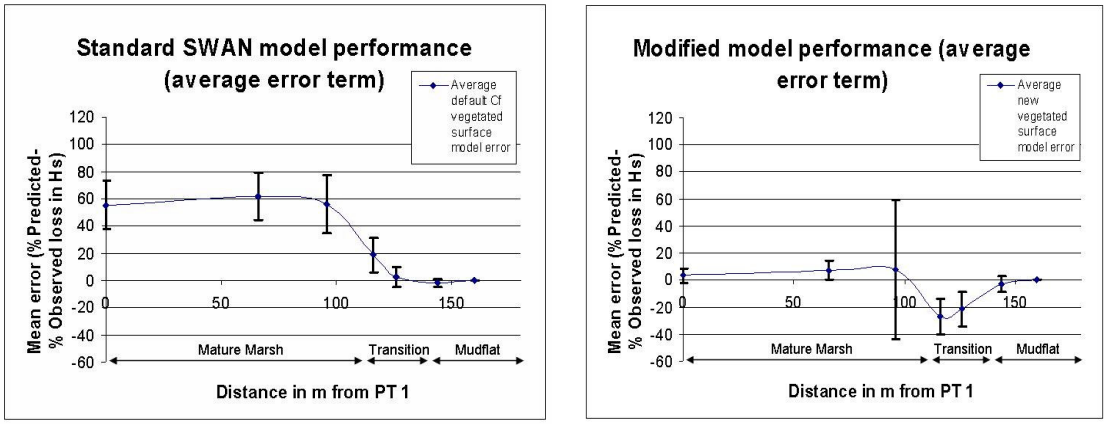

Figure 2 Comparison of measured and modelled Hs and associated errors (see Figure 1 for note on PT1)

Note: (A) Simulation of significant wave heights along cross-shore transect using default SWAN model setup and model with improved friction term, compared to observed attenuation on a typical tide (tide 8, phase I (10/01/2000, 13.09) and (B) Mean error as difference between modelled and observed H_s reduction (%) relative to seaward transect limit for (i) SWAN in default mode (i.e. Cf = 0.015) – shown above left and (ii) SWAN using optimised friction terms approximated from vegetation measurements – shown above right (error terms were computed by comparing model runs with observed wave attenuation over 24 wave records (tides)). Error bars indicate ± one standard deviation around the mean.

While the SWAN model, run in default mode (Figure 2A), predicts wave attenuation from the most seaward limit of the transect to the mudflat/saltmarsh transition zone relatively well, it fails to achieve accurate attenuation values over the mature marsh. The panels of Figure 2 illustrate the significant improvement in terms of overall prediction of wave attenuation over the entire transect when the empirical friction factors, approximated from vegetation measurements, are used. The use of the empirical friction factors reduced errors from ca. 55% (SWAN in default mode) to < 5% (SWAN with modified friction factors) at the landward limit (ca. 120 m inland from the mudflat/saltmarsh transition zone). The results do suggest, however, that the modified friction factors used for the transition zone were unrealistically high, leading to an over-

prediction of attenuation in this particular cross-shore zone. Further work is needed to improve the representation of surface friction in this transitional area (see below).

The average value of Cf_{veg} for Tillingham was 0.63, with individual values based on a few vegetation observations and a gentle gradient in value between observations (Figure 3).

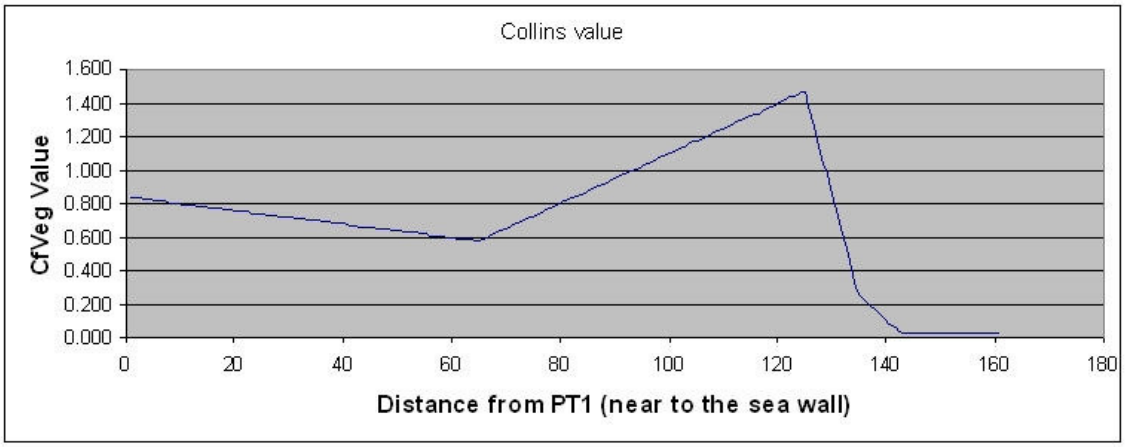

Figure 3 Spatial variation in value of coefficient Cf_{veg} for Tillingham

A high and invariant value of Cf_{veg} for Tillingham was used early in the model development but it became clear this gave a poor result as it could not mimic the patterns of dissipation shown on the marsh.

Gaps in the knowledge

The remaining discrepancy between modelled and observed attenuation (see Figure 2 above), in particular in the mudflat/saltmarsh transition zone, clearly indicates that the C_w term is a drag coefficient that will need to be defined more accurately following future research. It is likely to vary with vegetation type. For example the woody stems of *Atriplex spp.* will have higher C_w values than those attributed to 'softer', more flexible vegetation e.g. *Salicornia spp.* Values for saltmarsh species may in turn be greater than those associated with seagrasses. Previous models have used a fixed C_w value of 1.0, but as noted above this would not be able to reproduce the spatial variation in dissipation.

Further improvement of the coefficient can be made by incorporating stem numbers or by parameterising the coefficient according to species.

There is a lack of data for the investigation and development of the C_w drag term in the coefficient. This would be most efficiently collected in a laboratory flume environment where any changes in H_s reduction could only be attributed to the species planted in the flume. As yet it has not been possible for the model to account for the changing surface roughness which results from a 'floating canopy' effect. This occurs when the vegetation canopy lifts off the marsh surface on progressive inundation.

Limits of Applicability

The characterisation of vegetation by stem diameter, density, and height does not fully incorporate vegetation structure and rigidity. For a more physically meaningful

representation of vegetation in the model, these latter two vegetation characteristics must also be incorporated.

In theory the model should 'scale up' for use in environments with lower water depths (microtidal marshes), or 'scale down' for application in studies of seagrasses or kelp fields where vegetation acts less like a direct buffer and more to increases the viscosity of the water (Mork, 1996). The model remains untested for either of these vegetation types.

References

Booij N., Ris, R.C. and Holthuijsen, L.H. 1999. A third generation wave model for coastal regions 1. Model description and validation. Journal of Geophysical Research 104, 7649-7666

Collins, J.I. 1972. Prediction of shallow-water spectra. Journal of Geophysical Research 77, 2693-2707.

Hasselmann, M., Barnett, T.P., Bouws, E., Carlson, H., Cartwright, D.E., Enke, K., Ewing J.A., Gienapp, H., Hasselmann, D.E., Kruseman, P., Meerburg, A., Muller, P., Olbers, D.J., Richter, K., Sell, W. and Walden, H. 1973. Measurements of Wind-Wave Growth and Swell Decay during the Joint North Sea Wave Project (JONSWAP). Deutsches Hydrographischen Zeitschrift Suppl. 12, A8

Komen, G.J., Cavaleri, L., Donelan, M., Hasselmann, K., Hasselmann, S. and Janssen, P.A.E.M. 1994. Dynamics and Modelling of Ocean Waves. Cambridge University Press: Cambridge

Madsen, O.S., Poom, Y.K. and Graber, H.C. 1988. Spectral wave attenuation by bottom friction: theory. Proceedings of 23rd International Conference on Coastal Engineering. American Society of Civil Engineering. New York, 492-504

Mork, M. 1996. The effect of kelp in wave damping. Sarsia 80, 323-327

NB:

More explicit information on running the model can be found in the following report on the EstProc website:

Turner, R.H.C., Möller, I., Spencer, T. and Booij, N. 2003. Application of the SWAN model to vegetated surfaces. CCRU, unpublished EstProc Report.

2.2.4 EP4 - Algorithm- a model for wave dissipation due to flexible vegetation (DHH-Booij)

Aim To derive an expression for wave dissipation in a region with vegetation.

Background and basic assumptions
This part of project has worked on the derivation of an expression for wave dissipation in a region with vegetation. The vegetation is assumed to be flexible, and the vegetation height is assumed to be of the order of magnitude of the depth. Some simplifications are necessary in order to keep an analytic treatment feasible. Such simplifications are allowed in view of the erratic nature of vegetation in reality; a very accurate model would be impossible.

There are four basic assumptions:

1. All physical effects, including friction are assumed to be linear.
2. All time-dependent quantities are assumed to vary harmonically.
3. The dynamics is not integrated over the height of the vegetation, but is considered at one level which is related to the vegetation height.
4. The pressure fluctuations due to waves penetrate into the vegetation layer as if there were no vegetation.

Justifications for the assumptions
Assumption 1 is justified because the friction is fairly small. The nonlinearity can be introduced at the end in an approximate manner. Assumption 2 is valid if the previous one is; irregular wave motion is introduced at the end by taking a sum over many harmonic components. We introduce the following notation:

Let $p(t) = P \exp(i \omega t - i k x)$ be a harmonic function of time, then $|P|$ is the amplitude of the function.

Assumption 3 is hard to justify; it is expected that by a proper choice of the level representative of the whole layer a good result can be obtained. This representative level will be called z_v, it is a constant factor c_v times the vegetation height h_v or, if this is larger than depth, c_v times depth d; i.e. $z_v = c_v \, \mathrm{Min}(d, h_v)$.

Assumption 4 seems realistic because in general vertical velocities in the water body are small, certainly close to the bottom; this is expected to be true also for velocity differences between fluid and vegetation. Therefore the expression for pressure over the vertical can be taken from the generally accepted linear wave theory. Thus at level z_v the value of pressure $P = P_{surf}.\cosh(k z_v)/\cosh(k d)$, where P_{surf} is the pressure fluctuation at the (average position of the) surface, i.e. $P_{surf} = \rho g \eta$.

Equations of the model
The horizontal velocity of the fluid is calculated from the equation of motion:

$$i \omega \rho U + w(U-U_v) + dP/dx = i \omega \rho U + w(U-U_v) - i k P = 0$$

Here the friction coefficient w is assumed to be a given constant for the time being. The gradient of P is interpreted as the force per unit volume; thus w is the ratio of the force per unit volume and the velocity difference between fluid and stalks.

The velocity of the vegetation depends on the rigidity of the stalks; the force exerted by the fluid on the stalks is assumed to be in balance with the restoring force:
$w(U-U_v) + K X_v = i \omega w(X-X_v) + K X_v = 0$, so that $X_v = X / (1 + i K/\omega w)$, or $U_v = U / (1 + i K/\omega w)$. Thus $U = \Delta U (1 - i\omega w/K)$ where $\Delta U = U - U_v$.

The dissipation (per unit surface) is then obtained by taking the product of the friction force and the velocity $D = w/2 |\Delta U|^2 \text{Min}(d,h_v)$.

The energy density (energy per unit surface) is $E = 1/2 \rho g \eta^2$.

Coefficients w and K
The friction coefficient w is assumed to be constant; in reality it is not since we are always dealing with a turbulent regime. The following expression for w will be used: $w = C_D \rho \delta n |u-u_v|$; the average value for harmonic motion then is $w = 8/3\pi . C_D \rho \delta n |\Delta U|$. The problem with this relation is that $U-U_v$ is not known beforehand.

The coefficient K depends on mechanical properties of the vegetation. From structural mechanics an expression is known for circular tubes or massive cylinders made of an elastic material. Whether such a model is applicable for natural vegetation is doubtful. Probably it is more relevant to measure (if possible at all) the relation between a force on an individual stalk at level z_v and the displacement at the same level; let the ratio be called K_s. From this K can be calculated as follows: $K = n K_s / h_v$.

The restoring force often is not primarily caused by the mechanical strength of the plants but by their buoyancy. Let $\Delta\rho$ be the difference in mass density between plants and fluid. Further assume that the relative volume of the plants V_v (volume of the plants divided by total volume) is concentrated at the level z_v. Then the restoring force per unit volume divided by the displacement is: $K = \Delta\rho g V_v / z_v$. This is expected to be a very small quantity in practice, so that other effects may become dominating, such as increase of roughness due to the vegetation.

Transition to irregular waves
In the SWAN model one needs an expression relating $D(\sigma,\theta)$ to $E(\sigma,\theta)$; a very simple (and probably adequate) solution is to assume that the ratio D/E, the quantities derived in the previous section, is also valid for all spectral components. In SWAN the same has been done for the breaking dissipation term in the action balance equation.

In the above equations one would then use an average ω and corresponding average k. The value of $U-U_v$ is then a value valid for the whole spectrum, which is the value needed for the computation of the (nonlinear) friction coefficient w.

A disadvantage of this approach is that in case of a vegetation height much smaller than depth the high frequencies may be attenuated too much.

The value of U in the vegetation layer is also to be used as the output quantity "orbital velocity at the bottom"; the value calculated presently in SWAN is invalid in presence of vegetation.

Computation of w and D
From the equation of motion we obtain: $\rho \omega \Delta U (1-i\omega w/K) - i w \Delta U - k P = 0$, or $\Delta U [\rho\omega - i w (1 + \rho\omega^2/K)] = k P$. From this equation ΔU can be computed; further analysis is necessary because w depends on this quantity.

Since $w = 8/3\pi\ C_D\ \rho\ \delta\ n\ |\Delta U|$ the equation for ΔU can be rewritten as: $\Delta U\ [\rho\omega - i\ 8/3\pi\ C_D\ \rho\ \delta\ n\ |\Delta U|\ (1 + \rho\omega^2/K)] = k\ P$. Taking the absolute value of the above equation we get: $|\Delta U|\ |\rho\omega - i\ 8/3\pi\ C_D\ \rho\ \delta\ n\ |\Delta U|\ (1 + \rho\omega^2/K)| = |k\ P|$, enabling us to calculate $|\Delta U|$ and thereby the dissipation D.

For very flexible vegetation K is small, and then one gets: $\Delta U\ [-i\ w\ \rho\omega^2/K] = k\ P$. Then $U = k\ P\ /\ (\rho\ \omega)$. This is understandable, since with very flexible vegetation the velocity of the fluid is as if there were no vegetation, leading to a small dissipation: $D = w/2\ |\Delta U|^2\ Min(d,h_v) = 1/2\ U^2\ K^2\ w^{-1}\ \omega^{-2}\ Min(d,h_v)$.

For the case of a vegetation which is very low compared with depth ($h_v << d$) this can be translated into Collins friction formula with $C_f = 1/2\ K^2\ w^{-1}\ \omega^{-2}\ Min(d,h_v)$.

Another special case occurs when there is a rigid dense vegetation, i.e. w is dominant. $8/3\pi\ C_D\ \rho\ \delta\ n\ |\Delta U|^2 = k\ P$.

Evaluation and implementation
This method has been implemented, see EP3.

Notation

c_v	constant relating representative height in the vegetation layer and the vegetation height
C_d	drag coefficient for stalks or leaves
d	water depth
g	acceleration due to gravity
k	wave number (=2π/wavelength)
h_v	vegetation height
K	spring coefficient (ratio of force per unit volume and excursion from equilibrium position) of the vegetation
n	number of stalks per m^2
P	pressure
t	time
T	wave period
u	horizontal velocity of the fluid; u = dx/dt
u_v	velocity of the vegetation; $u_v = dx_v/dt$
w	friction coefficient relating the force (per unit volume) on the stalks to the difference in velocity of the fluid and the stalks.
x	horizontal coordinate (in the direction of wave propagation)
X	horizontal displacement of a water particle from its average position
X_v	horizontal displacement of the vegetation from the equilibrium position
z	vertical coordinate (z=0 at the bottom)
z_v	representative level in the vegetation layer ($=c_v * Min(h_v,d)$)
δ	diameter of the stalks of the vegetation
θ	propagation direction of a wave component
η	vertical position of the surface
ρ	mass density of the fluid
σ	relative angular frequency of the wave motion
ω	(absolute) angular frequency of the wave motion $\omega = 2\pi/T$

2.2.5 EP5 - Algorithm for vegetation friction factor (WLD-de Vries)

Aim To improve the accuracy of the SWAN wave model for situations where submerged or emergent vegetation is occurring, based on species specific vegetation characteristics.

Scientific background
The wave model SWAN uses the Collins (Collins, 1972) friction coefficient for calculating wave transmission over unvegetated bottoms. This friction coefficient is not a priori suited to include the effect of vegetation on wave transmission. In our study it is shown that this friction coefficient is, except for a constant factor, the same as an alternative vegetation friction coefficient that can be calculated on the basis of vegetation characteristics, stem diameter, plant height, plant density and a species specific drag factor.

This approach has been tested by a comparison between the dissipations predicted by the alternative friction coefficient and the dissipations measured in a field experiment. This resulted in quite satisfying correlations; correlation coefficients of about 0.6 – 0.8 were calculated.

Improvement in understanding
Utilisation of the vegetation friction coefficient allows the user to analyse wave dissipation over vegetated areas. Based on field experiments, this coefficient has been calibrated for *Spartina* dominated emergent vegetation. From this, it has now become possible to predict wave dissipation with the SWAN model for saltmarshes using vegetation and plant characteristics.

Implementation
When entering shallow water, the wave spectrum is strongly affected by the bottom through shoaling, refraction, diffraction, reflection and bottom friction. In finite-depth water, nonlinear effects such as depth-induced wave breaking or wave-wave interactions arise. The nature of the bottom and the topography have a strong impact on the near shore wave field. A rough or irregular bottom will induce larger wave dissipation than a smooth, flat bottom. The process of wave energy dissipation at the seabed can be modeled by the action of a stress on the water moving at a given velocity just above the boundary layer (Putnam and Johnson, 1949).

As a basis for theoretical formulation for dissipation due to vegetation, the theoretical relation of bottom dissipation will be described, following the formulations of Van Rijn (1989). The dissipation is equal to the time-averaged work done by the friction force at the bottom, giving:

$$D_f = \frac{1}{T}\int_0^T \tau_b \cdot U_\delta \cdot dt \qquad (1)$$

Where
D_f - Dissipation by bottom friction
τ_b - Bed shear stress
U_δ - Current velocity just above boundary layer

T - total duration

In the case of wave action, substitution of

$$U_\delta = \hat{U}_\delta \cdot \sin(\omega t) \tag{2}$$

and

$$\tau_b = \frac{1}{2}\rho \cdot f_w \cdot \hat{U}_\delta^2 \cdot \sin^2(\omega t) \tag{3}$$

where:
f_w - friction coefficient
$\hat{U}_\delta$ - maximum velocity near boundary layer
ρ - mass density of the fluid
ω - (absolute) angular frequency of the wave motion ω = 2π/T

yields:

$$D_f = \frac{\rho f_w \hat{U}_\delta^3}{2T}\int_0^T \sin^3(\omega t)dt = \frac{4}{3\pi}\rho \cdot f_w \cdot \hat{U}_\delta^3 \tag{4}$$

This formulation shows that dissipation due to bottom friction is related to a friction coefficient f_w and the third power of the amplitude of the horizontal orbital velocity at the bottom, $\hat{U}_\delta$ (from now on referred to as U_{orb}). This equation is the basis of the following approach to describe wave energy dissipation as a function of some vegetation characteristics:

First we define the force on a single stem of height dz, assuming a uniform $\hat{U}_{orb}^2$ as:

$$F_{ss} = \frac{1}{2}\rho \cdot f_w^* \cdot D \cdot dz \cdot \hat{U}_{orb}^2 \cdot \sin^2(\omega t) \tag{5}$$

where:
F_{ss} - force exerted on a single stem of vegetation
f_w^* - vegetation friction coefficient
D - stem diameter
dz - average vegetation height
$\hat{U}_{orb}^2$ - maximum horizontal orbital velocity

The stress τ_v on the vegetation with height dz, per unit area, depends on the density of stems n.

$$\tau_v = \frac{1}{2}\rho \cdot f_w^* \cdot D \cdot dz \cdot n \cdot \hat{U}_{orb}^2 \cdot \sin^2(\omega t) \tag{6}$$

where:

τ_v - stress caused by vegetation friction
n – number of stems per unit area

The energy dissipation per unit area, integrated over the vegetation height dz, assuming constant density, becomes:

$$D_v = \frac{4}{3\pi} \rho \cdot U_{orb}^3 \cdot f_w^* \cdot D \cdot n \cdot dz \tag{7}$$

where:
D_v - dissipation of energy per unit area of vegetation

In this approach four vegetation characteristics are included, $f_w^*, D, n \text{ and } dz$. Vegetation density, stem diameter and vegetation height. The friction factor f_w^* is still dependent on other species specific characteristics such as the stiffness and the roughness of the plant surface that are not further elaborated upon in this work.

In a simplified case, with shallow water wave conditions and constant plant density in height, the total vegetation friction factor c_v equals:

$$c_v = f_w^* \cdot D \cdot n \cdot dz \tag{8}$$

where:
c_v - vegetation friction factor

Our aim is now to prove the validity of replacing the bottom friction factor c_f that is used in SWAN with the vegetation friction factor c_v. For that purpose, SWAN wave dissipation due to bottom friction (equation 11) will be rewritten to a form comparable to the way wave dissipation is described according to Van Rijn (equation 4).

$$S(\omega,\theta) = -C_{bottom} \frac{\omega^2}{g^2 \sinh^2(kh)} E(\omega,\theta) \tag{9}$$

where:
S - wave dissipation
θ - propagation direction of a wave component
C_{bottom} - bottom friction coefficient
g - acceleration due to gravity
k - wave number (=2π/wavelength)
h - water depth
E - total wave energy density

The expression of Collins (1972) is based on a conventional formulation for periodic waves with the appropriate parameters adapted to suit a random wave field. The dissipation rate is calculated with the conventional bottom friction formulation of equation 11 in which the bottom friction coefficient is

$$C_{bottom} = c_f \cdot g \cdot U_{orb} \tag{10}$$

where c_f is the Collins friction factor

From equation 9 and 10 it follows that:

$$S_{ds,b}(\omega,\theta) = -c_f U_{orb} \frac{\omega^2}{g \sinh^2(kh)} E \tag{11}$$

The sum of the potential and the kinetic energy density is calculated by:

$$E = \frac{1}{8}\rho g H^2 \tag{12}$$

where:
H - root-mean-square wave height

With ω (= $2\pi/T$) and E according to 12, formula 11 can be rewritten as:

$$S(\omega,\theta) = -c_f U_{orb} \cdot \rho \cdot H^2 \frac{\omega^2}{8 \sinh^2(kh)} \tag{13}$$

Furthermore, from linear wave theory it is known that:

$$U_{orb}(z) = \omega \cdot H \frac{\cosh k(h+z)}{2 \sinh kh} \tag{14}$$

where:
z - height above bottom

Approaching the bottom, thus $z = -h$, the horizontal velocity amplitude becomes:

$$U_{orb}(z) = \frac{\omega \cdot H}{2 \sinh kh} \tag{15}$$

With this formulation, equation 13 can be written as follows:

$$S_{ds,b}(\sigma,\theta) = -c_f U_{orb} \cdot \rho \cdot \frac{1}{2} \cdot U_{orb}^2 = -\frac{1}{2} \cdot c_f \cdot \rho \cdot U_{orb}^3 \tag{16}$$

This last equation shows a great similarity with the way dissipation was described by Van Rijn (see equation 4). The slight differences are:

- the minus sign in the SWAN expression. This is just a result of how dissipation is defined. In SWAN a negative dissipation causes a decrease in wave energy density, while in the approach of the previous chapters positive dissipation has been interpreted as the cause of energy loss
- the second difference is the factor ½. In the van Rijn formulation this factor is slightly different, namely $4/(3\pi) \approx 0{,}42$.

The great similarity in the two formulations of wave energy dissipation gives a good opportunity to make SWAN suitable for vegetation influence by *replacing* the Collins friction factor c_f by the alternative vegetation friction factor c_v. Table 1 shows some results after calibrating the SWAN model to field data. It is clear that this factor is much higher then the value usually used for c_f, 0.015. f_w^* proves to be fairly constant, due to the fact that *Spartina anglica* is dominating the local vegetation.

Table 1 Vegetation friction factors calculated for 6 different field locations(P0-P5) based on shallow water wave theory, with constant vertical density of vegetation

Location	dz *cm*	D *mm*	n 1/m^2	f_w^*	c_v
P0	42	4,3	872	0,90	1,41
P1	30	3,5	796	0,90	0,75
P2	38	3,9	620	0,90	0,83
P3	34	2,9	1476	0,89	1,29
P4	36	3,9	1308	0,89	1,64
P5	31	3,8	1704	0,88	1,76

Limits of applicability
The algorithm has been tested for *Spartina anglica* dominated vegetations.

Validation
The effectiveness of the algorithm was investigated by application of the SWAN model to a transect in the Paulinaschor area in the Western Scheldt (NL). For this transect data on plant height, density, stem diameter were collected. In the same transect wave data were measured.

At first the Collins friction coefficient was used for calibration of the 1DH model. Values for this factor turned out to be 2 orders of magnitude bigger than the default value, for unvegetated bottoms. Using the calculated alternative friction coefficients, the SWAN model has been validated. The model results showed a good agreement with reality, but that agreement has not been quantified. Only the wave attenuation at the edge of the salt marsh did not correspond very well with the observed attenuation. A possible explanation could be that vegetation is modelled in SWAN through an enlarged bottom friction, instead of 3D obstacles. Also due to the fact that the development of the orbital velocity in the vegetation is not known exactly, deviances between model outcome and observed attenuation may occur.

References
Booij, N., R. C. Ris, and L. H. Holthuijsen, A third-generation wave model for coastal regions : 1. Model description and validation, *J. Geophys. Res., 104*, 7649-7666, 1999.

Collins, J. I., Prediction of shallow water spectra, *J. Geophys. Res., 77,* 2693-2707, 1972.

WL | Delft Hydraulics, 2003. Wave attenuation in vegetation. Author: A. Mol. Project reference Z2837.

Putnam, J. A. and J. W. Johnson, The dissipation of wave energy by bottom friction, *EOS Trans. AGU, 30,* 67-74, 1949.

Van Rijn, L. C., 1989. Handbook of Sediment Transport by Currents and Waves. Report No. H461, Delft Hydraulics.

2.2.6 EP6 - Algorithm for relationship between intertidal surface properties and H/h ratio limit (CCRU- Möller)

Aim To provide data based relationships between wave height and water depth on mudflat and saltmarsh. To establish the maximum limit to observed H_{rms}/h ratios over a range of intertidal surfaces with differing frictional characteristics.

Scientific Background
Recent research has shown that surfaces are capable of dissipating more than 90% of the incident total spectral wave energy over short (several 10s of meters) distances (Moeller et al. 1996, Möller *et al*. 1999, 2002). Patterns of wave attenuation over cliffed marsh edges correspond to patterns observed in previous physical scale model experiments, although dissipation landwards of the cliff face is less pronounced in the field. Over 'ramped' mudflat-to-saltmarsh transitions dissipation is initially less pronounced but once waves reach the permanently vegetated surfaces further landwards, dissipation exceeds levels predicted by earlier physical scale model experiments.

Spectral summary parameters (e.g. significant wave height, total spectral energy) provide useful indicators of the energy dissipation potential at the marsh-wide scale. The ratio between root-mean-square wave height (H_{rms}) and water depth (h) is controlled by the counteracting processes of shoaling (increasing H_{rms}/h ratios) and energy losses through bed friction or viscous damping (decreasing H_{rms}/h ratios).

Benefits from EstProc
Figure 1 was derived from an analysis of data from the Dengie Peninsula, Essex, available to EstProc. Instrument location PT1 was near the seawall and instrument PT14 was situated a distance offshore of about 290 m from PT1; the zonation of the saltmarsh is given in the figure and PT9 and PT10 lie in the area of seasonal saltmarsh vegetation. It strongly suggests that the H_{rms}/h ratio is constrained by an upper limit determined by bed characteristics along the mudflat to saltmarsh transition. The limiting values of the ratio are plotted in Figure 1.

Thus, for example, on the mudflat at Tillingham, Essex, shoaling dominates over frictional energy losses (viscous damping being of minor importance on a mudflat composed of well-consolidated sediment), leading to an increase in the maximum achievable H_{rms}/h ratio. This tendency also characterises the transition zone of seasonal vegetation cover, where changes in water depth are minimal (<10cm) and a well-developed mud-mound topography is present. Over the first 20m of permanently vegetated marsh surface, however, the additional frictional losses appear significant enough to reduce H_{rms}/h ratios to < 0.15 derived from Le Hir *et al*.'s (2000) study of the Brouage mudflat, France.

Limits of applicability
The relationships above are empirically derived from a finite data series. Their validity is thus limited geographically to the particular site at Dengie, Essex, although there is some evidence (e.g. Le Hir *et al*. (2000)) that the relationships contained in this algorithm are of more general application.

Intra-annual variability in energy dissipation patterns suggests that variations in vegetation canopy structure and biomass may influence dissipation rates. Progress has been made in EstProc in modelling this dissipation process over vegetated saltmarsh surfaces in the upper intertidal zone using new algorithms in the SWAN model. Using a modified Collins coefficient, which mimics the change in vegetation characteristics across marsh surfaces as community composition changes. It has been possible to develop a dedicated coefficient for vegetation within SWAN (see EP3, Section 2.2.3).

Gaps in knowledge

As mentioned above, there is a need to test the validity of the above relationships at other locations and for other marsh types before they can be fully and more generally accepted as input into numerical models. It is also necessary to develop improved empirical methods for the quantification of surface properties (vegetation and topographic characteristics) and their relationship to hydrodynamic surface roughness. Some progress towards this aim has been achieved within EstProc (see EP3, Section 2.2.3).

References

Le Hir, P., Roberts, W., Cazaillet, O., Christie, M., Bassoullet, P, and Bacher, C. 2000. Characterization of intertidal flat hydrodynamics. Continental Shelf Research 20, 1433-1459.

Möller, I. and Spencer, T. 2003. Wave transformations over mudflat and saltmarsh surfaces on the UK east coast – Implications for marsh evolution. Proceedings, International Conference on Coastal Sediments 2003 (ASCE, World Scientific Publishing Corp. and East Meets West Productions : Corpus Christi Texas).

Möller, I., Spencer, T. and Rawson, J. 2002. Spatial and temporal variability of wave attenuation over a UK East-coast saltmarsh. Proceedings of the 38th International Conference on Coastal Engineering, Cardiff, July 2002.

Möller, I., Spencer, T., French, J.R., Leggett, D.J. and Dixon, M. 1999. Wave transformation over salt marshes: A field and numerical modelling study from North Norfolk, England. *Estuarine, Coastal and Shelf Science* 49, 411-426.

Moeller, I., Spencer, T. and French, J.R. 1996. Wind wave attenuation over saltmarsh surfaces: Preliminary results from Norfolk, England, *Journal of Coastal Research* 12(4), 1009-1016.

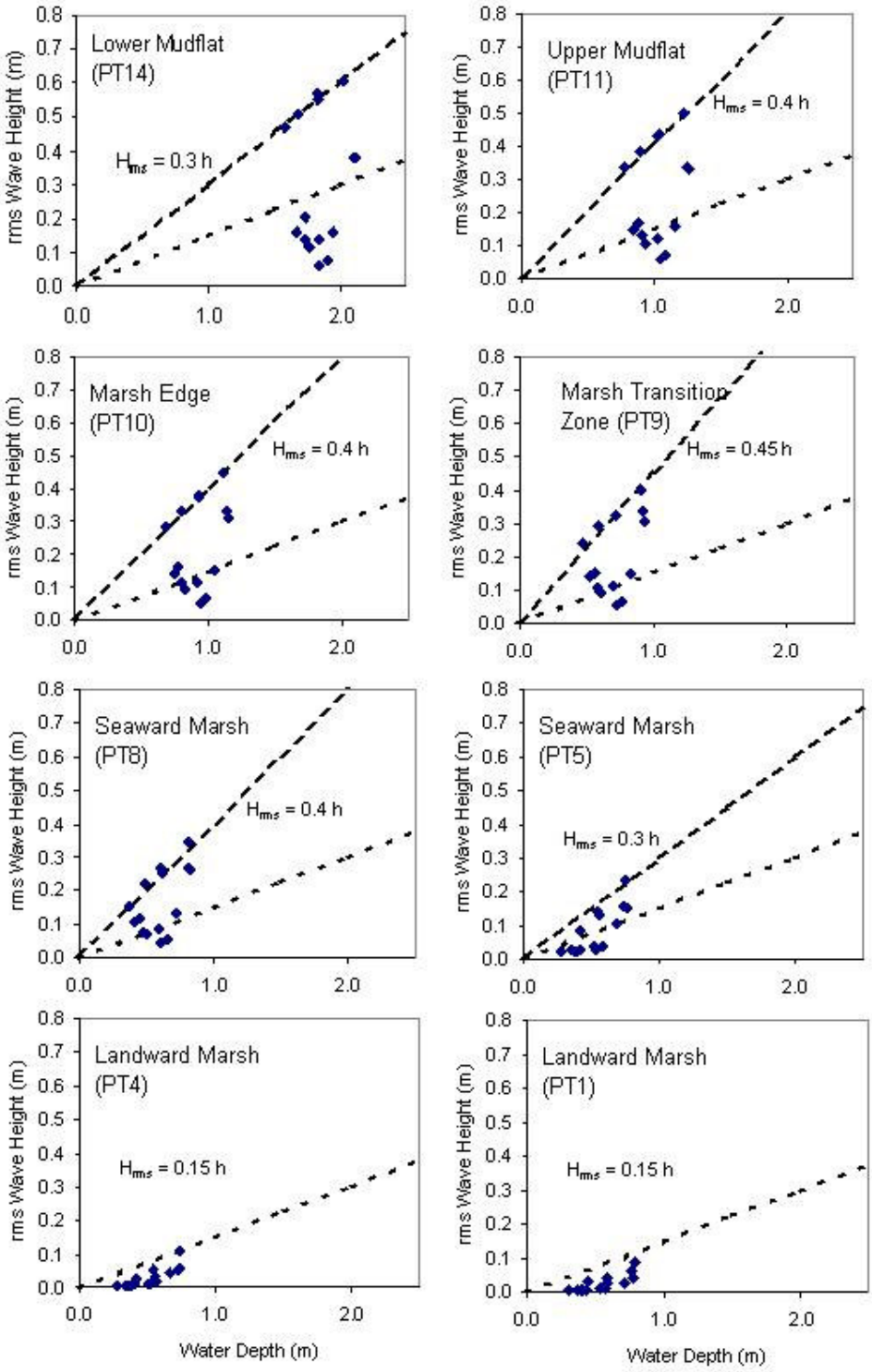

Figure 1 Relationship between root-mean-square wave height (H_{rms}) and water depth (h) for selected locations along the intertidal transect at Tillingham, Essex. PT 1 is located near the seawall and PT 14 is 290 m offshore

Relationship (algorithm level 1) between root-mean-square wave height (H_{rms}) and water depth (h) for selected locations (solid triangles) along the intertidal transect at Tillingham, Essex (after Möller and Spencer 2003). Also plotted on this figure are (a) lines (fine dotted) that represent the ratio H_{rms}/h of 0.15 found by Le Hir et al. (2000) to apply to maximum wave heights on the Brouage mudflat in France, and (b) lines (bold dotted) that may represent a similar limiting H_{rms}/h of different magnitude for the respective locations on the Tillingham, Essex transect.

2.3 Prediction of the impact of extreme events and major anthropogenic influences

2.3.1 EP7 - Algorithm for modelling flow in dendritic systems – porosity method (HRW-Spearman)

Aim To develop an effective method based on cross-section "porosity" for modelling flow in the dendritic channels found in the saltmarsh and mudflat areas of an estuary.

Scientific background
Dendritic systems (which for the sake of this study effectively means saltmarsh and mudflats, although the general principles apply to all such systems) have irregular bathymetry which can vary significantly over length-scales of 1m or less. These small length scales are considerably less than the practically viable scales of 2D flow model grids for applied modelling. For (non-research) estuary modelling scales are typically of the order of 50-100m in estuaries (and greater for large systems)

The inability of applied models to reproduce the small-scale variation in bed levels can result in a poor overall description of flow through grid cells representing flow through highly varied bed topography, since the bed is represented by a single level throughout the cell. A single level cannot both adequately represent the total storage and the deepest channel through the cell. Usually the bed level is "averaged" meaning that the model represents flow through the grid cell later in the tide than the real situation. This can result in a poor representation of flow through the (saltmarsh or mudflat) system as a whole, especially as it drys and wets. Moreover in an estuary system or tidal inlet dominated by significant and small-scale bathymetric variation these problems can result in a generally poor simulation of flows in the system.

The normal course of action open to the numerical modeller is to enhance the grid resolution over the dendritic portion of the mudflat/saltmarsh up to the point where the flow within the system becomes acceptably similar to the observations. However higher grid resolutions lead to larger numbers of nodes and smaller mesh elements, which can lead to unacceptably long run times.

The new algorithm, developed in EstProc, and described below, includes the effect of the small-scale bathymetric variation on flows without increasing the mesh resolution. This type of approach is termed "sub-grid" modelling.

Improvement in understanding
The new method improves on existing methods because:

- it can significantly improve the accuracy of the flow model results, especially within the saltmarsh
- the increase in run times is only of the order of 15%-25%.

Implementation
The algorithm makes use of the TELEMAC-2D flow model software which allows the specification of the porosity of flow within a model element. Here the algorithm is written in a step-by-step "recipe" style, which can easily be coded for any computer application (assuming porosity is included in the form of the continuity and momentum

equations which the model is solving). The method samples the local bed elevation data within a specified search radius to determine the associated value of porosity.

The TELEMAC-2D software implements a FORTRAN file (called "princi.f") which governs the way initial and boundary conditions are implemented within the model. This princi.f file also implements the routine that specifies porosity if required. The algorithm is implemented within two of the subroutines which form the princi.f file:

- CORFON (where the initial bathymetry is specified) and POROS (where the porosity is set).

Algorithm

Inputs
High resolution bathymetry data set (m datum)

Outputs
Minimum bed level for each model node (m datum)
Porosity for each model element (no units)

1 Using the appropriate mesh generator, generate the mesh and bathymetry for the available data set.

2 Calculate the required search radius. This should be done by trial and error but as a starting point the following search radius is suggested (for meshes with triangular elements):

$$\mathrm{SR} = \frac{1}{2\sqrt{3}} < \text{grid resolution} >$$

3 Locate all the bathymetric points within the specified search radius for each model node.

4 Redefine the bathymetry so that, as long as one data point or more is found within the search radius, the bathymetry at each model node is altered to the lowest elevation from those points within the search radius.

5 Define two arrays:
ncount(i) , the number of bathymetric points corresponding to node i
zcount(i,k) , the level of the kth bathymetric point at node i

6 Sort the values of zcount(i,k) so that the lowest elevation is zcount(i,1) and the highest elevation is zcount(i,N).

7 On each time step …

For each node …

Calculate

$$A(i) = \sum_{k=1,j} k.\min(zcount_{k,i}, fs_i) \qquad P(i) = \max\left(\frac{A(i)}{H(i)}, 0.5\right)$$

where j is given by $zcount_{i,j-1} < fs_i < zcount_{i,j}$;
$zcount_{k,i}$ is the k^{th} elevation for the i^{th} node ;
fs_i is the free surface elevation at node i;
P is the porosity associated with node i.

(necessary for TELEMAC software)
Calculate the porosity of each element

$$PE_m = \frac{1}{3} P_{m,1} + \frac{1}{3} P_{m,2} + \frac{1}{3} P_{m,3}$$

where PE_m is the porosity associated with the m^{th} element;
$P_{m,1}$ etc are the porosities associated with the three nodes corresponding to the m^{th} element.

Limits of applicability
The algorithm is applicable where there is high resolution bathymetric data (i.e. where the resolution of bathymetric measurements is significantly greater than the model grid resolution).

Validation
The studies described above suggest that the sub-grid methodology will improve the representation of flows both within saltmarsh systems and in estuaries containing such systems. For a given resolution, however, the results of this study suggest that the method can only *partially* overcome the inaccuracy introduced by coarser resolution. It should be noted that these results are derived from only one specific estuary and further use of the method in different environments is recommended.

The method was consistently successful at improving flows within the saltmarsh but no objective improvement in flows in the main channel outside of the saltmarsh was discernible. Moreover, outside of the saltmarsh the improvements in accuracy due to the method varied from significant improvement to significant deterioration in accuracy and no clear pattern could be observed with variation in location.

The usefulness of the method must be judged against the improvements that can be brought to a model be merely increasing grid resolution. For coarser resolutions (the definition of which may vary from model to model) the suggestion is that (in terms of improved accuracy for a given run time) the method may be less effective than increasing intertidal resolution. At higher resolutions the run times increase rapidly while the corresponding increase in accuracy from the ever-increasing resolution reduces. It is for these situations that the method seems best suited.

The effectiveness of the algorithm was investigated using a TELEMAC-2D model of Salcott Creek in the Blackwater Estuary (Spearman et al, 2004). Model results derived using the algorithm were compared objectively using the Brier Skill Score method – see Sutherland and Soulsby (2003) - against model results derived without the method, and with a reference data set generated using a very high resolution model. The new method was shown to be effective but the level of quantifiable benefits depend on the baseline result used in the Brier Skill Score calculation, and varies spatially within the estuary.

References
Hervouet J, Samie R and Moreau B (2000), Modelling urban areas in dam-break flood-wave numerical simulations, International seminar and workshop on rescue actions based on dam-break flood analysis, 1-6 October 2000, Seinäjoki, Finland.

HR Wallingford (2001), Sustainable Flood Defences. Monitoring of Retreat and Recharge Sites, Project Number MRD 21110, Abbott's Hall, Numerical Modelling, HR Wallingford EX Report 4367, August 2001.

Spearman J R, Baugh J and McCoy M J (2004), Use of sub-grid approaches in the modelling of estuaries with salt marsh systems, HR Wallingford Report TR138, January 2004.

Sutherland, J. and Soulsby, R.L., (2003). Use of model performance statistics in modelling coastal morphodynamics, Proceedings of the International Conference on Coastal Sediments 2003, CD-ROM Published by World Scientific Publishing Corp. and East Meets West Productions, Corpus Christi, Texas, USA. ISBN 981-238-422-7.

2.3.2 EP8 - Algorithm for modelling flow in dendritic systems – Raster model (ABP-Swift)

Aim To develop an effective method based on cross-section "porosity" for modelling tidal flows in the dendritic channels found in the saltmarsh and mudflat areas of an estuary.

Raster Model

(a) Flow between adjacent cells in the X-direction (coupled solution)

Equation (1) is based on the work of Horritt and Bates (2001) but includes the corrected free surface gradient terms referred to in the supporting technical report, ABPmer (2004). The equation is presented in finite difference nomenclature for a two-dimensional grid where $H^{i,j}$ represent the water free surface elevation in cell *(i,j)* of a rectangular grid, whose dimensions are Δx and Δy in the x and y directions respectively. The discharge Q across a cell boundary in the x direction is given by:

$$Q_x^{i,j} = \frac{C\Delta y \cdot h^{3/2} \dfrac{H^{i-1,j} - H^{i,j}}{\Delta x}}{[\{(H^{i-1,j} - H^{i,j})/\Delta x\}^2 + \{(H^{i,j-1} - H^{i,j+1})/2\Delta y\}^2]^{1/4}} \quad (1)$$

The Chézy roughness coefficient, C, has been used in preference to the Manning solution. The variable h represents the depth of flow across the interface between the two adjacent cells. The left hand cell is at index position *(i-1,j)* and the cell to the right of the cell interface is at index *(i,j)*. Flow is positive from left to right, with advancing x. A similar equation can be developed for flow in the Y-direction.

(b) Flow between adjacent cells in the X-direction (uncoupled solution):

If the flows in the x and y directions are treated as uncoupled, then a one dimensional solution can be recovered from equation *(1)* by setting $H^{i,j-1}$ equal to $H^{i,j+1}$ thus:

$$Q^{i,j} = C\Delta y \cdot h^{3/2} \left[\frac{H^{i-1,j} - H^{i,j}}{\Delta x} \right]^{1/2} \quad (2)$$

Again a similar result applies in the Y-direction.

(c) Flow between adjacent cells in the x direction (uncoupled solution with conservation of specific energy):

Inspection of equation *(1)* reveals that flow rates tend to increase indefinitely as the roughness of the bed progressively decreases. The reason for this is that the variation in specific energy between adjacent cells has been neglected. The effects of conservation of specific energy between cells are incorporated in the raster solution through the modified expressions provided in equation (3). The coefficient Z_e is a correction to the original solution which permits the conservation of specific energy in one dimension and regulates the magnitude of predicted current velocities:

$$Q^{i,j} = C\Delta y \cdot h^{3/2}\left[\frac{H^{i-1,j} - H^{i,j}}{\Delta x}\right]^{1/2} / Z_e$$
$$Z_e = \left[1 + \frac{C^2 h^3}{2g\Delta x}\left(\frac{1}{(y^{i+1})^2} - \frac{1}{(y^i)^2}\right)\right]^{1/2} \quad (3)$$

and similarly for the Y-direction.

Validation

Test results were presented for the application of the cellular model to two non-uniform bathymetry scenarios. The first test result from a planar sloping beach showed a satisfactory level of agreement with the results of an earlier one-dimensional model. The second test result was an application to Tom Tiddlers creek near Calshot Creek in Southampton Water. There was an encouraging comparison with field records of water levels and current speeds. One problem encountered was the progressively smaller time step required for increasing tidal range, in order to maintain run stability. A post-processing smoothing application was applied to provide a solution to this problem.

Implementation

More details of how the method is implemented are found in the report ABPmer (2004).

References

ABPmer (2004). Hydrodynamic Cellular Models of Tidal Regimes, Report R.1091.

Horritt, M.S. and Bates, P.D. 2001. Predicting floodplain inundation: raster-based modelling versus the finite element method. *Hydrological Processes, **15***: 825-842.

2.3.3 EP9 - Algorithm for the impact of Global Climate Change and Extreme Events in Estuaries (POL-Prandle)

Aim To utilise analytical relationships for estuary form and process to investigate the impact of Global Climate Change and Extreme Events in estuaries.

Summary
Consequences of Global Climate Change may include changes in:

- mean sea level, magnitude and frequency of storm events (surges, waves, river flow) and supply of sediments.

In this algorithm we have explored likely sensitivities of estuaries of differing size and shape to these changes with particular emphasis on associated flood risks in extreme events.

Based on existing experience, we do not expect dramatic changes in UK estuarine responses to tides or surges from the projected impacts of Global Climate Change over the next few decades. Some enhanced sensitivity might be found in relation to shorter 'period' (6 hr) surges associated with secondary depressions on the West Coast, particularly in larger estuaries. Likewise, maintaining fixed defences alongside continuous increases in mean sea level may enhance surge response in the shallowest estuaries.
Increases in mean river flows will produce corresponding proportionate reductions in flushing times. In the absence of 'hard geology', enhanced river flows may result in increases in estuarine lengths and depths, though with the proportional increases less than half that of the change in river flow and developing over decades.

The influences of changes in wave climate are more complex and spatially variable within any particular estuary. The potential influence on the nature of sea-bed sediments and associated flora and fauna could, in some cases, be both abrupt and dramatic.

1. Range of Estuary Shapes

We adopt three characteristic shapes (Figure 1) namely: BAY, LINEAR and FUNNEL described by axial, x, variations in breadth and depth increasing in proportion to $x^{½}$, x and $x^{3/2}$ respectively. These shapes correspond to values of the bathymetric parameter, ν, (Prandle & Rahman 1980, subsequently PR) of 1, 2 and 5, i.e. almost the complete range of estuaries encountered.

2. Tide and surge heights

Figure 3(b) of PR showed that over this range ($1< \nu < 5$), amplification of tides (and surges) between the first 'node' and the head of the estuary can be up to a factor of 2.5. Concern focuses on conditions in estuaries where the bathymetric dimensions (length, depth and shape) and excitation 'period', P, result in the estuarine mouth coinciding with this node with consequent resonant amplification. This occurs when

$$y = 0.75\,\upsilon + 1.25 \qquad (1)$$

with

$$y = \frac{4\,\pi\,L}{P\,(2-m)\,(g\,D)^{1/2}} \qquad (2)$$

where L and D are the estuarine length and depth (at the mouth), and m is the power of axial depth variation (0.5, 1 or 1.5 noted above).

Figure 2 indicates the corresponding resonant periods for a range of both L and D. Results for m = 1 are within 10% of those for m= 0.5 and m= 1.5, hence only those for m = 1 are shown. By utilising the formula

$$L = \frac{120}{f^{1/2}}\, D^{5/4} / \zeta^{1/2} \qquad (3)$$

derived by Prandle (2003),with f the bed friction coefficient (assumed ~0.0025) and ζ tidal elevation amplitude, values of L and D consistent with resonance at the M2 tidal period (12.42 h) can be calculated. These are shown in Table 1.

Table 1 Values of depth D, at the mouth, and length L consistent with resonance at M2 tidal frequency

ς (m)	2	2	4	4
	D(m)	L(km)	D(m)	L(km)
BAY m = 0.5	33.5	193.3	84.4	306.8
LINEAR m = 1.0	29.8	167.3	75.1	265.4
FUNNEL m = 1.5	26.3	142.7	66.2	226.4

These results show that resonance at semi-diurnal frequencies will only occur for $D \geq 20$ m and $L \geq 140$ km. The tidal reach of the Thames is approximately 95 km and the Humber 60 km. Hence, we only anticipate resonance for the semi-diurnal frequency in systems such as the Bristol Channel where the estuarine 'resonance' extends to the adjacent shelf sea. Thus, we do not expect dramatic changes in tide and surge responses in UK estuaries for anticipated changes in sea level of up to 1 m. Likewise increases in flood levels within estuaries are likely to be of the same order as the respective increases in adjacent open-sea conditions.

Some exception to the above is possible for surge response to secondary depressions (prevalent along the West Coast, Proctor & Flather, 1989) which can have effective periodicities of significantly less than 12 hours and hence may have resonant responses as indicated in Figure 2.

3. Intervention

Prandle (1989) examined the change in tidal response in estuaries due to variations in mean sea level where the location of the coastal boundaries remain fixed (i.e.

construction of flood protection walls). The results show the largest impacts will be in flat, shallow estuaries.

4. Effects of changes in river flow

For tidally-mixed estuaries with m = 0.8 (synchronous), Prandle (2003), the following relationship between river flow, Q, and depth at the mouth, D was derived (Prandle 2004a).

$$D = 12.8\,(Qa)^{0.4} \tag{4}$$

Where 'a', the transverse slope of the inter-tidal zone, is typically $0.01 > a > 0.001$. Hence we anticipate changes in depth δD for changes in flow δQ,

$$\frac{\delta D}{D} = 0.4\,\frac{\delta Q}{Q} \tag{5}$$

Moreover, since the same study derived the relationship (3) for estuarine length proportional to $D^{5/4}$, this indicates changes in estuarine length δL,

$$\frac{\delta L}{L} = 0.5\,\frac{\delta Q}{Q} \tag{6}$$

While such morphological adjustments might occur over decades, more immediate adjustment to salinity intrusion and associated mixing of fluvial contaminants might be expected. Since flushing times, F_T, are inversely proportional to Q (Prandle 2004b) we expect changes δF,

$$\frac{\delta F}{F} = -\frac{\delta Q}{Q} \tag{7}$$

5. Change in sediment supply

Changes in the nature and supply of marine sediments, here we assume the supply of fluvial sediments to most UK estuaries is negligible in terms of its influence on morphology, can lead to abrupt changes in estuarine morphology. This supply can directly determine the nature of the surficial sediments and thereby bed roughness. Peculiarly, the derived relationship (4) between depth at the mouth and river flow is independent of bed roughness. However, from (3), the associated estuarine length should vary according to:

$$\delta L \big/ L = -\frac{1}{2}\,\delta f \big/ f$$

i.e. estuaries will shorten as sediments become coarser.

6. Changes in wave climate

Enhanced wave heights in shelf seas can increase the effective sea-surface roughness and thus increase surge heights. Conversely, in shallow water, waves may increase sea-bed roughness and reduce tide and surge heights. These same effects will occur within estuaries with some accompanying longer-term adjustments of flora and fauna

(particularly salt marshes). Net effects within estuaries may show significant small scale variability, reflecting the additional exposure to wind (and wave) direction.

Validation

The validation of these methods is being furthered in Defra project FD2107. The methods are constructed to help understand the behaviour of estuaries rather than to provide accurate predictions.

References

Prandle, D & Rahman, M. (1980) Tidal response in estuaries, J Physical Oceanography 10(10), 1552-1573

Prandle, D. (1989) The impact of mean sea level change on estuarine dynamics. Proc. 13th Congress IAHR, Ottawa, Canada

Prandle, D. (2003) Relationships between tidal dynamics and bathymetry in strongly convergent estuaries. J Physical Oceanography, 33, 2738-2750

Prandle, D. (2004a) How tides and river flows determine estuarine bathymetries. To appear in Progress in Oceanography

Prandle, D. (2004b) Saline intrusion in partially mixed estuaries. Estuarine, Coastal & Shelf Sciences, 59, 385-397

Proctor, R. & Flather, R.A. (1989) Storm surge prediction in the Bristol Channel, the floods of 13 December 1981. Continental Shelf Research, 9, 889-918

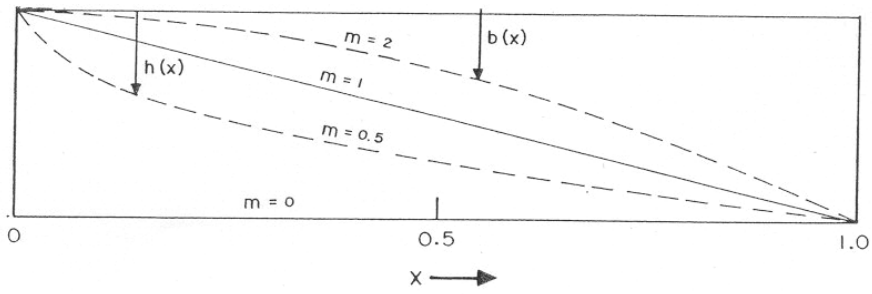

Figure 1 Estuarine dimensions proportional to xm**

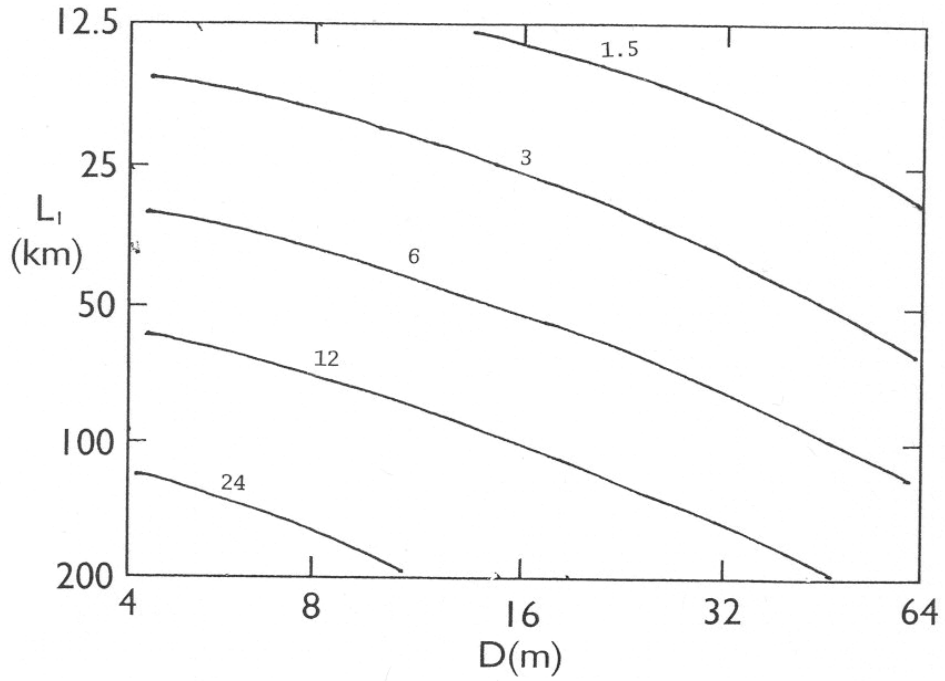

Figure 2 Contours of resonant periods (in hours) as f(D,L)

2.4 Results obtained from the interrogation of data

2.4.1 EP10 - Algorithms for salinity, velocity, SPM, and mudflat characteristics (PML-Uncles)

Aim To produce a set of algorithms for selected estuarine parameters from existing datasets analysed during the EstProc project. The work is listed here in sections A to E followed by the corresponding separately numbered algorithms.

A. The influences of weather, freshwater runoff (especially strong runoff) and tides on water levels and salinity intrusion at two sites in the upper Tamar Estuary were investigated. Results are presented for data measured at high water (HW) during 1988 and 1989, together with numerous along-estuary salinity surveys in the Tamar during 1981, 1982 and 1985.

- Salinity intrusion in the Tamar:
  - Salinity intrusion was strongly related to runoff, with less dependence on tidal range.
  - Salinity stratification was strongly related both to runoff and tidal range.

- Peak near-bed salinity:
  - This was strongly, positively related to HW level at low runoff – the relationship was much weaker at higher runoff.
  - It was strongly, negatively related to runoff.
  - It was strongly related to longer-term (2 – 8 day) winds and atmospheric pressure.

B. Analyses of field surveys over intertidal areas in the central Tamar Estuary have been made to quantify the seasonal and tidal variability of some key physical and biological properties of intertidal mudflats and their dependence on hydrodynamics. The analysis also utilised a flow model, derived at PML, that had spatial, cross-sectional dependence (Uncles et al., 2003). There was insufficient time in this project to analyse data for wave behaviour.

- Velocity data:
  - Transverse distributions of longitudinal current velocity, derived from ADCP measurements over a cross-section, exhibited large differences in speeds and phases between the main channel and intertidal areas.
  - Even small amounts of channel curvature apparently produced striking differences in section morphology.
  - Model results showed strong similarities with measured data, such that main-channel currents were faster than those on the mudflats except around HW, at which time mudflat currents had started to ebb while main-channel currents were still on the flood.
  - The model results also showed that simulated currents on the upper mudflats, very near to the shorelines, were ebbing, if only very slowly, throughout their brief periods of submergence.

- Seasonal variations:
  - Seasonal variations in 'physical' mudflat properties were relatively small.
  - Biological variations were large and EPS (extra-cellular polymeric substances) in the surface 0.002 m had a dominating influence on the critical erosion threshold (CET) of mudflat sediment.
  - During 'bloom' conditions the stress exerted by water flows was too small to cause suspension of sediments, in the absence of waves, and the intertidal areas were depositional.

C. Analyses were made of longitudinal surveys along the upper Humber and Ouse, which can have a bore-like tidal wave in the upper reaches, which utilised profiling throughout the water column of salinity, suspended particulate matter (SPM) and temperature. The data included spring-neap, seasonal and tidal variability. The Humber-Ouse had a strong estuarine turbidity maximum (ETM) in its low salinity reaches (Uncles et al., in press (a)).

- Seasonal variations in SPM:
  - The ETM location and magnitude were strongly related to runoff and the spring-neap cycle. It was more than 50 km from the tidal limit in winter and less than 30 km in summer.
  - SPM stratification was related to runoff and tidal range and ceased only where SPM concentrations were very low, close to the tidal limit.
  - Fluid mud layers and stationary suspensions sometimes occurred near to the bed and SPM concentrations sometimes exceeded 100 g/l. These layers were stationary or had very slow current speeds within them.

D. Analyses were made of vertical profiles of temperature, salinity, velocity and SPM concentration and, occasionally, in-situ floc sizes over tidal cycles in the upper Humber and Ouse (Uncles et al., in press (a, b)).

- Vertical profiles of SPM:
  - At HW these profiles were characterised by flocculation and settling, with the largest flocs observed at mid-depth.
  - Strong seasonal variations in SPM concentrations were related to seasonal movements of the ETM.
  - Entrainment of flocs from near-bed suspensions during fast currents and strong shears led to their disruption.
  - Floc sizes in the ETM appeared to be smaller (~100 microns) than elsewhere in the estuary, although this remains to be confirmed.
  - Maximum floc sizes in the bulk of the water column (~ 500 microns) occurred down-estuary of the ETM, near mid depth at HW. Sizes there typically were 100-300 microns.
  - Floc sizes in near-bed stationary suspensions could exceed 800 microns.

E. Analyses have been made of the grain sizes of primary and flocculated suspended sediments and their particulate organic carbon content (POC) *via* loss on ignition (LOI), as well as of intertidal sediment properties along the Humber and Ouse (Uncles et al., in press (c)).

- Sediment characteristics:
  - SPM that comprised the ETM was largely inorganic (mineral) fine sediment (LOI ~10%).
  - The primary SPM was such that greater than 40% by volume of the solids was very fine silt and clay sized (< 4 μm) and greater than 20% (typically 30%) was < 2 μm (clay-sized).
  - Bed-sediment grain-sizes varied throughout the region and were much coarser than the SPM, although the great majority of bed sediment was smaller than 500 μm.
  - The dominant bed-sediment fraction down-channel of the ETM was fine sand; within the ETM the bed sediment was predominantly fine sand and very fine sand; up-estuary of the ETM the bed sediment was mainly very fine sand and compacted silt and clay-sized material.

- Seasonal variations in sediment properties:
  - A strong seasonal, longitudinal transport was found to occur both in subtidal and intertidal sediments.
  - Over the winter period, the up-channel margin of very fine sand moved down-estuary and left a scoured, highly cohesive mud bed.
  - Sand was transported back into the upper reaches by flood-dominant tidal currents during low inflow, summer and autumn periods.
  - The intertidal banks of the upper reaches utilised very fine sand to grow during summer and autumn.

Algorithms

1. **EP10.1:** *Regression relationships for suspended sediment and salt intrusion in terms of runoff for the Tamar*

   - Input of SPM from the River Tamar

There appears to be no correlation between freshwater SPM concentration and daily-averaged river inflow, Q_1, for flows less than 10 $m^3\ s^{-1}$, although a power-law dependence of SPM on inflow is fairly realistic at higher flows. The regression relationship is such that when $Q<10\ m^3\ s^{-1}$ the SPM concentrations, P, are 5 mg l^{-1}, whereas for higher inflows (Q_1 in $m^3\ s^{-1}$):

$P=5(Q_1/10)^{1.2}$ mg l^{-1}

   - Salt Intrusion

The location of the limit of saline intrusion (or freshwater-saltwater interface, FSI) at HW depends mainly on the freshwater runoff across the head of the estuary. The spring-neap influence is slight. The distance of the FSI from the head, X_S, is correlated with the daily runoff, Q_1. The FSI is taken here to be the point at which the 1-isohaline contour intersects the bed of the estuary. For runoff less than about 20 $m^3\ s^{-1}$ the FSI is less than 10 km from the head at HW of spring and neap tides. The regression relationship between FSI location at HW and freshwater runoff is:

$X_S = 3.6(Q_1)^{0.27}$ km

- ETM Location

The location of the ETM at HW of spring tides is usually associated with the FSI. When the freshwater runoff is less than about 10 m^3 s^{-1}, which typically is the case during summer periods, the ETM is located somewhat up-estuary of the FSI at HW. This separation is in the range 1-3 km and occurs when the FSI location at HW is less than about 7 km from the head; it is more pronounced when the FSI is close to the head. A regression relationship between the ETM location (X_P, km from the head) and daily runoff, Q_1, is:

$X_P = 1.7(Q_1)^{0.48}$ km

- Salt Intrusion and ETM Location in the Tavy

In the Tavy Estuary, which is 5 km long and a sub-estuary of the Tamar, the salt intrusion and the location of the ETM as functions of daily freshwater runoff Q_1 and tidal range TR (m) are:

$X_S = 0.96(Q_1/TR)^{0.40}$ km

and

$X_P = 0.82(Q_1/TR)^{0.80}$ km

2. **EP10.2:** *Regression relationships between various mudflat variables for the Tamar*

There were strong correlation relationships between several of the intertidal mudflat properties (Uncles et al., 2003).

- Silt and Clay Fraction

The percentage silt and clay within the upper 0.01 m of the sediment bed, SC, is strongly, negatively correlated with its bulk density, BD (g ml^{-1}). Therefore, finer sediment mixtures (greater silt and clay fractions) are able to hold more water (reduced bulk density) than coarser mixtures:

$SC = 295 - 171BD$ %

- Bulk Density

The bulk density, BD, within the upper 0.01 m of the sediment bed is strongly, negatively correlated with sediment moisture content (MC in % - the percentage mass of water to mass of dry sediment in a sample):

$BD = 1.57 - 0.00168MC$ g ml^{-1}

- POC

In the upper 0.01 m of the mud bed, the particulate organic carbon (POC, % of dry sediment) is strongly, negatively correlated with sediment bulk density. This demonstrates that finer sediment mixtures (with more water and reduced bulk density) are associated with a greater organic content (per unit mass of dry sediment) than coarser sediments:

$POC = 13.6 - 7.64BD$ %

- EPS

In the upper 0.002 m of the mud bed, the colloidal carbohydrate content of sediment (EPS, expressed as glucose equivalents in mg g^{-1} of dry sediment) is strongly, positively correlated with the chlorophyll-a fraction of the sediment (CH, in μg g^{-1} of dry sediment):

$EPS = -0.0317 + 0.0107CH$ mg g^{-1}

3. **EP10.3:** *Regression relationships for seasonal variations in SPM and Salt Intrusion in terms of runoff in the Humber-Ouse*

- Input of SPM from the River Ouse

There appears to be no correlation between freshwater SPM concentration and daily-averaged river inflow from the River Ouse, Q_1, for flows less than 25 m^3 s^{-1}, although a power-law dependence of SPM on inflow is fairly realistic at higher flows. The regression relationship is such that when Q<25 m^3 s^{-1} the SPM concentrations, P, are 5 mg l^{-1}, whereas for higher inflows:

$P = 5(Q_1/25)^{1.4}$ mg l^{-1}

- Salt Intrusion

A multiple regression of the location of the saline intrusion, X_S, in terms of Q_{31}, where Q_{31} is the inflow averaged over 31 days preceding the survey, explains much of the variance in X_S (see Uncles et al., in press):

$X_S = 21(Q_{31})^{0.23}$ km

- ETM Location

A multiple regression of X_P in terms of Q_{31} and TR explains much of the variance in X_P. Both variables have a statistically significant influence on X_P. Increasing Q_{31} increases X_P so that the ETM moves down-estuary. Increasing TR decreases X_P and moves the ETM closer to Naburn Weir. Compared with the influence of freshwater inflow the tidal effect in this system is secondary and will be ignored. Thus a relationship for X_P can be proposed (see Uncles et al., in press):

$X_P = 17(Q_{31})^{0.31}$ km

References

Uncles, R.J., Bale, A.J., Brinsley, M.D., Frickers, P.E., Harris, C., Lewis, R.E., Pope, N.D., Staff, F.J., Stephens, J.A., Turley, C.M., Widdows, J. 2003. Intertidal mudflat properties, currents and sediment erosion in the partially mixed Tamar estuary, UK. Ocean Dynamics, 53, 239-251.

Uncles, R.J., Stephens, J.A., Harris, C. In press. Runoff and tidal influences on the estuarine turbidity maximum of the highly turbid Humber Estuary, UK. Marine Geology.

2.4.2 EP11 - Algorithm for the effects of suspended sediment on turbulence within an estuarine turbidity maximum (UOP-Dyer)

Aim Analysis and interpretation of existing field data for turbulence and sediment properties within an estuarine turbidity maximum.

Background
There is a poor understanding of the formation and entrainment of near bed high concentration layers, because of the interacting effects of the density on the turbulence, the shear stresses and the velocity field. The results of a field study undertaken during the EC COSINUS project, have been analysed to help understand the effects of high concentration sediment suspensions upon the nature of near-bed turbulence. In this study, measurements of current velocities, associated turbulence and flow characteristics were measured within and above a high concentration near bed layer in the turbidity maximum of the Tamar Estuary. Two pairs of electro-magnetic flowmeters were orthogonally mounted on a bed frame at two separate heights to capture the mean and fluctuating velocities in the along-stream, lateral and vertical directions. Simultaneously, profiles of suspended sediment concentration, salinity, and temperature were obtained. Detailed examination of results obtained over several tidal cycles led to the selection of two spring ebb tides when criteria relating to the orientation of the EM flowmeters were satisfactory. Because of the narrowness of the lutocline, with gradients in excess of 15 kgm^{-4}, it is inherently difficult to characterise the gradient Richardsons numbers in anything other than general terms. This restricts comparison of the results with theory.

Turbulent shear stresses are difficult to determine when wave motions are present, and shear stresses were calculated both from the turbulent kinetic energy (TKE) and as the Reynolds stress. Intermittent internal waves were important features of the turbulence, especially at higher Richardson numbers (> 0.15) and above the lutocline. At lower Richardson numbers internal waves were less significant. Attempts to categorise the internal waves showed them to be a complicated mixture of progressive and standing waves, with the proportions and amplitudes varying at different times. At lower Richardson numbers the ratio of measured vertical to horizontal turbulent intensities were similar to clear water values (0.4-0.7), increasing away from the bed. The TKE and the shear stress derived from it were greater at the lower height. At higher Richardson numbers the TKE was greater at the upper height, and the ratio of vertical to horizontal turbulence intensities exceeded 1.0, and reached 1.6 when internal waves were present. Additionally, internal waves increase the total magnitude of the fluctuations, without necessarily affecting the turbulent stresses, depending on the phase relationships created by the standing and progressive nature of the waves. As the internal wave effects are greatest above the lutocline, this leads to the fluctuations being smaller within the lower layer, and TKE shear stresses larger at the upper level.

Results
Comparison between shear stresses calculated from the turbulent kinetic energy, and via the Reynolds stresses showed 'inactive turbulence' occurring at stresses less than about 0.2 Nm^{-2} both within and above the high concentration layer. Consequently, there are disorganised motions present at low stresses that may exchange mass, but not momentum. Thus stresses below this magnitude are unlikely to create break-up of flocs, but are more likely to promote aggregation, as well as allowing settling.

During the periods of inactive turbulence, calculated turbulent Reynolds fluxes of suspended sediment showed that negative suspended sediment fluxes often occurred, adding a downward flux similar in magnitude to that due to advective settling. This indicates that the turbulence could significantly enhance settling of the sediment. Additionally, downward fluxes intermittently occurred at higher stresses within the high concentration layer. This suggests that within the layer a modest amount of turbulence may increase the settling of sediment. This settling 'threshold' needs to be incorporated in mathematical models. Additionally, the presence of internal waves appear to increase the variability of the Reynolds fluxes of suspended sediment, also allowing downwards sediment fluxes at other times, especially beneath the lutocline.

Quadrant analysis of the direction and sign of turbulent velocity fluctuations showed that above the lutocline sweeps, strong downwards vectors, and ejections, weaker upward vectors, each contributed about 33% of the overall stress, the same as for clear water. The inward and outward interactions together occupied 30 % of the time. However, beneath the lutocline the density layering appeared to rotate the ellipse enclosing the limits of the fluctuations, and reduce the contribution of all four quadrants to 24-28%, thus relatively increasing the duration of the interaction events. These changes must occur by a reduction in the magnitude of both the horizontal and vertical fluctuations, but a relative increase in the vertical contributions at the expense of the horizontal.

Examination of the quadrant relationships of the velocity and concentration fluctuations show that differences in the sign and magnitudes of the Reynolds fluxes arise because of the details of the way in which the profile of concentration interacts with the velocity fluctuations. Downwards motions must be correlated with low concentrations and upward motions with high concentrations. Above the lutocline where the profile variation of concentration is small, the downward motions cannot create a large downward flux of sediment, whereas the upward motions create a large upward flux. Similarly, below the lutocline upward motions produce relatively large upward fluxes, because of the high concentration, and downward motions create lesser downward fluxes. As a consequence of the actions occurring simultaneously at both levels, a sweep would tend to enhance the lutocline, whereas an ejection would lessen the intensity of the lutocline. During the increased duration of the interaction phases, downward fluxes would occur by settling. The overall effect of the turbulent bursting cycle may then depend crucially on the way in which the velocity fluctuations in the burst are modified by the presence of the lutocline, as well on the period when there is inactive turbulence.

Physical explanation and challenges

A physical explanation for the unexpected enhancement of the vertical fluctuations at the expense of the horizontal, in terms of the structure of the water motions, seems to lie in the observed complicated interaction of standing and progressive waves. Incorporating these internal waves into mathematical models will require careful specification of their properties.

Because of the importance of internal waves to the specification of the fluxes, further more detailed measurement is required in order to parameterise adequately turbulence in transport models.

Algorithm

The upper limit for gravitational settling may be extended to stresses of 0.2 Nm^{-2}. Within this range, the flux of settling sediment could be doubled.

Reference

Dyer, K.R.; Christie, M.C., and Manning, A.J., 2004. The effects of suspended sediment on turbulence within an estuarine turbidity maximum. *Estuarine, Coastal and Shelf Science*, **59**, 237-248.

2.4.3 EP12 - Algorithm for the Dimensional Relationships of Estuaries (UOP-Dyer)

Aim To provide improved relationships between estuary dimensions and physical driving processes

Background
The O'Brien relationship states that there is an empirical power law relationship between the cross sectional area of the estuary mouth, and the tidal prism. Also it is frequently assumed for morphological modelling that the O'Brien relationship holds for cross sections and tidal prisms of subsections of an estuary. The relationship has been investigated by a large number of authors for estuaries from around the world in order to try to establish empirical rules by which prediction can be carried out. It is apparent that no one set of constants is universal, and that tidal velocities, characterised by the tidal prism, have to be modified by inclusion of factors relating to the type of the estuary, the geology, availability of sediment, and littoral processes. These factors have recently been examined comprehensively by Townend (2005) for 66 British estuaries. He concluded that geological history and availability of sediment are important, and an improvement can be made by allowing for estuary length, and for frictional effects. However, river flow is important in many estuaries. Additionally, the cross sectional area at the mouth can be defined in a variety of ways, normally as the area at high spring tide. In the study reported here, river flow is considered, as well as the fact that the maximum tidal velocity normally occurs at about mean tide level, rather than at high water. For the river flow component the maximum spate discharges have been considered, as they are likely to be important in determining the morphological response of those estuaries where river flow exerts an influence.

Method
The dimensions of 96 estuaries from England and Wales detailed in the FUTURECOAST datafiles (Burgess et al, 2002) have been examined, corrected where necessary, and extended and updated. This is an extension of work done originally in EMPHASYS – ERP1 (EMPHASYS Consortium, 2000).

However, the quality of some of the data remains inherently unsatisfactory. The normal O'Brien analysis shows that there are no universal coefficients that can be generally used. Differences between estuaries appear to relate to the sediment quantities that have been available to fill the estuary and provide a sediment balance. This means that there can be delays between the formation of the estuary and the achievement of a sedimentary balance, and these can be of the order of thousands of years. Also the presence of rock, or a harder substrate, limits the amount of adjustment possible in the mouth cross section to increases in current velocity required by increases in the tidal prism. Additionally, the magnitude of sedimentary processes active around the mouth determine whether spits can develop, and their presence can hinder the ready availability of finer sediment to fill the inner estuary. Man made training walls and jetties have a similar effect. Also, reclamation of intertidal areas change the currents through the mouth and require a change in cross sectional area to produce a balance. In some cases tendency for change in cross sectional areas may have been altered by dredging of the navigation channel.

River Discharge

The river discharges into each estuary from the river catchment have been taken from the Hydrological Data UK, Hydrometric Register and Statistics 1991-95, as detailed in the FUTURECOAST database. During the tidal cycle, the river discharge increment during the flooding tide should appear as part of the calculated tidal prism volume. The discharge increment during the ebb tide, however, will enhance the tidal flow. Consequently, the tidal prism is increased by the river discharge volume totalled over six and a quarter hours.

Results for a comparison between the high water tidal prism and the tidal prism plus the ebb tide increment of river flow is shown in Figure 1. It is apparent that for a majority of estuaries the inclusion of river flow would not affect the O'Brien relationship significantly. However, for some estuaries the deviation is large. The Tyne and the Parrett, for instance, are narrow estuaries with comparatively large catchments that have been modified and trained for industrial purposes and to prevent flooding. The Dovey and the Conwy, in comparison, drain mountainous areas with high rainfall, and their valleys are in resistant rocks. Of particular note are the small estuaries, such as the Teifi, the Ogmore and the Tweed, where the river flow increment during spates can be much larger than the tidal prism.

Thus, deviation of the points from the line of equality is related to the flow ratio, the ratio of the river flow to the tidal prism. Points unaffected by river flow represent well mixed estuaries, and those departing from the line are increasingly stratified at maximum river flow. At those times the river flow and river borne sediments are likely to dominate the estuarine morphodynamics.

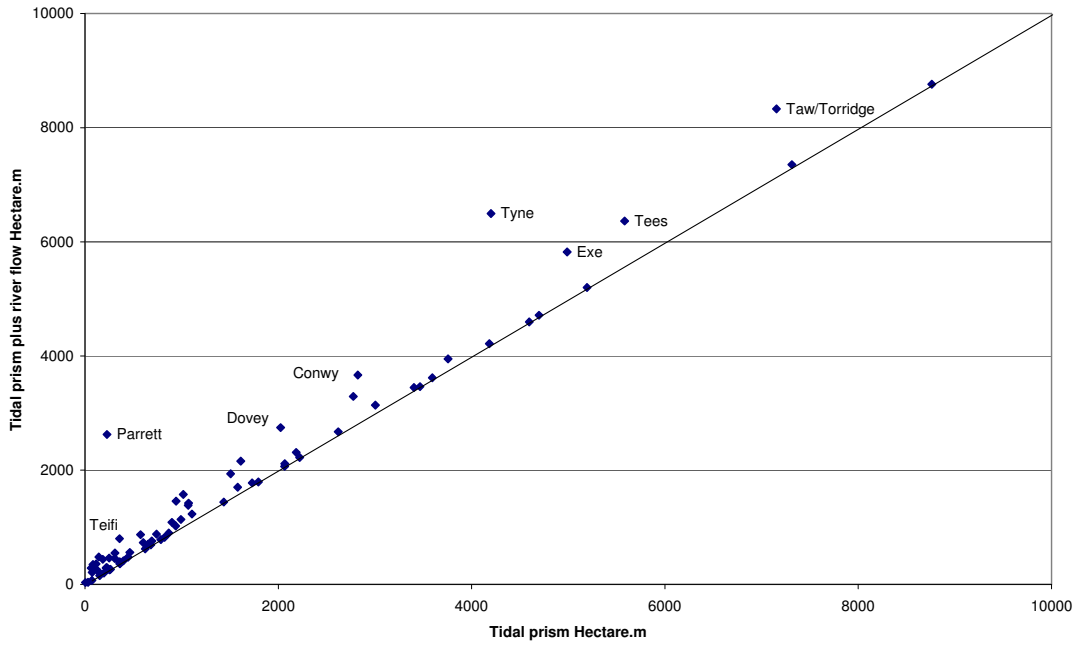

Figure 1 The high water tidal prism versus the tidal prism including the ebb tide increment of river flow. The line shows equality

Tidal Phase

The maximum velocity through the mouth of an estuary, which should be the most morphodynamically important current, does not occur at high water, but at around mean

tide level. The effect of the phase of the current is shown in Figure 2 by comparison of the high water cross sectional area with that at the mean tide level.

For all estuaries there is a reasonable linear trend that continues for the large estuaries such as the Severn and the Wash, which are outside the axes plotted for this figure. This would have the effect of reducing the constants in the O'Brien relationship. However, the cross sectional area of the shallow high tidal range estuaries, such as the Solway and the Dee, is affected more than estuaries, such as the Thames, Plymouth and the Mersey, that have mouths with jetties, embankments or training walls. The effect will be large also for small estuaries where the tidal range is comparable with the water depth.

The scatter in the points, in terms of the cross sectional area, is likely to be related to the intertidal area ratio, the ratio of the intertidal area to the total high water surface area. This, however, will be modified by littoral processes occurring at the mouth, and the formation of enclosing spits.

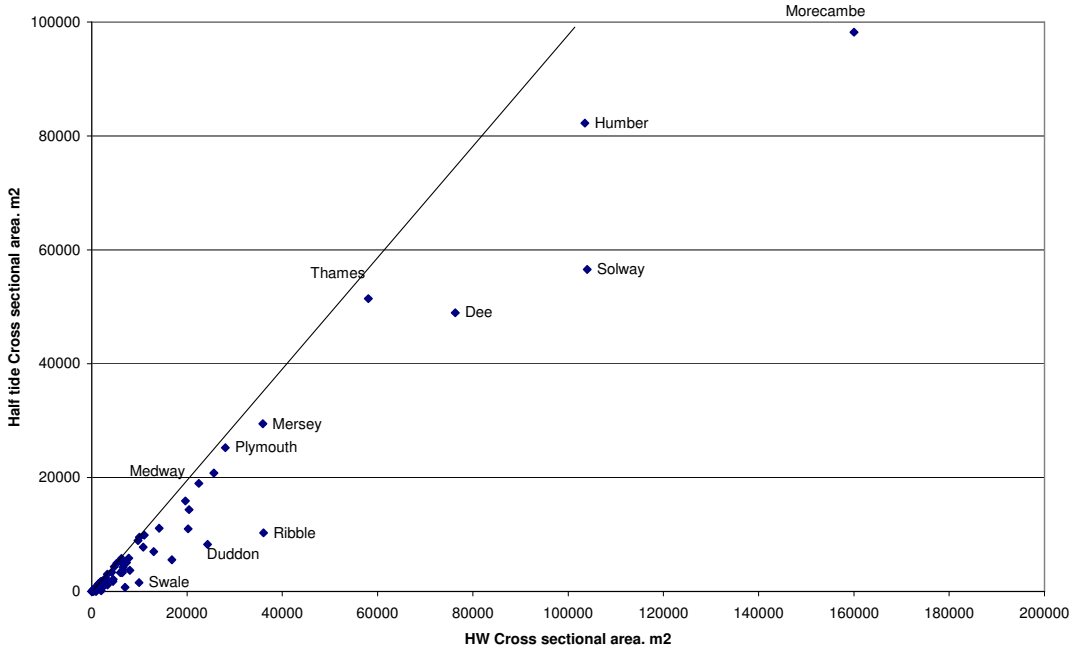

Figure 2 High water cross sectional area versus half tide cross sectional area. The line shows equality

Use of algorithms

A comparison of plots of the O'Brien relationship, using the traditional high water cross sectional area and the tidal prism, with the values discussed above of half tide cross sectional area and the river flow enhanced tidal prism does not provide any significant improvement over previous approaches in reducing the scatter. It is apparent that there are too many factors that need to included and parameterised to provide a realistic empirical formula. Definition and prioritisation of the factors becomes subjective and they are difficult to quantify. Consequently, dimensional relationships have to be determined on an individual estuary basis, and applying the results obtained for the whole estuary to other cross sections within an estuary may not be valid. Success is likely to be greatest in morphodynamically active, well mixed estuaries where the mouths are relatively well defined.

Reference

Burgess, K.A., Balson, P., Dyer, K.R., Orford, J., Townend, I.H., 2002. Future-Coast – the integration of knowledge to assess future coastal evolution at a national scale. In: 28th International Conference on Coastal Engineering. ASCE, New York, 3, pp 3221–3233.

EMPHASYS Consortium, 2000. Modelling Estuary Morphology and Processes. Final Report. Research by the EMPHASYS Consortium for MAFF Project FD 1401. Report TR 111. HR Wallingford, UK. December 2000.

Townend, I, 2005. An examination of empirical stability relationships for UK estuaries. Journal of Coastal Research, 21, 1042-1053.

2.5 Representation of near bed stresses

2.5.1 EP 13 - Algorithm for wave-current bed shear stresses (HRW – Soulsby)

Algorithm Version number 2-1

Aim To calculate bed shear-stresses due to combined waves and currents acting on smooth and rough beds.

Scientific background
Calculations and numerical modelling of the erosion, transport and deposition of sediments in estuaries and coastal areas rely heavily on expressions that contain the bed shear-stress, representing the friction exerted by the flowing water on the bed. In general the bed shear-stress is generated by the combined effects of waves and currents, whose turbulent boundary layers interact non-linearly. Many analytical and numerical models of bed shear-stresses due to wave-current interaction on *rough* beds already exist, because of their importance for sediment transport calculations. However, they generally require computationally-intensive solution, so that they are unsuitable for the repeated calculations needed in morphodynamic models of coastal and estuarine processes. In addition, much less attention has been given to the case of *smooth* beds such as freshly deposited mud in estuaries. The new method developed in EstProc provides an explicit set of formulae to predict the mean, maximum and root-mean-square bed shear-stress for any combination of waves for any flow regime (full derivation presented by Soulsby and Clarke, 2004). It includes different but compatible methods for laminar, smooth-turbulent and rough-turbulent flows, and automatically determines which case to use. It is based on an analytical solution of the equation of motion with a turbulence closure given by a time-independent, vertically varying eddy viscosity.

Improvement in understanding
The new method improves on existing methods because:

- it can be expressed with explicit algebraic formulae, simplifying and speeding up calculations
- it is based on physics, so improves on existing purely empirical methods
- it deals with all of laminar, smooth-turbulent and rough-turbulent regimes, which most other methods do not
- it has been tested against published laboratory data, and gives good agreement.

Implementation
The algorithm is written in a step-by-step "recipe" style, which can easily be coded for computer application. A corresponding FORTRAN code has also been written and tested. It comprises a subroutine that calls several other subroutines and functions, plus a calling (main) program to read inputs and write outputs to file. The main program can be used in stand-alone mode. The subroutine can be incorporated into larger FORTRAN models.

Algorithm

1. Inputs

Water depth (m)	h	
Water density (kgm^{-3})	ρ	
Kinematic viscosity ($m^2\ s^{-1}$)	ν	
Median grain diameter of bed (m)	d_{50}	(= 0 for smooth bed)
Wave orbital velocity amplitude (ms^{-1})	U_w	
Wave period (s)	T	
Depth-averaged current speed (ms^{-1})	$\overline{U}$	
Angle between wave and current directions (degrees)	ϕ_d	($0° \le \phi_d \le 360°$)
Acceleration due to gravity (ms^{-2})	g	($9.81 ms^{-2}$)

2. Outputs

Current-alone bed shear-stress (Nm^{-2})	τ_c
Wave-alone bed shear-stress amplitude (Nm^{-2})	τ_w
Mean wave-plus-current bed shear-stress (Nm^{-2})	τ_m
Maximum wave-plus-current bed shear-stress (Nm^{-2})	τ_{max}
Root-mean-square wave-plus-current bed shear-stress (Nm^{-2})	τ_{rms}

3. Calculate basic parameters

Convert ϕ_d to radians: $\phi = \phi_d\ \pi/180$

Convert d_{50} to bed roughness length (rough flow): $z_o = d_{50}/12$

Calculate current Reynolds Number

$$Re_c = \frac{\overline{U}h}{\nu} \quad (1)$$

Calculate wave semi-orbital excursion

$$A = \frac{U_w T}{2\pi} \quad (2)$$

Calculate wave Reynolds Number

$$Re_w = \frac{U_w A}{\nu} \quad (3)$$

Calculate drag coefficient for current for smooth turbulent flow

$$C_{Ds} = 0.0001615 \exp\left[6(Re_c)^{-0.08}\right] \quad (4)$$

Calculate wave friction factor for smooth turbulent flow

$$f_{ws} = 0.0521\, Re_w^{-0.187} \quad (5)$$

Calculate drag coefficient for current for rough turbulent flow

$$C_{Dr} = \left[\frac{0.40}{\ln(h/z_o) - 1}\right]^2 \quad (6)$$

Calculate wave friction factor for rough turbulent flow

$$f_{wr} = 1.39\left(\frac{A}{z_o}\right)^{-0.52} \quad (7)$$

4. Determine flow regime

4.1 If $\overline{U} = 0$ and $U_w = 0$, then no flow

$\tau_m = \tau_{max} = 0$ (8)

4.2 If $\overline{U} > 0$ and $U_w = 0$, then current-only flow

If $Re_c \le 2000$, then laminar flow

$$\tau_m = \tau_{max} = \frac{3\rho\nu\overline{U}}{h} \quad (9)$$

If $Re_c > 2000$, then turbulent flow

Calculate $\tau_{mr} = \rho C_{Dr} \overline{U}^2$ (rough) (10a)

and $\tau_{ms} = \rho C_{Ds} \overline{U}^2$ (smooth) (10b)

then $\tau_m = \tau_{max} = \max(\tau_{mr}, \tau_{ms})$ (11)

4.3 If $\overline{U} = 0$ and $U_w > 0$, then wave-only flow

If $Re_w \le 1.5 \times 10^5$, then laminar flow

$\tau_m = 0, \tau_{max} = \rho Re_w^{-0.5} U_w^2$ (12)

If $Re_w > 1.5 \times 10^5$, then turbulent flow

Calculate $\tau_{wr} = \frac{1}{2}\rho f_{wr} U_w^2$ (f_{wr} from Eq. (7)) (13)

and $\tau_{ws} = \frac{1}{2}\rho f_{ws} U_w^2$ (f_{ws} from Eq. (5)) (14)

then $\tau_m = 0, \tau_{max} = \max(\tau_{wr}, \tau_{ws})$ (15)

4.4 If $\overline{U} > 0$ and $U_w > 0$, then combined wave and current flow

Calculate critical current Reynolds number

$Re_{c,cr} = 2000 + (5.92 \times 10^5 \times Re_w)^{0.35}$ (16)

$Re_{w,cr} = 1.5 \times 10^5$

If $Re_c \le Re_{c,cr}$ *and* $Re_w \le Re_{w,cr}$, then laminar flow

τ_m given by Eq. (A9)

$\tau_w = \rho Re_w^{-0.5} U_w^2$ (17)

$\tau_{max} = \left[(\tau_m + \tau_w|\cos\phi|)^2 + (\tau_w|\sin\phi|)^2\right]^{1/2}$ (18)

If $Re_c > Re_{c,cr}$ *or* $Re_w > Re_{w,cr}$, then turbulent flow

Calculate $\tau_{m,r}$ and $\tau_{max,r}$ for rough flows using method given in Step 5

Calculate $\tau_{m,s}$ and $\tau_{max,s}$ for smooth flows using method given in Step 6

If $\tau_{max,r} > \tau_{max,s}$, then flow is rough turbulent

$\tau_m = \tau_{m,r}, \tau_{max} = \tau_{max,r}$ (19a)

If $\tau_{max,r} \le \tau_{max,s}$, then flow is smooth turbulent

$\tau_m = \tau_{m,s}, \tau_{max} = \tau_{max,s}$ (19b)

The values of τ_c and τ_w must be calculated for the flow regime determined in this sub-section for combined waves and currents. Thus τ_c and τ_w are given respectively by:

Eqs. (9) and (12) for laminar flow
Eqs. (10a) and (13) for rough turbulent flow
Eqs. (10b) and (14) for smooth turbulent flow.

5. Rough-turbulent wave-plus-current shear-stresses

Set $a_r = 0.24$

Calculate $T_1 = \dfrac{\delta}{z_o} = \max\{12, a_r \left(\dfrac{f_{wr}}{2}\right)^{1/2} \left(\dfrac{A}{z_o}\right)\}$ (20)

with f_{wr} from Eq. (A7)

$$T_2 = \frac{h}{\delta} = \frac{h}{T_1 z_o} \tag{21}$$

$$T_3 = \frac{u_{*e}}{\overline{U}} = \left[C_{Dr}^2 + \left(\frac{f_{wr}}{2}\right)^2 \left(\frac{U_w}{\overline{U}}\right)^4 \right]^{1/4} \tag{22}$$

with C_{Dr} from Eq. (A6)

$$A_1 = \frac{T_3 [\ln(T_2) - 1]}{2\ln(T_1)} \tag{23}$$

$$A_2 = \frac{0.40\, T_3}{\ln(T_1)} \tag{24}$$

$$C_{Dm} = \left[\left(A_1^2 + A_2\right)^{1/2} - A_1 \right]^2 \tag{25}$$

$$C_{D\max} = \left[\left(C_{Dm} + T_3 \cdot \frac{U_w}{\overline{U}} \cdot \left(\frac{f_{wr}}{2}\right)^{1/2} \cdot |\cos\phi| \right)^2 + \left(T_3 \frac{U_w}{\overline{U}} \left(\frac{f_{wr}}{2}\right)^{1/2} \cdot |\sin\phi| \right)^2 \right]^{1/2} \tag{26}$$

$$\tau_m = \rho\, C_{Dm}\, \overline{U}^2 \tag{27}$$

$$\tau_{max} = \rho\, C_{D\max}\, \overline{U}^2 \tag{28}$$

6. Smooth turbulent wave-plus-current shear-stress

Set $a_s = 0.24$

Calculate

$$T_1 = 9\, a_s\, Re_w \left(\frac{f_{ws}}{2}\right)^{1/2} \left[C_{Ds}^2 \left(\frac{\overline{U}}{U_w}\right)^4 + \left(\frac{f_{ws}}{2}\right)^2 \right]^{1/4} \tag{29}$$

with f_{ws} from Eq. (A5), C_{Ds} from Eq. (A4)

$$T_2 = \left(\frac{Re_c}{Re_w}\right) \cdot \left(\frac{U_w}{\overline{U}}\right) \cdot \frac{1}{a_s} \cdot \left(\frac{2}{f_{ws}}\right)^{1/2} \tag{30}$$

$$T_3 = \left[C_{Ds}^2 + \left(\frac{f_{ws}}{2}\right)^2 \cdot \left(\frac{U_w}{\overline{U}}\right)^4 \right]^{1/4} \tag{31}$$

Calculate A_1 from Eq. (23), A_2 from Eq. (24), C_{Dm} from Eq. (25), C_{Dmax} from Eq. (26) except replace f_{wr} with f_{ws}, τ_m from Eq. (27), τ_{max} from Eq. (25)

7. RMS shear-stress for waves plus current

Calculate τ_m using the methods given above appropriate to laminar, smooth-turbulent or rough-turbulent flow regime. The flow regime is determined by the criteria given in Section 4.4.

Calculate τ_w from Eq. (A17) if flow is laminar, or Eqs. (5) and (14) if flow is smooth turbulent, or Eqs. (7) and (13) if flow is rough turbulent.

Calculate root-mean-square shear-stress

$$\tau_{rms} = \left(\tau_m^2 + \tfrac{1}{2}\tau_w^2\right)^{1/2} \qquad (32)$$

8. Worked examples

The following inputs and outputs are provided so that users can check they get the same answers. The full step-by-step working is not given, since it would be rather lengthy.

8.1 Laminar flow

Inputs: $h = 0.1m$, $\rho = 1000kgm^{-3}$, $\nu = 1.0 \times 10^{-6}m^2s^{-1}$, $d_{50} = 0$ (smooth bed), $U_w = 0.2ms^{-1}$, $T = 10s$, $\overline{U} = 0.06ms^{-1}$, $\phi_d = 0^0$

Outputs: $(\tau_c, \tau_w, \tau_m, \tau_{max}, \tau_{rms}) = (0.0018, 0.1585, 0.0018, 0.1603, 0.1121)\ Nm^{-2}$

8.2 Smooth turbulent flow

Inputs: $h = 0.4m$, $\rho = 1000kgm^{-3}$, $\nu = 1.0 \times 10^{-6}m^2s^{-1}$, $d_{50} = 0$ (smooth bed), $U_w = 0.4ms^{-1}$, $T = 2s$, $\overline{U} = 0.3ms^{-1}$, $\phi_d = 75^0$

Outputs: $(\tau_c, \tau_w, \tau_m, \tau_{max}, \tau_{rms}) = (0.1530, 0.5492, 0.2194, 0.6518, 0.4460)\ Nm^{-2}$

8.3 Rough turbulent flow

Inputs: $h = 5m$, $\rho = 1000kgm^{-3}$, $\nu = 1.0 \times 10^{-6}m^2s^{-1}$, $d_{50} = 0.001m$, $U_w = 0.7ms^{-1}$, $T = 8s$, $\overline{U} = 0.5ms^{-1}$, $\phi_d = 90^0$

Outputs: $(\tau_c, \tau_w, \tau_m, \tau_{max}, \tau_{rms}) = (0.3998, 2.7353, 0.7292, 2.8448, 2.0670)\ Nm^{-2}$

9. Limits of applicability

The method can be applied to both laboratory and field conditions. Any combination of waves and currents at any angle, and from pure current through to pure wave, can be used. However, the method gives poor results for cases in the transitional regime, when the flow is laminar at some phases of the wave cycle and turbulent at others. The bed is assumed to be horizontal (say slopes of 0 to 1:20), and can be smooth (e.g. laboratory

steel-bedded flume, or freshly deposited mud in field conditions) or covered in (flat) sand or gravel. It can also be used for rippled sand provided that a suitable ripple scale is used instead of d_{50}. For ripples of height Δ_r and wavelength λ_r, an equivalent d_{50} grainsize of approximately $d_{50} = 12\Delta_r^2/\lambda_r$ could be used. For rippled beds the resulting shear-stresses are *total* stresses (including form drag of the ripples). For flat beds the shear stresses represent the *skin-friction*. The waves are assumed to be monochromatic, and given by a sinusoidally varying bottom orbital velocity. The velocity asymmetry under crest and troughs of steep waves is not taken into account. Waves are assumed to be non-breaking, since breaking-generated turbulence is not included. A spectrum of irregular waves must be approximated by a monochromatic wave (see Soulsby, 1997, p79). There are no formal limits to the input parameters, but the following are suggested as approximate limits of applicability.

Depth $0.1 \le h \le 100$m

Density $1000 \le \rho \le 1100$ kg m^3

Kinematic viscosity $1.0 \times 10^6 \le \nu \le 2.0 \times 10^{-6}$ m^{2}s^{-1}

Grainsize $0 \le d_{50} \le 1$m, with $d_{50} < 0.1h$

Wave orbital velocity $0 \le U_w \le 5$ms^{-1}

Wave period $1 \le T \le 30$s

Current speed $0 \le \bar{U} \le 5$ms^{-1}

Angle between waves and currents $0 \le \phi_d \le 360°$. (NB since waves are treated as sinusoidal, there is no distinction between waves travelling "with" and "against" the current.)

Validation

Tests of the new method against data and existing methods are presented by Soulsby and Clarke (2004). The new rough-bed method agrees well with the earlier empirical "DATA2" method that was itself calibrated against extensive lab and field data. Tests of the new method against the same smooth-bed data (131 values) gave predictions of *mean* bed shear-stress that lay within factors of 1.1, 1.2, 1.5 and 2 for 26%, 52%, 82% and 90% of the observations respectively. No other existing rough-bed method gives better all-round agreement. The *maximum* bed shear-stresses were not able to be measured in these data-sets. The new smooth-bed method was tested against two sets of laboratory data. It gave significantly better agreement with the data than earlier methods. For the most appropriate set of smooth-bed data (80 values), the new method gave predictions of *mean* bed shear-stress that lay within factors of 1.1, 1.2, 1.5 and 2 for 30%, 41%, 68% and 75% of the observations respectively. It gave predictions of the *maximum* bed shear-stresses that lay within the above factors for 48%, 65%, 80% and 94% of the observations respectively. No other existing smooth-bed method gives better all-round agreement.

Gaps in knowledge

There appears to be a lack of data for field-scale (or full-scale laboratory) measurements of bed shear-stresses under combined waves and currents on smooth beds. The effects

of a mobile layer of sediment (mud or sand) on bed shear-stresses is poorly understood. Models that include wave-breaking turbulence are needed.

References

Soulsby, R. L. (1997). "Dynamics of Marine Sands – a manual for practical applications". Thomas Telford Publications, London ISBN: 07277 2584X. 249 pp.

Soulsby, R. L. and Clarke, S. (2004). Bed shear-stresses under combined waves and currents on smooth and rough beds. Report TR137, HR Wallingford Ltd (Rev 1.0).

2.5.2 EP14 - Algorithm for bed roughness with Moveable Bed Model (ABP – Harris)

Aim To produce a prediction method for wave-generated ripple height and wavelength which can be implemented in ripple bed roughness predictors.

Method
In the present approach the method of Vongvisessomjai *et al.* (1987) has been adapted. This is an approach described in Harris (1997) to enable the prediction of field generated ripples, that is ripple geometry under irregular waves. The proposed model is based on Eqs. (1) and (2):

$$\Delta(t) = \Delta_{\max n}\left\{1 - \exp\left[-B_n^*\left(\frac{t}{T_{zn}}\right)\right]\right\} \quad (1)$$

and

$$\lambda(t) = \lambda_{\max n}\left\{1 - \exp\left[-B_n^*\left(\frac{t}{T_{zn}}\right)\right]\right\} \quad (2)$$

where B_n^* is defined as:

$$B_n^* = 1.77 \times 10^{-6} a_{*n}^{1.68} \psi_n^{-0.394}$$

$$B_n^* = 1.82 \times 10^{-4} a_{*n}^{0.366} \psi_n^{0.432}$$

and a_{*n} is the relative bed smoothness and is given by:

$$a_{*n} = \frac{a_n}{d_{50}}$$

a_n is the near-bed orbital amplitude such that $a_n = u_{\infty n}/\omega_n$; u_∞ is the near-bed velocity amplitude; ω_n is the angular frequency and d_{50} the median grain diameter.

ψ_n is the mobility number and is defined as:

$$\psi_n = \frac{(a_n\omega_n)^2}{(s-1)gd_{50}}$$

where s is the specific gravity of the sediment, given by $s = \rho_s/\rho$, where ρ_s is the density of the sediment and ρ is the fluid density.

The model allows T_z to vary, so for a given surface wave height time-series, n zero-upcrossing periods can be calculated along with the corresponding wave heights, H_n. The quantity n denotes the number of zero-upcrossing periods in the given wave height record. Knowing T_{zn} and H_n allows the maximum near-bed orbital amplitude, a_n, and

maximum near-bed orbital velocity, $u_{\infty n}$, to be calculated. From this, it is possible to calculate n values for the maximum possible ripple geometry, $\Delta_{max\,n}$ and $\lambda_{max\,n}$. Using these values and Eqs. (1) and (2) enables a time-series for the ripple geometry to be generated. For each nth value, the value of t within the exponential term is reset to zero, whilst leaving the actual time-series to run continuously. A ripple will continue to grow in height until the value of the present $\Delta_{max\,n}$ is reached. If for the n+1 value, the value of $\Delta_{max(n+1)}$ is smaller than $\Delta_{max\,n}$ the ripple height will start to decay. A similar process operates for the ripple length.

The value of $\Delta_{max\,n}$ was calculated using four existing predictors: Nielsen, Wiberg and Harris, Grant and Madsen, Mogridge et al.

Validation

For more information on application and testing of this algorithm see the report ABPmer (2004).

References

ABPmer (2004). Modelling Moveable Seabed Roughness Under Random Waves, Report R.1092.

Harris, J.M. (1997*). Modelling Random Wave Boundary Layers*. Dept. of Civil Engng., Ph.D. thesis, University of Liverpool, 356pp.

Vongvisessomjai, S., Munasinghe, L.C.J. and Gunaratna, P.P. (1987). Transient ripple formation and sediment transport. In: *Coastal Engng.*, Proc. 20th Int. Conf. Coastal Engng., (ed.) Edge, B.L., Taipei, Taiwan, 9-14 Nov., 1986, Vol. 2, Chap. 120, ASCE, New York, pp. 1638 -1652.

2.5.3 EP15 - Algorithm for representation of near bed stresses in an annular flume (PML – Widdows)

Aim To describe the relationship between current velocity (U_{10}) and bed shear stress in PML's annular flumes for intertidal sediments with biota. To compare with measurements in the field (shallow water estuarine mudflats) over tidal cycles (spring tides) during calm weather conditions without wind / waves.

Scientific Background
There is a variety of *in situ* devices for measuring sediment erodibility. Several of these have been widely used to quantify sediment erosion in various field campaigns investigating the functional role of key intertidal biota (e.g. PML's annular flumes, PML's mini-flumes, SOC's annular flumes, Cohesive Strength Meter (CSM), EROMES). Some of the erosion devices with smaller 'footprints' have a vertical jet or turbulent flow and are difficult to calibrate in terms of the shear stress applied to the bed. The size of PML's annular flume and mini-flume are suitable for measurement of vertical profiles of current and turbulence. The use of Acoustic Doppler Velocimeters (ADV) has enabled us to establish the relationship between bed shear stress, determined by the Turbulent Kinetic Energy (TKE) method, and the current velocity at 10 cm above the bed, in PML's annular flume, mini-flume and in the field (i.e. same smooth estuarine mudflats under calm weather conditions) (Figure 1).

Improvement in understanding
Numerical models of estuarine sediment dynamics and morphology need to incorporate biological as well as physical processes in order to represent the natural estuarine environment. Establishing relationships between current velocity, bed shear stress and drag coefficients for different types of bed and bed roughness, including those influenced by biota, are necessary to improve parameterisation of numerical models.

Implementation
The equation below is routinely applied to estimate bed shear stress from measurements of near bed current velocities (U_{10}). It is applicable to extensive areas in many estuaries where mudflats are composed of smooth fine sediments.

Algorithm

Bed shear stress (Pa) = $0.4702U_{10}^3 + 1.152U_{10}^2 + 0.1553U_{10}$ $\quad r^2 = 0.99$

Inputs:
U_{10} = Current velocity (m s^{-1}) at 10 cm above the bed. Suitable for a range of current velocities from 0.02 to 0.4 m s^{-1}. Note that in PML's annular flumes the U_{10} is very similar to the depth averaged current velocity.

Output:
τ_0 = Bed shear stress (Pa)

This relationship was established in the flume and field using an ADV for measuring near-bed currents and bed shear stress (TKE method). It is plotted in Figure 1.

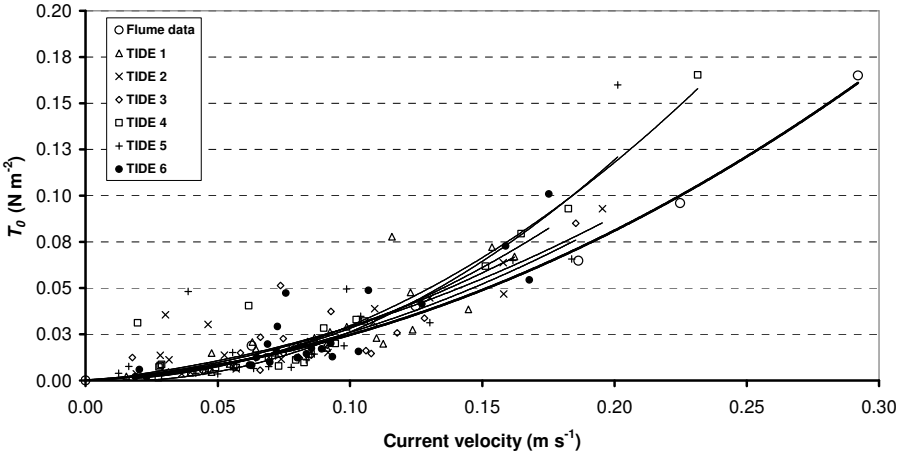

Figure 1 Comparison of flume and field derived relationships for bed shear stress (τ_0) against current velocity for Blaxton intertidal sediment (smooth mudflat). Field data collected every 15 minutes over 6 spring tides

Limits of applicability

The algorithm only applies to recently deposited fine sediment and smooth mudflats of cohesive fine sediment with minimum disturbance due to biota. The relationship applies to current velocities between 0.02 and 0.40 m s^{-1}.

Bed shear stress increases relative to current velocity with increasing bed roughness induced by grain size, bed ripples and biota.

Validation

The flume measurements of bed shear stress in relation to current velocity (U_{10}) for smooth cohesive fine sediment fall within the range of data recorded with the field ADV over a tidal cycle under calm weather conditions (field measurements in Blackwater, Crouch (Essex), and Tavy (SW England).

Gaps in Knowledge

There is a need to establish algorithms for a wider range of sediment types and biotic influences and to calculate drag coefficients from the relationships.

References

Pope, N.D., Widdows, J. and Brinsley, M.D. Estimation of bed shear stress using turbulent kinetic energy (TKE) approach:- Comparison of annular flume and field data (submitted).

2.6 Transport of mixed sediments

2.6.1 EP16 - Algorithm for modelling sediment mixing in estuaries (WLD – Winterwerp)

Aim To calculate the sedimentation and flow-induced erosion rates of sand-mud mixtures

Scientific background See Sections 2.6.1.1 and 2.6.1.2 to this algorithm

Improvement in understanding This algorithm improves on existing formula because:

- it accounts for two different sediment fractions
- it accounts for the sedimentological nature of the bed
- its behaviour has been tested in a sensitivity analysis.

Implementation The new algorithm has been implemented in the operational DELFT3D software system.

This algorithm has to be implemented in existing solvers for the transport of sand and mud in suspension (two fractions). The model should contain a bed module consisting of a number of layers in which sand and mud can be stored upon deposition and released upon erosion.

Algorithm

Co-ordinate system
The vertical co-ordinate z within the bed is defined from the bed surface (i.e. $z = 0$) and positive downward.

Inputs
Note that superscripts are reserved for the sediment fractions sand (sa), clay (cl), silt (s), mud (m) and total (t); mud is the sum of the clay and silt fraction.

total bed concentration (kg/m^3)	c_b^t
sand concentration in the bed (kg/m^3)	c_b^{sa}
boundary condition c_b^{sa} at base of bed model (kg/m^3)	$c_{ini,b}^{sa}$ $\left(c_{ini,b}^{sa} \approx 1600 \text{ kg/m}^3\right)$
mud concentration in the bed (kg/m^3)	c_b^m
boundary condition c_b^m at base of bed model (kg/m^3)	$c_{ini,b}^m$ $\left(c_{ini,b}^m \approx 0\right)$
plasticity index bed sediment (-)	PI
equilibrium sand concentration in the water column (kg/m^3)	c_e^{sa} (from transport formula)
sand concentration in the water column (kg/m^3)	c^{sa}
mud concentration in the water column (kg/m^3)	c^m
water depth (m)	h
bed mixing length (m)	L_p (L_p = 0.01 – 0.1 m)

mud erosion parameter for non-cohesive bed (kg/m^2/s)	M_n^m
mud erosion parameter for cohesive bed (kg/m^2/s)	M_c^m
shear velocity (m/s)	u_*
settling velocity for sand (m/s)	W_s^{sa}
settling velocity for mud (m/s)	W_s^m
mixing coefficient (-)	α_0 ($\alpha_0 \cong 10^{-6}$)
time step (s)	Δt
form factor (-)	γ ($\gamma \cong 1$)
sediment density (kg/m^3)	ρ_s
flow-induced bed shear stress (Pa)	τ_b
critical bed shear stress for non-cohesive bed (Pa)	$\tau_{e,n}$
critical bed shear stress for cohesive bed (Pa)	$\tau_{e,c}$

Outputs

deposition rate sand (kg/m^2/s)	D^{sa}
erosion rate sand (kg/m^2/s)	E^{sa}
deposition rate mud (kg/m^2/s)	D^m
erosion rate mud (kg/m^2/s)	E^m

Algorithm

Assess sediment composition at bed surface

This algorithm models the mixing of mud within a sandy bed as a result of physical processes (bed form migration, waves, etc.) and of biological processes (bioturbation).

compute diffusion coefficient in bed

$$\varepsilon_b = \alpha_0 u_* h \exp\{-z/L_p\} \quad (1)$$

compute boundary conditions at bed surface, i.e. at the top (*top*) of bed model

$$c^m_{new,top} = c^m_{old,top} + \left(D^m - E^m\right)\Delta t \quad (2)$$
$$c^{sa}_{new,top} = c^{sa}_{old,top} + \left(D^{sa} - E^{sa}\right)\Delta t$$

boundary conditions at base of bed model (*base*)

$$c^m_{new,base} = c^m_{ini,base} \quad (3)$$
$$c^{sa}_{new,base} = c^{sa}_{ini,base}$$

compute total mass concentration

$$c^t = c^m + c^{sa} \quad (4)$$

compute mud fraction

$$\xi^m = c^m / c^t \quad (5)$$

solve bed composition diffusion equation

$$\frac{\partial \xi^m}{\partial t} - \frac{\partial}{\partial z}\varepsilon_b \frac{\partial \xi^m}{\partial z} = 0 \quad (6)$$

Assess critical shear stress for erosion

$$\tau_{e,n} = \tau_{e,n,input} \tag{7}$$

$$\text{if } \tau_{e,c} \neq 99999 \text{ than } \tau_{e,c} = \tau_{e,c,input}$$
$$\text{else } \tau_{e,c} = 0.163\,\mathrm{PI}^{0.84} \tag{8}$$

Assess mode of erosion

If $\xi^m \leq 0.3$ than non-cohesive bed

If $\xi^m > 0.3$ than cohesive bed

Note that in case of a constant silt-clay ratio 4:1, this would yield a critical clay content of 6 %.

Water-bed exchange for non-cohesive bed

If $\tau_b \leq \tau_{e,n}$ then

$$\begin{aligned} E^{sa} - D^{sa} &= \gamma W_s^{sa}\left(c_e^{sa} - c^{sa}\right) \\ E^m &= 0 \\ D^m &= W_s^m c^m \end{aligned} \tag{9}$$

If $\tau_b > \tau_{e,n}$ then

$$\begin{aligned} E^{sa} - D^{sa} &= \gamma W_s^{sa}\left(c_e^{sa} - c^{sa}\right) \\ E^m &= \xi^m M_n^m \left(\frac{\tau_b - \tau_{e,n}}{\tau_{e,n}}\right) \\ D^m &= W_s^m c^m \end{aligned} \tag{10}$$

Water-bed exchange for cohesive bed

If $\tau_b \leq \tau_{e,c}$ then

$$\begin{aligned} E^{sa} &= 0 \\ D^{sa} &= W_s^{sa} c^{sa} \\ E^m &= 0 \\ D^m &= W_s^m c^m \end{aligned} \tag{11}$$

If $\tau_b > \tau_{e,c}$ then

$$E^{sa} = \xi^{sa} M_c^{\,m} \left(\frac{\tau_b - \tau_{e,c}}{\tau_{e,c}} \right)$$
$$D^{sa} = W_s^{sa} c^{sa} \qquad (12)$$
$$E^{m} = \xi^{m} M_c^{\,m} \left(\frac{\tau_b - \tau_{e,c}}{\tau_{e,c}} \right)$$
$$D^{m} = W_s^{m} c^{m}$$

Limitation of application
The formula presented in this algorithm describe floc and surface erosion. Mass erosion is not covered. Moreover, this model can be applied at low suspended sediment concentrations only (i.e. below a few 100 mg/l).
Equation (6) does not allow for morphological changes.

Validation
The algorithms have been tested through a sensitivity analysis on a tidal inlet and basin in the Dutch Wadden Sea. They have not been validated directly against field or laboratory data.

2.6.1.1 EP16.1 - Classification of sand-mud mixtures

In this section the empirical/heuristic sediment classification diagram commonly used in sedimentology (e.g. Flemming, 2000) is quantified with the use of some soil mechanical tools. First, distinction is made between cohesive and non-cohesive soils. This is done with the so-called Activity Plot on basis of the Atterberg limits. An example is given in Figure A.1 for mud samples from the Port of IJmuiden, The Netherlands.

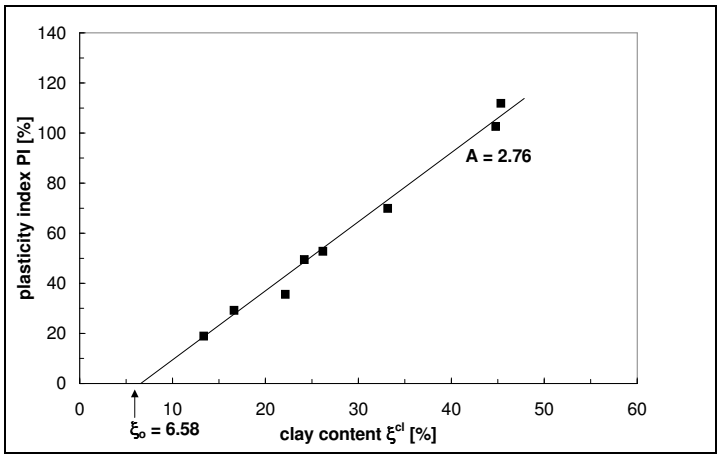

Figure A.1 Activity-plot for IJmuiden mud (Winterwerp & Van Kesteren, 2004)

The plasticity index PI is defined as PI = LL – PL, where LL is the liquid limit and PL is the plastic limit. The clay content ξ^{cl} is defined as the sediment fraction with particle size < 2 μm. The intercept ξ_0 of the fit through the data with the ξ-axis (i.e. at PI = 0) yields the critical clay content beyond which the sediment acquires cohesive properties. Note

that in general 5 % < ξ_0 < 10 %, whereas the slope A (A = PI/(ξ^{cl}-ξ_0) of this fit is called the activity, which value is uniquely determined by the clay minerals involved.

The granular network structure of the sediment, also referred to as the sediment's skeleton, is the second important parameter that governs the behaviour of sediment mixtures. Such a structure is sketched in Figure A.2.

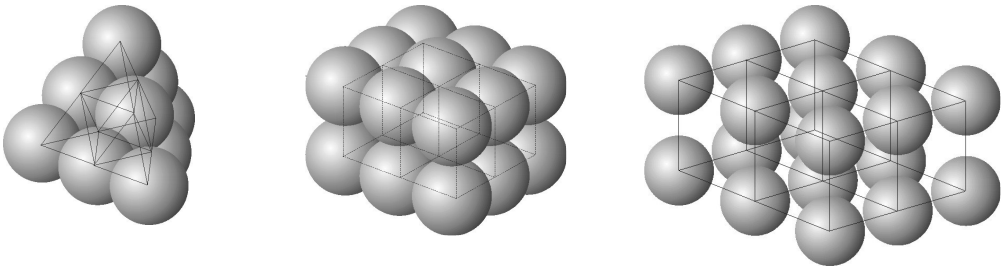

Figure A.2 Network structure of granular material

The left panel of Figure 2 shows a tetrahedral packing of spherical grains; under deformation, the particles have to dilate. The grains in the right panel do not form a network structure and the grains are merely space filling. The cubic-centred packing in the middle panel is the most loose packing in which grains can still support each other – it is referred to as the critical packing. For spherical particles the critical porosity amounts to n_c = 47.6 %. The actual critical porosity for natural sediment depends on the roundness and uniformity (D_{60}/D_{10}) of the sediment; typically values are 40 % < n_c < 50 % (e.g. Winterwerp & Van Kesteren, 2004).

The granular composition (clay: D < 2 μm; silt: 2 < D < 63 μm; and sand: D > 63 μm) is plotted in the sand-silt-clay triangle, as in Figure A.3 for sediment from the Western Scheldt.

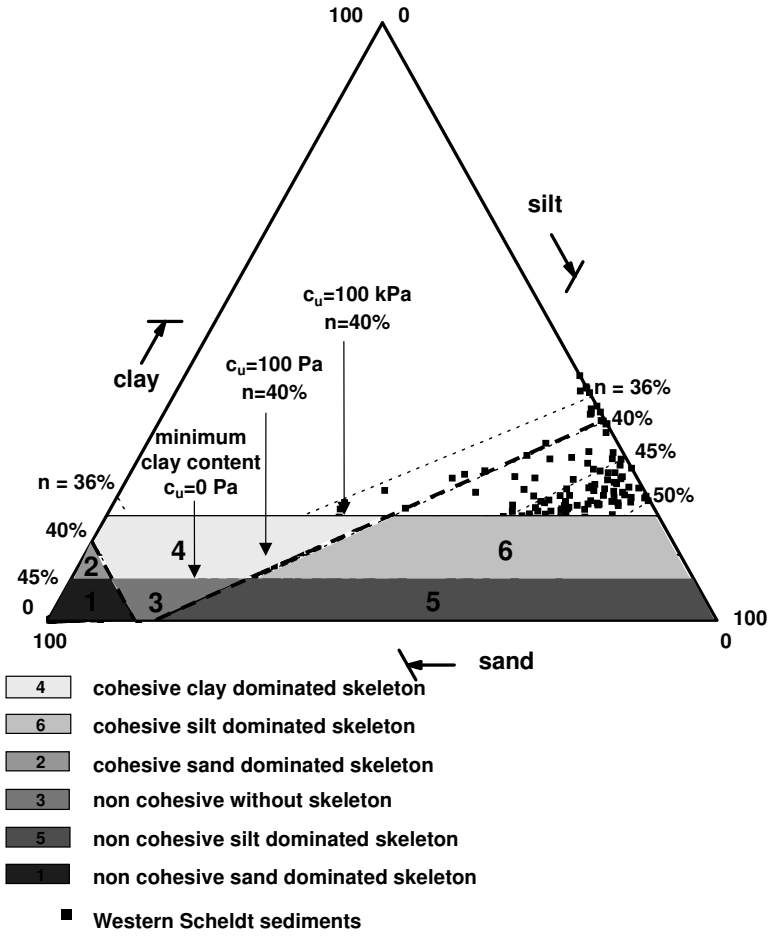

Figure A.3 Classification in sand-silt-clay diagram, $c_u = 0$ at $\xi^{cl} = \xi_0$

In Figure A.3 the demarcation between cohesive and non-cohesive beds (ξ^{cl} = 7 % for Western Scheldt sediment) is indicated by a horizontal line. By definition, the remoulded shear strength c_u of non-cohesive sediment is zero. We have also drawn lines for c_u = 100 Pa and c_u = 100 kPa. The remoulded shear strength is a material parameter that is easily determined and can be deployed to quantify the erodibility of cohesive sediment beds.

Next we draw the demarcation for network structure, i.e. the critical porosity for a sand skeleton and for a silt skeleton; in Figure A.3 we assume n_c = 40 % for illustration.

The cohesive and skeleton demarcation lines divide the sand-silt-clay triangle in six sub-zones distinguishing six modes of sand-mud behaviour:

1. non-cohesive sediment dominated by sand skeleton
2. cohesive sediment dominated by sand skeleton
3. non-cohesive sediment with unstable skeleton
4. cohesive sediment dominated by clay skeleton
5. non-cohesive sediment dominated by silt skeleton
6. cohesive sediment dominated by silt skeleton.

Note that the data from the Western Scheldt suggest that the ratio of clay and silt content is constant and about 1:4. Hence a critical clay content $\xi_0^{cl} = 0.07$ corresponds to a critical mud content $\xi_0^m = 0.35$. A similar observation was reported by Flemming (2000), but with different silt-clay ratios. It is therefore useful to combine the clay and silt fraction in the mud fraction. This is a very convenient observation, as it implies that the sediment composition can be measured through the sand content only, as $\xi^{sa} = 1 - \xi^{cl} - \xi^{si} = 1 - \xi^m$. This also agrees with an empirical relation derived by Allersma (1988):

$$\rho_{dry} = 480\alpha_c + (1300 - 280\alpha_c)\xi^{sa\,0.8} \tag{A.1}$$

which relates the dry bed density ρ_{dry} to the sand content ξ^{sa} only, and where α_c is a consolidation coefficient, ranging from $\alpha_c = 0$ for fresh deposits to $\alpha_c = 2.4$ for old, well-consolidated deposits.

These observations can be used to construct the sediment-phase diagram of Figure A.4, where the vertical axis now reflects the entire sediment composition from a granular point of view, and the horizontal axis the dry bed density. If the six modes of sediment behaviour are plotted within this graph, together with the empirical equ. (A.1), we note that in fact only three modes may occur in the Western Scheldt:

mode 1: non-cohesive sand dominated behaviour,
mode 3: non cohesive very loose (supercritical, i.e. sensitive to liquefaction) sand/silt skeleton, and
mode 4: cohesive clay dominated behaviour.

This classification enables us to assess the behaviour of the seabed and to select appropriate formulae describing the erosion of sediment mixtures.

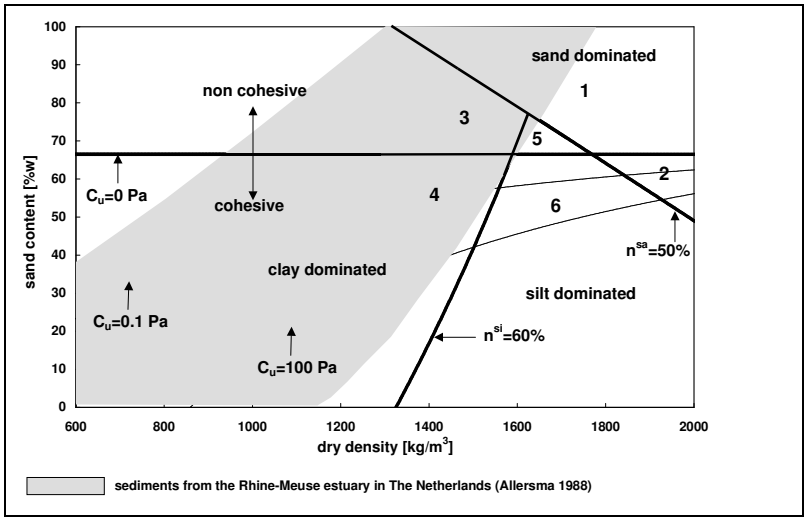

Figure A.4 Sediment-phase diagram for Western Scheldt sediments; the shaded area represents natural sediments, e.g. eq (1)

2.6.1.2 EP 16.2 - Erosion of sand-mud mixtures

Natural sediments often consist of a mixture of sand and mud (e.g. silt and clay). A conceptual framework to analyse and classify these sediment mixtures has been presented above.

A few studies on the behaviour of sand-mud mixtures have been reported in literature. Kandiah (1984) showed empirically that the effect of sand content on the erodibility of cohesive soils is a function of the SAR of the pore water. Kandiah reasoned that the strength of a bed is determined by clay-clay bonds and clay-sand bonds. At high SAR, the clay-clay bonds would be weaker than the clay-sand bonds, and an increase in clay content would result in a decrease in overall bed strength, i.e. an increase in erodibility. At small SAR the opposite would happen, and an increase in clay content yields an increase in overall bed strength.

In the 1990's a number of laboratory experiments on sand-mud mixtures were carried out, e.g. Torfs (1995) and Williamson (1993 – see Chesher and Ockenden, 1997 and Whitehouse et al., 2000). Chesher and Ockenden (1997) schematised the results in a simple diagram that was used in a depth-averaged sediment transport model of the Mersey estuary. In this diagram, the critical shear stress for erosion τ_e first increases and then decreases with increasing mud content, starting from a pure sand bed.

The various experimental data were further analysed by Torfs et al. (2001), who found that τ_e increased with increasing mud content, except at mud contents of a few percent, when a small decrease in τ_e was observed, as shown in Figure B.1. Note that Figure B.1 suggests an off-set in erosional behaviour, similar to the definition of ξ_0 (Figure B.1). Figure B.1 also shows the empirical relation equ. A.1 for the case the mud fraction equals the clay fraction, which was the case for the experiments of Torfs for various values of the activity *A*. The measured data of Torfs appear to correspond well with an activity of $A = 1.5$ $\left(A = \mathrm{PI} \middle/ \left(\xi^{cl} - \xi_0\right)\right)$.

Smerdon and Beasley (1959) found an empirical relation between τ_e and PI:

$$\tau_e = 0.163\,\mathrm{PI}^{0.84} \qquad \text{(B.1)}$$

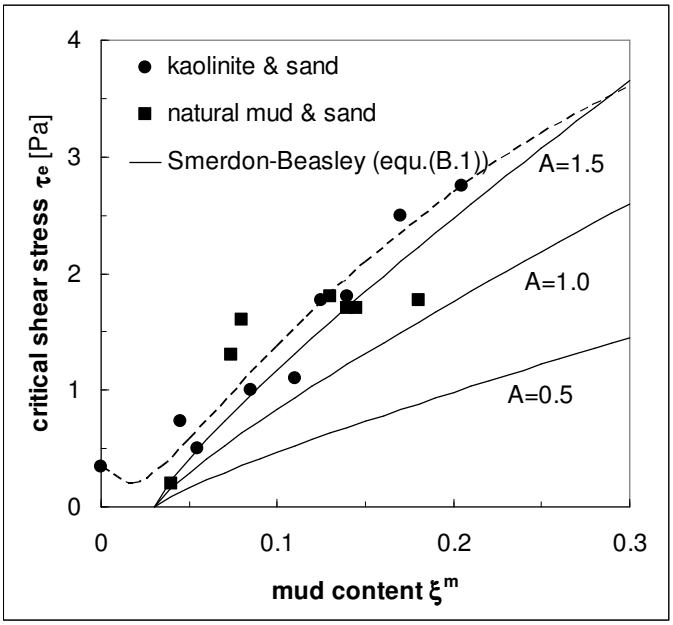

Figure B.1 Critical shear strength for erosion as a function of mud content ξ^m (redrawn from Torfs et al., 2001)

Note that Van Ledden et al. (2004) found the behaviour of cohesive sediment mixtures, such as erodibility, is related to the clay fraction instead of the mud fraction.

Van Ledden (2003) presented a thorough analysis of the various studies on sand-mud mixtures. On the basis of this analysis, and on the classification of sand-mud beds, he proposed two heuristic erosion formulae. In the non-cohesive regime sand and mud particles behave independently and the individual sediment components do not affect the erodibility of the other constituent. Hence:

$$\begin{aligned} E^{sa} - D^{sa} &= \gamma W_s \left(c_e^{sa} - c^{sa} \right) \\ E^m &= \xi^m M_n^m \left(\frac{\tau_b - \tau_{e,n}}{\tau_{e,n}} \right) \quad \text{for} \quad \tau_b > \tau_{e,n} \end{aligned} \tag{B.2}$$

where c_e^{sa} is the equilibrium concentration for sand and γ is a form coefficient.

In the cohesive regime, erosion is governed by the cohesive nature of the bed, and sand particles are passive: they are eroded with the mud particles at a rate proportional to their fraction:

$$\begin{aligned} E^{sa} &= \xi^{sa} M_c^m \left(\frac{\tau_b - \tau_{e,c}}{\tau_{e,c}} \right) \quad \text{for} \quad \tau_b > \tau_{e,c} \\ E^m &= \xi^m M_c^m \left(\frac{\tau_b - \tau_{e,c}}{\tau_{e,c}} \right) \quad \text{for} \quad \tau_b > \tau_{e,c} \end{aligned} \tag{B.3}$$

Note that the thresholds for erosion of a cohesive and non-cohesive bed $\tau_{e,c}$ and $\tau_{e,n}$ may be different. However, we assume that in the cohesive regime, sand and mud are eroded at the same relative rate.

The bed composition is modelled with a diffusion equation proposed by Armanini (1995):

$$\frac{\partial \xi^{sa}}{\partial t} - \frac{\partial}{\partial z}\varepsilon_b \frac{\partial \xi^{sa}}{\partial z} = 0 \qquad \text{(B.4)}$$

in which the bed diffusion coefficient ε_s is modelled as:

$$\varepsilon_b = \alpha_0 u_* h \exp\{-z/L_p\} \qquad \text{(B.5)}$$

Typical values for α_0 and L_p are: $\alpha_0 \cong 10^{-6}$ and L_p = 0.01 – 0.1 m. See Van Ledden (2002 and 2004) for more details.

References

Allersma, E., 1988, Morphological studies for the Rhine-Meuse estuary – morphological modelling Part IV: composition and density of sediment, Delft Hydraulics, Report Z71-03 (in Dutch).

Armanini, A., 1995, Non-uniform sediment transport: dynamics of the active layer, Journal of Hydraulic Research, Vol 33, No 5, pp 611-622.

Chesher T.J. and M.C. Ockenden, 1997, Numerical modelling of mud and sand mixtures, in N. Burt, R. Parker and J. Watts, Cohesive Sediments, John Wiley & Sons, Chichester, 395-406.

Flemming, B.W., 2000, A revised textural classification of gravel-free muddy sediments on the basis of ternary diagrams, Continental Shelf Research, 20, 1125-1137.

Kandiah, 1974, Fundamental aspects of surface erosion of cohesive soils, PhD-thesis, University of California, USA.

Mitchener, H.J., Torfs, H. and Whitehouse, R.J.S., 1996, Erosion of mud/sand mixtures, Coastal Engineering, 29, 1-25 (errata, 1997, 30, 319).

Smerdon, E.T. and Beasley, R.P., 1959, The tractive force applied to stability of open channels in cohesive soils, University of Missouri, Research Bulletin 715.

Torfs, H., 1995, Erosion of sand/mud mixtures, PhD-thesis, Katholieke Universiteit Leuven, Leuven, Belgium.

Torfs, H., J. Jiang and A.J. Mehta, 2001, Assessment of the erodibility of fine/coarse sediment mixtures, in W.H. McAnally and A.J. Mehta, Coastal and Estuarine Fine

Sediment Processes, Proceedings in Marine Science, Vol 3, Elsevier, Amsterdam, pp 109-123.

Van Ledden, M., 2001, a process-based sand-mud model, in J.C. Winterwerp and C. Kranenburg, Fine Sediment Dynamics in the Marine Environment, Proceedings in Marine Science, Vol 5, Elsevier, Amsterdam, 577-594.

Van Ledden, M., 2003, Sand-mud segregation in estuaries and tidal basins, PhD-thesis, Delft University of Civil Engineering.

Van Ledden, M., W.G.M. van Kesteren and J.C. Winterwerp, 2004, A classification for erosion behaviour of sand-mud mixtures, Continental Shelf Research, Vol 24, pp 1-11.

Whitehouse, R., R. Soulsby, W., Roberts and H. Mitchener, 2000, Dynamics of estuarine muds, HR Wallingford, DETR, Thomas Telford, London, pp 210.

Winterwerp, J.C., W.G.M. van Kesteren, 2004, Introduction to the physics of cohesive sediments in the marine environment, Elsevier, Developments in Sedimentology, 56.

2.7 Understanding of the sediment transport profile

2.7.1 EP17 - Algorithm for understanding of the sediment transport profile (HRW – Soulsby)

Algorithm Version 1

Aim To devise an analytical formula for the concentration of mud in a tidal flow, and examine how this varies with the properties of the mud.

Scientific background

Sophisticated numerical models of the erosion, suspension, transportation and deposition of mud in estuaries usually make use of rather simple formulae for determining the erosion and deposition rates in terms of the flow behaviour (especially the bed shear-stresses) and the physical properties of the mud. Traditionally the mud is described for modelling purposes by only four parameters:

- the threshold shear-stresses for erosion and deposition and the erosion-rate constant for the mud bed, and the settling velocity of the suspended mud just above the bed. (The settling velocity is sometimes made a function of the mud concentration, making five instead of four parameters.)

The present work examines how these four parameters interact with the flow-generated bed shear-stresses in the simplest possible representation of a tidal estuary to determine the concentrations of mud in suspension and the masses of mud eroded and deposited per unit area. This gives insight into the values of parameters to choose to simulate known behaviour in real estuaries, and the effect that variations in the parameters will have.

The estuary is assumed to be of uniform depth in both horizontal directions, and the mud properties to be horizontally uniform. The tidal depth variation is ignored, and the flow is represented by a repeating rectilinear tidal velocity such that the bed shear-stress varies sinusoidally as $\tau(t) = \hat{\tau} . \sin(\omega t)$. The settling velocity of the suspended mud is treated as constant, and the concentration profile is schematised as a linear variation from bed to surface $C(z) = C_b.(1-\alpha.z/h)$. The depth-averaged concentration is thus proportional to the bottom concentration by $\overline{C} = \beta C_b$, where $\beta = 1 - \alpha/2$. The pattern of erosion and deposition through the tide then gives rise to a concentration of suspended mud that varies through the tidal cycle, and repeats periodically. The algorithm gives algebraic expressions for the bottom concentration at slack water, and the maximum and minimum bottom concentrations in the tidal cycle. The full derivation is given in Soulsby (2004).

Improvement in understanding

The algorithm gives the following benefits:

- it allows a rough estimate of the suspended concentration of mud to be made without the need to set up and run a full numerical model
- this estimate may be good enough for initial investigations into a practical problem, and desk-study solutions

- if measured calibration/validation data of concentrations is available for a study area, it enables the values of the various parameters to be set in a full numerical model to (approximately) reproduce this
- it gives insight into the way that the values of the various parameters interact to determine the concentrations, and the sensitivity to changes in the parameters.

Implementation

The algorithm is sufficiently simple that it can either be computed using a pocket calculator, or in a spreadsheet. An example of results from a spreadsheet is given later.

Algorithm

1. Inputs

Water depth (m)	h	
Tidal radian frequency (s^{-1})	ω	(= 1.41×10^{-4} for M_2)
Amplitude of tidal bed shear-stress ($N.m^{-2}$)	$\hat{\tau}$	
Threshold shear-stress for erosion ($N.m^{-2}$)	τ_e	
Threshold shear-stress for deposition ($N.m^{-2}$)	τ_d	
Mud erosion-rate constant ($kg.N^{-1}.s^{-1}$)	m_e	
Settling velocity of flocs ($m.s^{-1}$)	w_s	
Ratio of depth-averaged concentration to bottom concentration	β	

2. Outputs

Bottom concentration at slack water ($kg.m^{-3}$)	C_o	
Maximum bottom concentration through tidal cycle ($kg.m^{-3}$)	C_{max}	
Minimum bottom concentration through tidal cycle ($kg.m^{-3}$)	C_{min}	
Mass of mud eroded per half-cycle ($kg.m^{-2}$)	M_E	
Mass of mud deposited per half-cycle ($kg.m^{-2}$)	M_D	

3. Calculate basic parameters

Check that $\tau_d < \tau_e < \hat{\tau}$ for validity of model assumptions

Calculate A (–)
$$A = \frac{w_s \tau_d}{2\omega\beta h\hat{\tau}} \quad (1)$$

Calculate C_s ($kg.m^{-3}$)
$$C_s = \frac{m_e \hat{\tau}}{\omega\beta h} \quad (2)$$

Calculate ϕ_E (radians)
$$\phi_E = \sin^{-1}\left(\frac{\tau_e}{\hat{\tau}}\right) \quad (3)$$

4. Calculate outputs

The mass of mud *eroded* per unit area of bed in one tidal half-cycle is obtained by integrating the erosion rate while $\tau > \tau_e$:

$$M_E = \frac{2m_e}{\omega}\left[\left(\hat{\tau}^2 - \tau_e^2\right)^{1/2} - \tau_e\left(\frac{\pi}{2} - \phi_E\right)\right] \quad (4)$$

The mass of mud *deposited* per unit area of bed in one tidal half-cycle is obtained by integrating the deposition rate while $\tau < \tau_d$:

$$M_D = 2\beta h\, C_o \sinh(A) \quad (5)$$

In Eq (5), the value of C_o is not yet determined. For an equilibrium repeating tide, the eroded and deposited masses per half-cycle are equal, so C_o can be obtained by equating Eqs (4) and (5):

$$C_o = \frac{C_s}{\sinh(A)}\left\{\left[1 - \left(\frac{\tau_e}{\hat{\tau}}\right)^2\right]^{1/2} - \left(\frac{\tau_e}{\hat{\tau}}\right)\left(\frac{\pi}{2} - \phi_E\right)\right\} \quad (6)$$

The maximum concentration occurs at the end of the erosion phase, and is:

$$C_{max} = C_o \exp(A) \quad (7)$$

The minimum concentration occurs at the end of the deposition phase, and is:

$$C_{min} = C_o \exp(-A) \quad (8)$$

The bottom concentrations C_o, C_{max}, C_{min} can be converted to depth-averaged concentrations by multiplying them by the factor β.

Limits of applicability

The model is based on a number of simplifying assumptions that need to be at least approximately valid:

1. The flow and bed properties are assumed to be horizontally uniform, hence it is not expected to be accurate in areas where either the flow or the bed-composition vary rapidly with position (e.g. near headlands, in small bays, near sandbanks).
2. Advection of mud is neglected (corollary of the above assumption), which in many estuaries will be an important, and sometimes dominant, effect.
3. Only pure cohesive mud is considered, without sand present.
4. The concentration profile is assumed to be linear, and to change at all levels instantaneously when the bottom concentration changes. This means that the timescale for response of the profile (say h/w_s) should be either short or long compared with the time-scale of change in velocity (say 3 hours for a semi-diurnal tide).
5. The settling velocity is assumed to be constant and independent of concentration, so that power-law dependence on concentration, and hindered settling, are both excluded. The exclusion of hindered settling restricts the concentrations to less than about 5 kg/m^3.
6. The method is only as good as the erosion and deposition laws on which it is based.

Although these assumptions seem rather restrictive, some of them apply also to many full numerical models.

Validation

Tests have not been made against measured concentrations. This would require field data in which the concentrations and the values of the various mud properties have all been measured, in a situation that approximates to the assumptions listed above. However, examples of concentrations for typical values of the mud properties have been calculated in a spreadsheet and are shown below. The peak shear-stress $\hat{\tau}$ is calculated from the peak tidal current speed U_{max} using the smooth-turbulent drag coefficient devised by Soulsby in Section 2.4.1, EP13. The thresholds of erosion and deposition are given a range of values relative to the maximum shear-stress, subject to $\tau_d < \tau_e < \hat{\tau}$. The range of concentrations obtained looks plausible. Values of concentration > 5 kg/m^3 are highlighted as being outside the limit of applicability because hindered settling is not included. The concentrations decrease strongly as τ_e increases, and decrease with increasing τ_d for a fixed τ_e. All concentrations are directly proportional to m_e. The variation in concentration through a tidal cycle C_{max}/C_{min} [= exp(2A)] varies from about 1.5 for the largest concentrations to about 40 for the smallest concentrations. The absolute values of concentration depend primarily on the erosion parameters m_e and τ_e, whereas the ratio of max to min depends on the deposition parameters w_s and τ_d.

Gaps in knowledge

This method could usefully be extended to use alternative assumptions, for example:

- assume a concentration-dependent settling velocity, possibly including hindered settling
- assume a profile shape based on eddy-diffusion considerations
- allow the profile shape to adapt with time
- replace the Krone law for deposition with the more plausible version proposed by Winterwerp (see Algorithm EP16)
- replace the sinusoidal variation in shear-stress with an asymmetrical variation (e.g. flood-dominant velocities)
- replace the sinusoidal variation with a full spring-neap cycle

The limits of mathematical tractability might be stretched by some of these extensions. It would nevertheless be desirable to obtain algebraic solutions that retain the insight that formulae give, rather than using an (albeit simple) numerical scheme.

References

Soulsby, R.L. (2004). Methods for predicting suspensions of mud. Report TR104, HR Wallingford Ltd.

Table showing spreadsheet output from the mud concentration algorithm

Concentrations at slack water C_0 , maximum C_{max} , and minimum C_{min}

depth h	5	m			
tidal period	12.4	hours	omega	0.000141	s^-1
U_{max}	0.8	m/s	tau_{max}	0.656793	N/m^2
m_e	0.001	kg/N/m			
w_s	0.002	m/s			
beta	0.67		C_s	1.392925	kg/m^3

Key	
	Input value
	Computed value
	$tau_d > tau_e$
	Conc > 5 kg/m^3

Table of C_0 **kg/m^3** **Concentration at slack water**

A	tau_d/tau_{max}									
1.908719	0.9									0.013
1.696639	0.8								0.045	0.016
1.484559	0.7							0.105	0.057	0.020
1.272479	0.6						0.206	0.133	0.072	0.025
1.0604	0.5					0.375	0.267	0.173	0.093	0.033
0.84832	0.4				0.661	0.500	0.356	0.230	0.124	0.044
0.63624	0.3			1.176	0.927	0.701	0.499	0.322	0.175	0.061
0.42416	0.2		2.250	1.830	1.443	1.091	0.777	0.502	0.272	0.096
0.21208	0.1	5.528	4.602	3.743	2.952	2.232	1.588	1.026	0.555	0.195
	tau_e/tau_{max}	0.1	0.2	0.3	0.4	0.5	0.6	0.7	0.8	0.9
phi_E		0.100167	0.201358	0.304693	0.411517	0.523599	0.643501	0.775397	0.927295	1.11977

Table of C_{max} **kg/m^3** **Max bottom concentration, occurs at end of erosion phase**

A	tau_d/tau_{max}									
1.908719	0.9									0.085
1.696639	0.8								0.246	0.086
1.484559	0.7							0.462	0.250	0.088
1.272479	0.6						0.736	0.476	0.258	0.091
1.0604	0.5					1.084	0.771	0.498	0.270	0.095
0.84832	0.4				1.545	1.168	0.831	0.537	0.291	0.102
0.63624	0.3			2.222	1.752	1.325	0.943	0.609	0.330	0.116
0.42416	0.2		3.439	2.797	2.206	1.668	1.187	0.767	0.415	0.146
0.21208	0.1	6.833	5.689	4.627	3.649	2.760	1.963	1.268	0.687	0.241
	tau_e/tau_{max}	0.1	0.2	0.3	0.4	0.5	0.6	0.7	0.8	0.9
phi_E		0.100167	0.201358	0.304693	0.411517	0.523599	0.643501	0.775397	0.927295	1.11977

Table of C_{min} **kg/m^3** **Min bottom concentration, occurs at end of deposition phase**

A	tau_d/tau_{max}									
1.908719	0.9									0.002
1.696639	0.8								0.008	0.003
1.484559	0.7							0.024	0.013	0.005
1.272479	0.6						0.058	0.037	0.020	0.007
1.0604	0.5					0.130	0.092	0.060	0.032	0.011
0.84832	0.4				0.283	0.214	0.152	0.098	0.053	0.019
0.63624	0.3			0.622	0.491	0.371	0.264	0.171	0.092	0.032
0.42416	0.2		1.472	1.197	0.944	0.714	0.508	0.328	0.178	0.062
0.21208	0.1	4.471	3.722	3.027	2.388	1.806	1.285	0.830	0.449	0.158
	tau_e/tau_{max}	0.1	0.2	0.3	0.4	0.5	0.6	0.7	0.8	0.9
phi_E		0.100167	0.201358	0.304693	0.411517	0.523599	0.643501	0.775397	0.927295	1.11977

2.7.2 EP18 - Algorithm for mass settling flux of flocculated cohesive sediment (Plymouth – Manning)

Aim To calculate the mass settling flux of flocculated cohesive sediment in a turbulent estuarine water column.

Scientific background
For predicting the transport and fate of sediment movement in estuaries, the determination of the various spatial and temporal mass fluxes is essential. One area which has caused numerous problems, is the modelling and parameterised description of the vertical mass settling flux of fine cohesive sediment, which becomes the depositional flux close to slack water. This flux is the product of the suspended particulate matter (SPM) concentration and the settling velocity. For non-cohesive sediment this is a relatively simple process as the settling velocity is proportional to the particle size. Whereas estuarine muds, which are composed of combinations of clay minerals and different types of biological matter, have the potential to flocculate in to larger, low density aggregates called flocs.

Turbulent shear generated in estuarine water columns is recognised as having a controlling influence on both the formation of mud flocs, and their break-up (Manning, 2004a). However, to date there have been no *in-situ* studies which have quantified the flocculation process with the specific emphasis of taking floc effective density, and consequently particulate mass distribution variations, into account, within both continually changing estuarine suspended concentration gradients and varying intensities of turbulent mixing. This is mainly due to the fragility of the fastest settling macroflocs, which are easily broken-up upon sampling.

The new flocculation model, developed as part of the EstProc project, is based entirely on empirical observations made using low intrusive floc and turbulence data acquisition techniques, from a wide range of estuarine water column conditions. In particular, the floc population size and settling velocity spectra were sampled using the unique video-based INSSEV: *IN-Situ* SEttling Velocity instrument, which was developed at the University of Plymouth. This provided a total of 157 floc data sets, from experiments conducted within the framework of three recent European Commission funded projects: COSINUS, SWAMIEE and INTRMUD (see Manning, 2004b).

The algorithms were generated by a parametric multiple regression statistical analysis of key parameters which were generated from the raw spectral data (detailed derivations and testing of the algorithms are described in: Manning, 2004c; Manning and Dyer, 2004). The multi-regression identified the key components which best quantitatively describe a floc population as being:

- the changes in the macrofloc (flocs size > 160 μm) and microfloc (flocs size < 160 μm) settling velocities ($Ws_{macroEM}$ and $Ws_{microEM}$), together with how the suspended matter is distributed across each floc sub-population ($SPM_{ratioEM}$).

Improvement in understanding
The new method improves on existing methods because:

- The algorithm is based on a multiple regression analysis of 157 uniquely comprehensive empirical flocculation and turbulence data sets, which were acquired from three different estuarine field experiments and two laboratory studies.
- The algorithm can estimate the settling velocity of both the macrofloc and microfloc sub-populations, in response to changes in turbulence and SPM concentration at an individual temporal and spatial point in an estuarine water column simulation. This method can also apportion the concentration distribution between the macrofloc and microfloc fractions, and correlate this floc mass to the respective settling velocities of each fraction.
- Typically these algorithms only require the input of two variables (turbulent shear stress and SPM concentration), which simplifies their inclusion in numerical simulation sediment transport models, and reduces computer processing time.
- The flocculation algorithm has extreme flexibility in adapting to a wide range of estuarine environmental conditions, specifically for applied modelling purposes, by producing reliable mass settling flux predictions in both quiescent waters, and on the rare occurrence of very turbulent events experienced during extremely high flow velocity conditions, where near-bed shear stresses could potentially reach the order of 1-10 N m^{-2}. The derived mass flux values are also valid for both water columns of very low turbidity and highly saturated benthic suspension layers with concentration approaching 8.6 g l^{-1}.
- It has been tested against independently acquired *in-situ* data sets, and gives good agreement.

Implementation
The algorithm is written in a step-by-step "recipe" style, which can easily be coded for numerical computer applications. The complete algorithm will calculate mass settling flux, or the three main components (equations *A1*, *A2* and *A4*) can be used in a stand-alone mode if required.

Algorithm

Inputs
The algorithm can be implemented in 1D, 2D and 3D models providing data inputs of the following parameters:

Turbulent shear stress (N m^{-2})	τ
Suspended particulate matter concentration (mg l^{-1})	SPM
Root mean square of the gradient in turbulent velocity fluctuations (s^{-1})	G
Von Karman constant (no units)	κ
Kinematic viscosity (m^2 s^{-1})	ν
Water density (kg m^{-3})	ρ_w
Distance above the estuary bed (m)	z

Outputs
In the most complex application, 3D, the algorithm can calculate the following outputs for each point (node) on a predetermined three-dimensional numerical model grid:

Macrofloc settling velocity (mm s^{-1})	$Ws_{macroEM}$
Microfloc settling velocity (mm s^{-1})	$Ws_{microEM}$

Suspended particulate matter ratio (no units) $SPM_{ratioEM}$
Total mass settling flux ($mg.m^{-2} s^{-1}$) MSF_{EM}

Calculate macrofloc settling velocity
For τ ranging between 0.04-0.7 N m^{-2}:

$$Ws_{macroEM} = 0.644 + 0.000471\ SPM + 9.36\ \tau - 13.1\ \tau^2 \quad (A1a)$$

For τ ranging between 0.6-1.5 N m^{-2}:

$$Ws_{macroEM} = 3.96 + 0.000346\ SPM - 4.38\ \tau + 1.33\ \tau^2 \quad (A1b)$$

For τ ranging between 1.4-5 N m^{-2}:

$$Ws_{macroEM} = 1.18 + 0.000302\ SPM - 0.491\ \tau + 0.057\ \tau^2 \quad (A1c)$$

- Continuity between each relationship can be achieved by calculating a $Ws_{macroEM}$ value using both adjacent equations (at a specific τ) and obtaining a single transitional $Ws_{macroEM}$ value from linear interpolation.
- The transition shear stress zone between eqns *A1a-A1b* is 0.6-0.7 N m^{-2}.
- The transition shear stress zone between eqns *A1b-A1c* is 1.4-1.5 N m^{-2}.

Calculate the microfloc settling velocity
For τ ranging between 0.04-0.55 N m^{-2}:

$$Ws_{microEM} = 0.244 + 3.25\ \tau - 3.71\ \tau^2 \quad (A2a)$$

For τ ranging between 0.51-10 N m^{-2}:

$$Ws_{microEM} = 0.65\ \tau^{-0.541} \quad (A2b)$$

- Continuity between each relationship can be achieved by calculating a $Ws_{microEM}$ value using both adjacent equations (at a specific τ) and obtaining a single transitional $Ws_{microEM}$ value from linear interpolation.
- The transition shear stress zone occurs between a τ of 0.51-0.55 N m^{-2}.

Calculate an alternative turbulence parameter format (optional)
If both equations *A1* and *A2* are to be incorporated into the framework of a numerical model where the turbulence input parameter is of the turbulent shear G format, all the τ functions must be replaced with the following τ_{mod} equation:

$$\tau_{mod} = \rho_w\ [(G^2\ .\ \kappa\ .\ \nu\ .\ z)^{1/3}]^2 \quad (A3)$$

This is because unlike the τ parameter, corresponding values of G are dependent on their height in the water column relative to the estuary bed.

Calculate the suspended particulate matter ratio

$$SPM_{ratioEM} = 0.815 + 0.00318\ SPM - 0.00000014\ SPM^2 \quad (A4)$$

Calculate the total mass settling flux

$$MSF_{EM} = \left[\left(1 - \frac{1}{1+SPM_{ratioEM}}\right)\cdot\left(SPM\,Ws_{macroEM}\right)\right] + \left[\frac{1}{1+SPM_{ratioEM}}\cdot\left(SPM\,Ws_{microEM}\right)\right] \qquad (A5)$$

Limits of applicability

The algorithm is applicable where there is high resolution coverage of SPM concentration and turbulent shear stress; either as an empirical data set or values generated by a numerical model.

No multiple regression data points were available for SPM concentrations over 1 g l^{-1} when the turbulent shear stress fell below 0.1 N m^{-2}, and therefore this should be regarded as a further boundary limit to equation *A1a*.

The lower limit of SPM concentration to which the approach is applicable is considered to be 10 to 20 mg l^{-1}.

What has been found is that the SPM ratio related to concentration. The key parameters were evaluated from the large dataset using statistical methods and the best components were identified. The combined parameter of turbulence and sediment concentration did not improve the situation for prediction of microfloc settling. It was found that the microflocs were more influenced by turbulence as they are the building blocks for macroflocs, which have a dependence on turbulence AND concentration. The macroflocs comprised aggregates of microflocs. The SPM ratio mass concentration distribution was found to be related just to sediment concentration. The correlation was not perfect statistically but the trend was indicative of the situation especially when flocculation is at a peak and settling flux increases. Older formulations related floc settling velocity just to concentration but now we find that is not sufficient to provide a good relationship.

Validation

The algorithms were tested against data acquired from a series of field experiments funded by the Natural Environmental Research Council which were conducted in the upper reaches of the Tamar estuary (UK), and placed the measurements within the tidal trajectory of the turbidity maximum. For spring tide measurements made on the 15th April 2003, a concentrated benthic suspension layer formed in close proximity to the bed on the ebb producing a peak concentration of 4.2 g l^{-1}. Turbulent shear stresses for the tidal cycle ranged from 0.04-1.6 N m^{-2}. The algorithms calculated the cumulative total mass settling flux for the entire 12.5 hour tidal cycle to within 93% of the measured flux.

The algorithms have been tested within an HR Wallingford TELEMAC-3D numerical model of a cross-section of the Thames estuary, and a 2D and 3D mudflat cross-section process model (see example applications in EstProc final report TR2 or HR Wallingford reports by Baugh and by Spearman).

References

Baugh, J. 2004. Implementation of Manning algorithm for settling velocity in an estuarine numerical model. HR Wallingford report TR146, Rev 1.0, August 2004.

Manning, A.J., (2004a). The observed effects of turbulence on estuarine flocculation. In: P. Ciavola, M. B. Collins and C. Corbau (eds), Sediment Transport in European Estuaries, Journal of Coastal Research Special Issue, SI 41, (in press).

Manning, A.J., (2004b). Observations of the properties of flocculated cohesive sediment in three western European estuaries. In: P. Ciavola, M. B. Collins and C. Corbau (eds), Sediment Transport in European Estuaries, Journal of Coastal Research Special Issue, SI 41, (in press).

Manning, A.J., (2004c). The development of new algorithms to parameterise the mass settling flux of flocculated estuarine sediments, HR Wallingford Technical Report (sub judice).

Manning, A.J. and Dyer, K.R., (2004). Mass settling flux of fine sediments: measurements and predictions. Journal of Geophysical Research, (sub judice).

Spearman, J. 2004. Note on the use of algorithms for modelling mud transport on tidal flats. HR Wallingford report TR144, Rev1.0, August 2004.

2.7.3 EP19 - Algorithm for Generic Models – 1-D single point, 2-D cross-sectional (POL – Lane)

Aim As part of Phase 1 of the UK Estuarine Research Programme, the EMPHASYS project highlighted the capabilities and limitations of 'bottom-up' (dynamical, numerical) and 'top-down' (geo-morphological, rule-based) models. A recommended subsequent objective was the integration of these approaches into 'hybrid' models – this has been pursued in Defra research project FD2107. 'Generic Models', of the form described here, offer a further alternative. These models provide exploratory tools that can be used to:

i) link theory with observations
ii) investigate scaling issues over wide ranges of parameter space
iii) derive appropriate up-scaling of process-study results for incorporation as 'rules' in T-D models or algorithms in B-U models.

Thus, within the aims of the ERP, these models can provide:

i) identification of potential for morphological mode changes
ii) specification of range of operation for B-U models in assembling ensemble outcomes
iii) identification and assessment of algorithms and 'rules'.

Formulation

The following description is extracted from the 1-D model software package. The 2-D version is essentially similar.

Model Description

Random walk particle movements are used to replicate solutions to the 1-D advection-diffusion equation:

$$\underset{\text{change in conc}}{\frac{\partial C}{\partial t}} - \underset{\text{advection (settling)}}{w_s \frac{\partial C}{\partial z}} = \underset{\text{diffusion}}{\frac{\partial}{\partial z}\left(K_z \frac{\partial C}{\partial z}\right)} + \text{source}$$

where C is the suspended sediment concentration, w_s is the fall velocity, and K_z is the vertical eddy diffusivity coefficient.

Erosion

A simple erosion source αU^p is assumed, with coefficient alpha, where p is the power to which the tidal velocity $U = \hat{U} \cos \omega t$ is raised, and ω is the M_2 tidal frequency. The potential erosion in each time step dt is summed until it exceeds a prescribed mass, M of an individual particle. The height of release of each particle corresponds to a normal distribution where the standard deviation sigma = l (diffusive path length - see diffusion, below).

Settlement

Deposition occurs when the height of the particle above the bed calculated from the advective step is less than zero.

Diffusion
Particles are displaced upwards or downwards randomly by a length $l = \sqrt{(2\ Kz\ dt)}$ (Fischer et al., 1979). K_z is approximated by $f\ \hat{U}\ D$ where f is a bed friction coefficient and D is the water depth. Movements 'above' the surface are reflected downwards. Movements 'below' the bed are reflected upwards but reduced by a 'bounce' coefficient b.

Numerical solution
The model simulation extends over N time steps for NC tidal cycles, starting with no particles in suspension. N is chosen so that $dt = P/N$, where P is the tidal period. This produces a random walk length l (see section on diffusion) less than $0.1D$. The solution involves calculation, for successive time steps, of the height above the bed, z of each particle following:

i) an advective movement $-w_s\ dt$ then by
ii) a diffusive displacement. Additional new particles are released into suspension by accumulation of the erosion potential. Likewise particles may be 'lost' by settlement following the advective movement.

Using the model
This model is written in FORTRAN77 and a PC-compatible executable program was developed. Changes to variables are made in the file 'polspm1.dat'. The user is free to modify the source code (in which case a suitable compiler is required). Model results are currently written to the file 'polspm1.out'. If you are interested in the code contact Proudman Oceanographic Laboratory: Andrew Lane, email: ale@pol.ac.uk)

Application
The 1-D model is deliberately designed for maximum simplification. Simulations can involve variations in: $\hat{U}$, D, f, b, α, and P, NC, w_s. The 2D model has been implemented to solve for morphological updating. Figures 1 and 2 show examples of respective applications of these models.

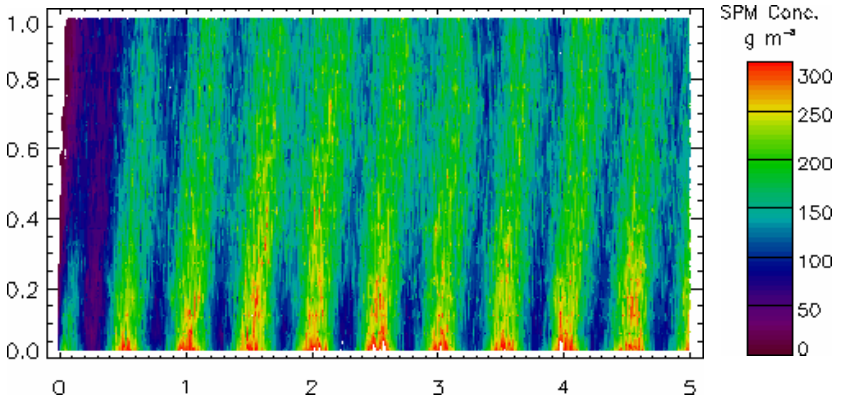

Figure 1 Suspended Particulate concentrations over a spring-neap cycle. (depth 20 m, tidal current amplitude 0.5 m s^{-1}, w_s 10^{-4} m s^{-1}). The axes are time and non-dimensional height in the water column

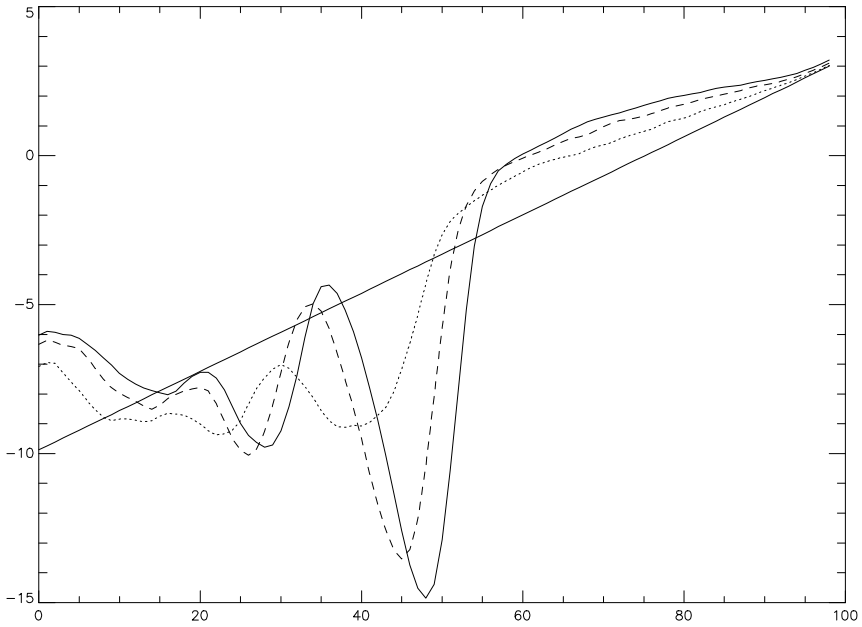

Figure 2 Morphological evolution over 2.5 (dotted line), 5 (dashed line) and 10 (solid line) years for (initial) linear triangular section; from 2D 'y-z' version of model; y axis is height in m and x axis is transverse distance in km from channel centre line
(depth 10 m, tidal amplitude 3 m, w_s = 0.001 m s^{-1} with and without flood defence)

Future developments
Many variations and extensions of these models are possible (see http://www.gotm.net/ for a European network development, extending to ecological applications). With a focus on the UK ERP, envisaged developments include:

i) more complex representation of eddy diffusivity K_z,
ii) mixed sediments (ranges of settling velocities w_s)
iii) flocculation
iv) biological and chemical mediation
v) consolidation
vi) surface wave impact (already tested in 3-D versions)

Incorporation of the above in spring-neap simulations of the 2-D model will provide valuable insight into the sensitivities of estuarine morphologies. This model should be especially valuable in examining the sensitivity of inter-tidal areas (including saltmarsh) to interventions such as flood protection or 'set-back' and to the broader impacts of Global Climate change.

Reference
Fischer, H.B., List, E.J., Koh, R.C.Y., Imberger, J., Brooks, N.H., 1979. Mixing in inland and coastal waters. New York, Academic Press. 483pp.

2.8 Understanding of general sedimentary processes

2.8.1 EP20 - Algorithm for modelling sediment mixing in estuaries (WLD – Winterwerp)

Aim To calculate the initial mixing between fluid mud layer and overflowing water

Scientific background See section 2.8.1.1 to this algorithm

Improvement in understanding This algorithm improves on existing formulae because:

- It is derived from a thorough elaboration of the turbulent kinetic energy equation,
- It distinguishes between a turbulent fluid mud layer and a turbulent overlying water layer,
- It has been tested against laboratory data.

Implementation The new algorithm has been implemented in a MATLAB environment (e.g. section 2.8.1.1) and in the operational DELFT3D software system.

Algorithm

Inputs

water depth (m)	h
depth-averaged flow velocities (m/s)	u, v
water density (kg/m^3)	ρ_0
water viscosity (m^2/s)	ν
shear velocity (m/s)	u_*
fluid mud thickness (m)	δ
depth-averaged fluid mud velocities (m/s)	u_m, v_m
fluid mud density (kg/m^3)	ρ_b
fluid mud viscosity (m^2/s)	ν_m
fluid mud yield strength (Pa)	τ_B
coefficient (-)	c_s ($c_s = 0.25$)
coefficient (-)	c_q ($c_q = 5.6$)
coefficient (-)	c_σ ($c_\sigma = 0.42$)

Outputs

initial entrainment velocity (m/s)	w_e

Calculate mean velocity

mean velocity overlying layer $$U = \sqrt{u^2 + v^2} \quad (1)$$

mean velocity fluid mud layer $$U_m = \sqrt{u_m^2 + v_m^2} \quad (2)$$

Calculate turbulence level and determine mode of entrainment

Reynolds number overlying layer

$$\mathrm{Re} = \frac{Uh}{\nu} \tag{3}$$

effective Reynolds number fluid mud layer

$$\mathrm{Re}_m = \frac{4U_m\delta}{\nu_m} \quad , \quad \mathrm{Re}_\tau = \frac{8\rho_b U_m^2}{\tau_B} \tag{4}$$

$$\frac{1}{\mathrm{Re}_e} = \frac{1}{\mathrm{Re}_m} + \frac{1}{\mathrm{Re}_\tau}$$

if $\mathrm{Re_e} > 3{,}000$ then Case II

if $\mathrm{Re_e} < 3{,}000$ and $\mathrm{Re} > 2{,}000$, then Case I

if $\mathrm{Re_e} < 3{,}000$ and $\mathrm{Re} < 2{,}000$, then $w_e = 0$.

Case I entrainment (upper layer turbulent)
Input: u_* = shear stress at water surface

bulk Richardson number

$$Ri_* = \frac{(\rho_b - \rho_w)\, gh}{\rho_w u_*^2} \tag{5}$$

if $\mathrm{Ri}_* < 1{,}000$ then

$$w_e = u_* \left(\frac{2c_s}{c_q + \mathrm{Ri}_*} \right)^{1/2} \tag{6}$$

if $\mathrm{Ri}_* > 1{,}000$ then

$$w_e = u_* \frac{c_\sigma}{\mathrm{Ri}_*} \tag{7}$$

Output: $w_e = \mathrm{d}\delta/\mathrm{d}t$ = initial entrainment velocity of fluid mud layer (layer becomes thinner). Note that at larger Richardson numbers (strong stratification) the entrainment process virtually ceases (strong damping of turbulence) and only "stirring", described by equ. (7) remains.

Case II entrainment (lower layer turbulent)
Input: u_* = shear stress at consolidated bed

bulk Richardson number

$$Ri_* = \frac{(\rho_b - \rho_w)\, g\delta}{\rho_b u_*^2} \tag{8}$$

if $\mathrm{Ri}_* < 1{,}000$ then

$$w_e = u_* \left(\frac{2c_s}{c_q + \mathrm{Ri}_*} \right)^{1/2} \tag{9}$$

if $\mathrm{Ri}_* > 1{,}000$ then

$$w_e = u_* \frac{c_\sigma}{\mathrm{Ri}_*} \tag{10}$$

Output: $w_e = \mathrm{d}\delta/\mathrm{d}t$ = initial entrainment velocity of fluid mud layer (layer becomes thicker). Note that at larger Richardson numbers (strong stratification) the entrainment process virtually ceases (strong damping of turbulence) and only "stirring", described by equ. (10) remains.

Limitation of application
This algorithm is applicable when either the water layer or the fluid mud layer is turbulent, or if the turbulence level of either one of these layers is much larger than the other. In case both layers are more or less equally turbulent, vertical mixing, possibly affected by buoyancy effects, becomes the dominant mechanism.

This algorithm describes the initial entrainment rates.

- Case I formula may also be applied as a first approximation to model erosion of the entire fluid mud layer.
- Case II formula can be applied as long as the fluid mud layer remains thin with respect to the water depth: $\delta/h < 0.2$.

Validation
The model is validated against laboratory data – see below.

2.8.1.1 Entrainment of fluid mud layers

Entrainment is a process that occurs in systems with two layers of fluid, and is referred to when a turbulent layer erodes a second non-turbulent (or less turbulent) layer, e.g. Turner (1973). Scarlatos and Mehta (1990), Mehta and Srinivas (1993) and Winterwerp and Kranenburg (1997a) showed that soft mud layers may behave as a viscous fluid, in which case they may be subject to entrainment processes.

Kranenburg and Winterwerp (1997) derived equations for entrainment at two conditions (see also Bruens, 2003):

Case I: Entrainment of a fluid mud layer by the turbulent water layer above,
Case II: Entrainment by a turbulent fluid mud layer of the water layer above.

This is further depicted in Figure 1, which also contains the various definitions used in the derivation of the entrainment equation. For Case I, the upper turbulent layer erodes the lower mud layer, and the sediment-water interface lowers: the sediment concentration in the lower mud layer remains constant, and the concentration in the upper layer slowly increases. Case I conditions occur for instance when wind-induced surface shear stresses generate entrainment, in the case of the entrainment of patches of fluid mud in local depressions (navigation channels) by turbulent ambient water, and in many laboratory experiments.

For Case II, the lower turbulent mud layer entrains water (or low-concentration suspension) from the upper layer, and the sediment-water interface rises: the sediment concentration in the lower layer decreases, and it remains constant in the upper layer. Case II conditions occur for instance in the case flowing mud layers, either in a river channel (Loire, e.g. Le Hir, 1997) or on slopes, and in the case of sub-marine turbidity currents.

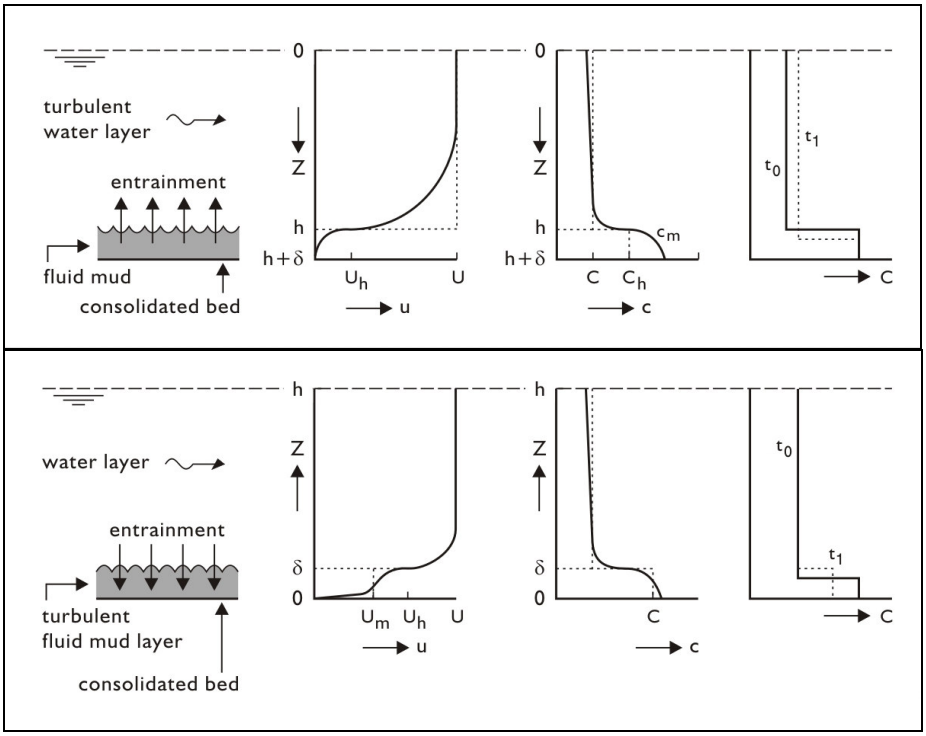

Figure 1 Case I (upper panel: upper layer turbulent) and Case II (lower panel: lower layer turbulent) entrainment

The entrainment equation is obtained by integrating the 1DV momentum equation, sediment balance equation and turbulent kinetic energy equation (TKE) over the thickness of the turbulent layer h (upper layer water depth, Case I) or δ (lower layer mud thickness, Case II), using the equation of state. We have added the effects of side-wall friction to enable the analysis of laboratory flume experiments, and the effects of a yield strength τ_y of the mud layer is introduced by relating the various shear velocities to a "yield velocity" $u_y^2 = \tau_y / \rho_b$. Integration of the TKE-equation yields:

$$\frac{\mathrm{d}}{\mathrm{d}t}\int_0^h k\mathrm{d}z + \int_0^h \left(\overline{u'w'}\frac{\partial u}{\partial z}\right)\mathrm{d}z - \frac{2\lambda}{W}hU^3 - \alpha\frac{g}{\rho_0}\int_0^h \overline{w'c'}\mathrm{d}z + \int_0^h \varepsilon\ \mathrm{d}z = 0 \qquad (1)$$

in which u and w are the horizontal and vertical flow velocity, c is the suspended sediment concentration, a prime denotes turbulent fluctuations and an overbar averaging over the turbulent time scale. The entrainment equation for Case I becomes:

$$\begin{aligned} &c_q\frac{\mathrm{d}}{\mathrm{d}t}\left(hU\frac{\mathrm{d}h}{\mathrm{d}t}\right) - c_s\left[2\left\langle u_h^2 - u_y^2\right\rangle(U-U_\delta) + \left((U-U_h)^2 - c_y u_y^2\right)\frac{\mathrm{d}h}{\mathrm{d}t}\right] + \\ &+c_s'\left\langle u_*^2 - u_y^2\right\rangle(U-U_h) - c_\sigma\left\langle u_s^2 - u_y^2\right\rangle u_s + \\ &-2c_w\frac{h}{W}\left\langle u_w^2 - u_y^2\right\rangle U + B\frac{\mathrm{d}h}{\mathrm{d}t} + 2\frac{\alpha C}{\rho_0}gw_s h = 0 \qquad \text{for} \quad \frac{\mathrm{d}h}{\mathrm{d}t} > 0 \end{aligned} \qquad (2)$$

in which U is depth-mean velocity of turbulent layer, w_s is the sediment settling velocity, α is the fractional density difference ($\alpha = (\rho_s - \rho_w)/\rho_s$), W is width of flume (laboratory experiments), B is the total buoyancy, i.e. $B = \alpha g h\left(c_h - C\right)/\rho_0$, and the terms between angular brackets become zero when negative. The various coefficients were established as: $c_q = 5.6$; $c_s = c_s' = 0.25$; $c_\sigma = 0.42$; $c_w = 0.07$. The term u_s^3 is the so-called stirring term, which becomes important when viscous effects play a role (i.e. large Ri_*): $u_s^3 = u_*^3 + u_\delta^3 + 2hu_w^3/W$, with $u_w^2 = \lambda U^2$; λ is friction coefficient. U_h is the velocity of the upper layer at the water – fluid mud interface and u_h is the velocity of the lower layer at the water – fluid mud interface.

In the case of no viscous effects ($u_h = U_h = 0$), thus no stirring ($u_s = 0$), as in the case of small Richardson numbers, the equilibrium solution (i.e. at large time when $U\,\mathrm{d}H/\mathrm{d}t \approx u_*^2$) to (2) yields an explicit expression for the initial entrainment velocity w_e, hence entrainment rate E_* (e.g. Kranenburg and Winterwerp, 1997):

$$E_* = \frac{1}{u_*}\frac{\mathrm{d}h}{\mathrm{d}t} = \frac{w_e}{u_*} = \left(\frac{2c_s}{c_q + Ri_*}\right)^{1/2} \tag{3}$$

where we have defined $Ri_* = B/u_*^2 = \left(\rho_b - \rho_0\right)gh_0/\rho_0 u_*^2$, which is the bulk Richardson number. Note that shear is generated at the water surface (Case I).

This entrainment equation differs both in their coefficients and exponent from the one used by Odd and Cooper (1989) to describe the large scale behaviour of (fluid) mud in the Severn estuary.

At large Ri_* viscous effects, hence the stirring term u_s becomes important, and (2) becomes:

$$E_* = \frac{1}{u_*}\frac{\mathrm{d}h}{\mathrm{d}t} = \frac{w_e}{u_*} = c_\sigma \frac{u_s^3/u_*}{B} \approx \frac{c_\sigma}{Ri_*} \tag{4}$$

where u_* is measured at the water-mud interface.

In flumes with side-wall friction, the equilibrium solution to (2) at large Richardson numbers reads (using the equilibrium solution to the momentum equation as well, e.g. Winterwerp and Kranenburg, 1997b):

$$\frac{1}{u_*}\frac{\mathrm{d}h}{\mathrm{d}t} = \frac{w_e}{u_*} = \frac{c_w}{\left(2\lambda h/W\right)\left(c_q + Ri_*\right)} \tag{5}$$

Note that the effects of large Ri_* and side-wall friction explain the apparent inconsistencies in literature between $w_e \propto Ri_*$ or $w_e \propto \sqrt{Ri_*}$.

For Case II we give the results without derivation as this is straightforward:

$$c_q \frac{\mathrm{d}}{\mathrm{d}t}\left(\delta U_m \frac{\mathrm{d}\delta}{\mathrm{d}t}\right) - c_s\left[2\left\langle u_h^2 - u_y^2\right\rangle (U_\delta - U_m) + \left((U_h - U_m)^2 - c_y u_y^2\right)\frac{\mathrm{d}\delta}{\mathrm{d}t}\right] +$$
$$+ c_s'\left\langle u_*^2 - u_y^2\right\rangle (U_h - U_m) - c_\sigma\left\langle u_s^2 - u_y^2\right\rangle u_s + \qquad (6)$$
$$-2c_w \frac{\delta}{W}\left\langle u_w^2 - u_y^2\right\rangle U_m + B\frac{\mathrm{d}\delta}{\mathrm{d}t} + 2\frac{\alpha C}{\rho_0} g w_s \delta = 0 \qquad \text{for} \quad \frac{\mathrm{d}\delta}{\mathrm{d}t} > 0$$

Entrainment equation (6) yields the same asymptotic solutions as (2), i.e. equ.'s (3) and (5), but h replaced by δ, and u_* is now related to the bed shear stress (equ. (4) remains unaltered).

The entrainment model for Case I (equ. 2) was used to re-analyse the entrainment experiments on stable fresh-saline water two-layer systems by Kantha et al. (1977), as presented in Figure 2. It is shown that (2) predicts the observations properly, including the change in E_* vs Ri_* slope. This change in character with increasing Ri_* is fully explained by the effects of viscosity and side-wall friction. Details of this analysis are given in Winterwerp and Kranenburg (1997b).

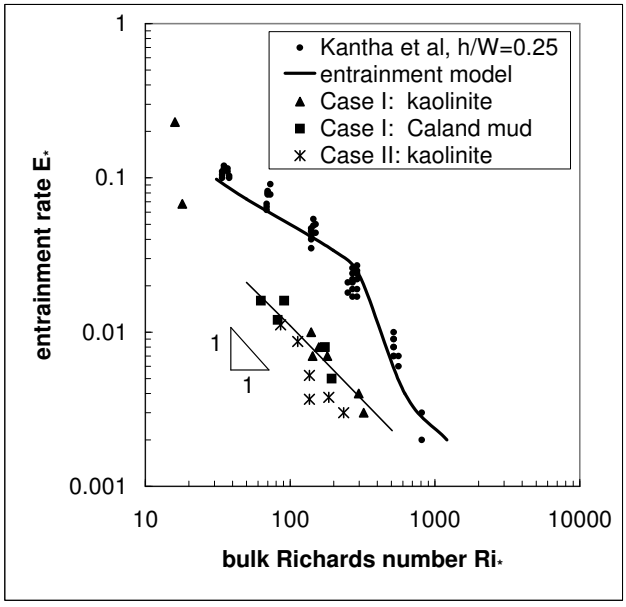

Figure 2 Initial measured and predicted (equ. 2) entrainment rates as function of bulk Richardson (after Winterwerp and Kranenburg, 1997b and Bruens, 2003)

We have also plotted the initial entrainment rates for Case I entrainment measured by Winterwerp and Kranenburg (1997b) and for Case II entrainment measured by Bruens (2003). These measurements were carried out in a rotating annular flume with kaolinite and mud from the Caland Canal (entrance channel to Rotterdam Port). It is shown that these entrainment rates agree quite well, in spite of their difference in nature, and follow the $w_e \propto Ri_*$ law, indicating that viscous effects and side-wall friction were important in these experiments.

Winterwerp and Kranenburg (1997a) and Bruens (2003) showed that the entrainment behaviour of fluid mud-water systems and salt-fresh water systems behave identically. This implies that fluid mud layers behave as viscous fluids, at least during part of their existence. This was also observed by Scarlatos and Mehta (1990) and Mehta and Srinivas (1993).

The effects of yield stress on the entrainment behaviour are illustrated in Figure 3, showing the decay in entrainment rate with time; OSLIM is optical silt monitoring instrument. The experiment against which the entrainment model was compared, was also carried out in a rotating annular flume with mud from the Caland Canal. Results of other, similar experiments are given in Winterwerp and Kranenburg (1997b), including the results of a "tidal" experiment, during which the applied shear stress was varied sinusoidally with time.

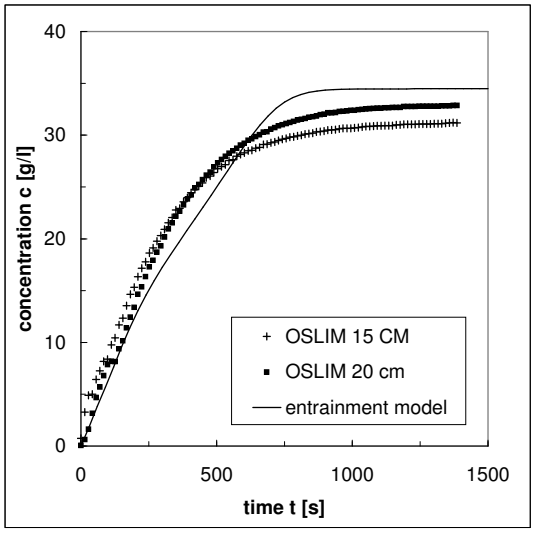

Figure 3 Time-variation of suspended sediment concentration above fluid mud layer as a result of entrainment of that layer (after Winterwerp and Kranenburg, 1997b)

This entrainment model has been applied for instance in a numerical modelling study on the far field dispersion of fine grained sediments mobilised by Water Injection in the River Crouch, UK (Winterwerp et al., 2002). The results of the simulations compared favourably with measurements on the dispersion of labelled sediment.

References

Bruens, A.W., 2003, Entraining mud suspensions, PhD-thesis, Delft University of Technology, also Communications on Hydraulic and Geotechnical Engineering, Faculty of Civil Engineering, Delft University of Technology, Report 03-01, ISSN 0169-6548.

Kantha, L.H., O.M. Philips and R.S. Azad, 1977, On turbulent entrainment at a stable density interface, Journal of Fluid Mechanics, 79 (4) 753-768.

Kranenburg, C. and J.C. Winterwerp, 1997, Erosion of fluid mud layers – I: Entrainment model, ASCE, Journal of Hydraulic Engineering, 123 (6) 504-511.

Le Hir, P., Fluid and sediment “integrated” modelling application to fluid mud flows in estuaries, in: N. Burt, R. Parker and J. Watts, Cohesive Sediments, John Wiley & Sons, Chichester, 417-428.

Mehta, A.J. and R. Srinivas, 1993, Observations on the entrainment of fluid mud by shear flow, in: A.J. Mehta, Coastal and Estuarine Studies, American Geophysical Union, 42, 224-246.

Odd, N.V.M and A.J. Cooper, 1989, A two-dimensional model of the movement of fluid mud in a high energy turbid estuary, Journal of Coastal Research, Special Issue No 5, 185-194.

Scarlatos, P.D. and A.J. Mehta, 1990, Some observations on erosion and entrainment of estuarine fluid muds, in: R.T. Cheng (ed.), Residual Currents and Long-term transport, Springer-Verlag, Coastal and Estuarine Studies, 38, 321-332.

Turner, J.S., 1973, Buoyancy effects in fluids, Cambridge University Press.

Winterwerp, J.C. and C. Kranenburg, 1997a, Erosion of fluid mud by entrainment, in: N. Burt, R. Parker and J. Watts, Cohesive Sediments, John Wiley & Sons, Chichester, 263-278.

Winterwerp, J.C. and C. Kranenburg, 1997b, Erosion of fluid mud layers – II: Experiments and model validation, ASCE, Journal of Hydraulic Engineering, 123 (6) 512-519.

Winterwerp, J.C., Z.B. Wang, J.A.Th.M. van Kester and J.F. Verweij, On the far-field impact of Water Injection Dredging, ICE/IAHR, Water and Maritime Engineering, 154 (4) 285-296.

2.8.2 EP21 - Algorithm for Gravitational circulation (WLD – Winterwerp)

Aim To describe and implement a method for including gravitational circulation in depth-averaged computational hydrodynamic models.

Background
Fresh water outflow in estuaries and lagoons generates horizontal density gradients resulting in a vertical circulation with a net landward near-bed current (gravitational circulation). As the near-bed sediment concentration tends to be larger than the concentration higher in the water column, gravitational circulation causes a net landwards sediment transport.

Gravitational circulation is often related to the formation and location of the turbidity maximum in estuaries, as sediment transport converges near the head of the salinity intrusion.

When the salinity structure is stratified, the landward transport will increase. This mechanism plays a role mainly in (deeper) channels of estuaries and tidal inlets, and is stronger for fine sediment with a larger grain size, as this sediment depicts a more pronounced vertical concentration gradient.

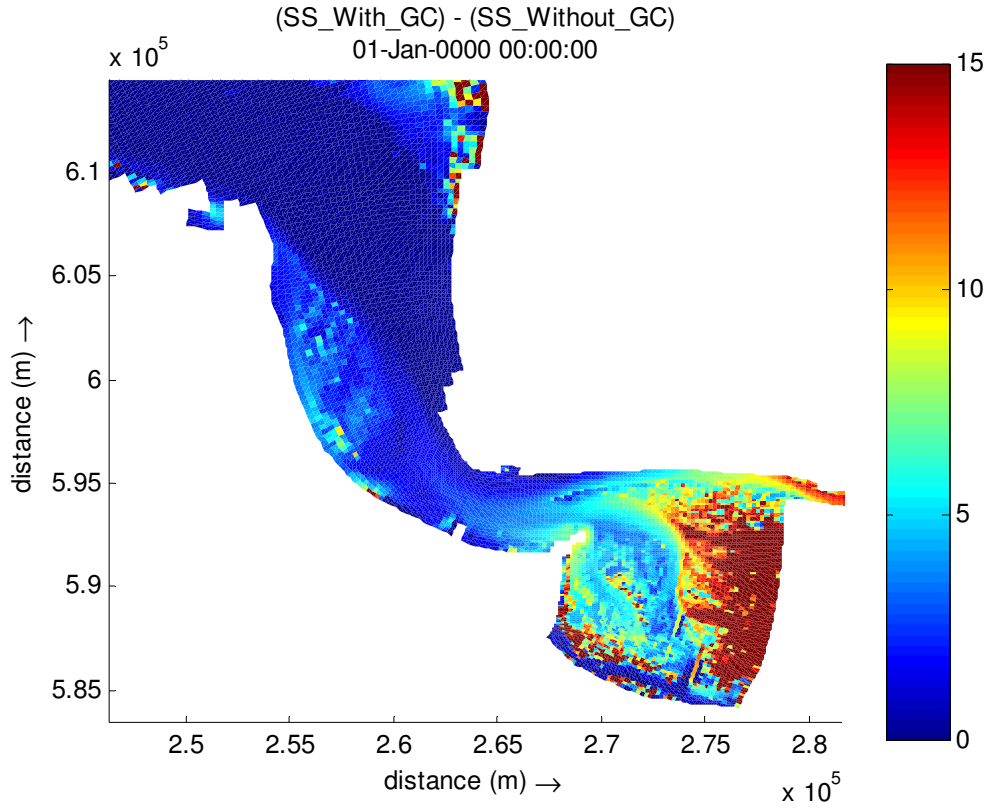

Figure 1 Absolute difference between computed 2Dh suspended sediment concentration in Dollart estuary with and without parameterisation of gravitational circulation

Method

The effects of gravitational circulation is not accounted for in depth-averaged (2Dh) sediment transport models, as all information on the vertical structure of the flow is lost. However, these effects can be included through parameterisation, using the horizontal (depth-averaged) salinity field, calibrated against observations by tuning the horizontal dispersion coefficient for salt D_S. The basic idea is to modify the advection term of the momentum equation for fine sediment with the computed salinity field, as gravitational circulation is an advective process. The transport of salt water T_s is described with an advective and diffusive part:

$$\vec{T}_s = h\vec{U}S - hD_S\,\partial S/\partial\vec{x} \tag{1}$$

where h is water depth, U is flow velocity vector, S is salinity and D_S is the dispersion coefficient for salt water transport, which is the calibration parameter to obtain a proper salinity distribution, given a properly calibrated water movement. The transport of fine sediment T_c, where c is the suspended sediment concentration, then consists of an advective part, normalised by the depth-mean salinity, given by T_s and a diffusive part:

$$\vec{T}_c = \vec{T}_S\frac{c}{S} - hD_c\frac{\partial c}{\partial\vec{x}} = hc\left(\vec{U} - \alpha\frac{D_S}{S}\frac{\partial S}{\partial\vec{x}}\right) - hD_c\frac{\partial c}{\partial\vec{x}} \tag{2}$$

where we have added the coefficient α to accommodate for possible non-linear effects. Note that in general $D_S >> D_c$, where D_c is the dispersion coefficient for suspended sediment.

Figure 1 shows the effect of this parameterisation on the computed depth-averaged suspended sediment concentration in the Dollart estuary, The Netherlands.

2.8.3 EP22 – Algorithm for transport by sediment-induced density currents (WLD – Winterwerp)

Aim To describe and implement a method for including sediment-induced density currents in a 3-dimensional computational hydrodynamic model.

Background
Suspensions of fine-grained sediment behave as a single phase fluid with densities in excess of those of clear water. Buoyancy effects may therefore become important, and it was shown (Winterwerp, 2001) that this may occur already at moderate concentrations, depending on the (local) hydrodynamic conditions. When the sediment concentrations become too large, the turbulence field may collapse and the flow can no longer keep the sediment in suspension. This condition is referred to as saturation. At, or just prior to saturation, the flow carries the maximum possible amount of sediment, known as the flow's capacity condition.

It is illustrative to compare the behaviour of a suspension in equilibrium at capacity condition of cohesive and non-cohesive sediment in uniform open channel flow in response to a (small) decrease in velocity:

- At capacity conditions, the vertical concentration profile of suspended non-cohesive sediment (sand) is at equilibrium with the local hydrodynamics. When the flow velocity is decreased, part of the sediment will settle until the sediment load is again in equilibrium with the new hydrodynamic conditions. Upon sedimentation, the settling particles form a rigid bed immediately, at which turbulence production is possible.
- Under the same conditions, settling flocs of cohesive sediment do not form a rigid bed but a layer of fluid mud instead, because of the high water content (large volumetric concentration) of the flocs. At the interface of the fluid mud layer relatively large gradients in suspended sediment concentration, hence fluid density occur, as a result of which turbulence mixing is damped. Because of this damping, less sediment can be kept in suspension, and a snowball effect results upon which finally no sediment at all can be kept in suspension.

It is noted that in natural environments additional sources of turbulence exist, generated locally or advected from elsewhere; such sources comprise bed irregularities, river banks, secondary currents, etc. Therefore, complete saturation may not be observed, even if the (local) conditions would be favourable.

Method
Prior to or without saturation, sediment-induced density effects can significantly influence large scale sediment transport rates. This is substantiated with simulations of the sediment transport into the Maasmond area, i.e. the approach channel to the Port of Rotterdam. These simulations have been carried out with a three-dimensional numerical model, based on DELFT3D, in which the following four processes have been implemented:

1. adjustment of the equation of state to account for the effects of suspended sediment concentration on the fluid density:

$$\rho\left(S,T,c^{(i)}\right)=\rho_w(S,T)+\sum_i\left\{\left(1-\frac{\rho_w(S,T)}{\rho_s^{(i)}}\right)c^{(i)}\right\} \tag{1}$$

2. a buoyancy destruction term in the k-ε turbulence closure equation to account for sediment-induced turbulence damping:

$$\frac{\partial k}{\partial t}+\frac{\partial u_i k}{\partial x_i}-\frac{\partial}{\partial x_i}\left(\nu+\frac{\nu_T}{\sigma_k}\right)\frac{\partial k}{\partial x_i}= \tag{2a}$$
$$=\nu_T\left(\frac{\partial u_i}{\partial x_j}+\frac{\partial u_j}{\partial x_i}\right)\frac{\partial u_i}{\partial x_j}+\delta_{i3}\frac{g}{\rho}\frac{\nu_T}{\sigma_T}\frac{\partial \rho}{\partial x_i}-\varepsilon$$

$$\frac{\partial \varepsilon}{\partial t}+\frac{\partial u_i \varepsilon}{\partial x_i}-\frac{\partial}{\partial x_i}\left(\nu+\frac{\nu_T}{\sigma_\varepsilon}\right)\frac{\partial \varepsilon}{\partial x_i}= \tag{2b}$$
$$=c_{1\varepsilon}\nu_T\frac{\varepsilon}{k}\left(\frac{\partial u_i}{\partial x_j}+\frac{\partial u_j}{\partial x_i}\right)\frac{\partial u_i}{\partial x_j}+\delta_{i3}\left(1-c_{3\varepsilon}\right)\frac{\varepsilon}{k}\frac{g}{\rho}\frac{\nu_T}{\sigma_T}\frac{\partial \rho}{\partial x_i}-c_{2\varepsilon}\frac{\varepsilon^2}{k}$$

3. a hindered settling formula to account for the formation of steep vertical density gradients:

$$W_s=W_{s,0}\left(1-\frac{c}{c_{gel}}\right)^5 \quad \text{or} \quad W_s=W_{s,0}\frac{\left(1-c/c_{gel}\right)\left(1-c/\rho_s\right)}{1+2.5\,c/c_{gel}} \tag{3}$$

4. and a baroclinic pressure term in the momentum equations to account for horizontal pressure gradients as a result of horizontal concentration gradients:

$$\frac{\mathrm{D}u_i}{\mathrm{D}t}=-\frac{1}{\rho_0}\frac{\partial}{\partial x_i}\int_z^\zeta g\rho dz'+\frac{1}{\rho_0}\frac{\partial \sigma_{ij}}{\partial x_j}-e_{ij}fu_j \tag{4}$$
$$\frac{\partial p}{\partial x_3}=-g\rho$$

where x_i = spatial co-ordinate, t = time, g = gravitational acceleration, u_i = flow velocity, p = pressure, σ_{ij} = stress tensor, S = salinity, T = temperature, c = suspended sediment concentration, c_{gel} = gelling concentration (fluid mud concentration), ρ = fluid density, ρ_s = sediment density, k = turbulent kinetic energy, ε = dissipation rate per unit mass, W_s = settling velocity, $W_{s,0}$ = reference settling velocity, ν = diffusion coefficient, ν_T = eddy diffusivity, $\sigma_{\varepsilon T}$ = turbulent Prandtl-Schmidt number, f = Coriolis.

From a sensitivity analysis it appeared that inclusion of the baroclinic pressure gradients did not have a very large effect.

Application

The computations were carried out with and without sediment-fluid interaction (i.e. sediment-induced buoyancy effects in the turbulence model, hindered settling and barotropic pressure effects in the momentum equations), e.g. Winterwerp and Van Kessel (2003) for details. Results of tide-averaged suspended sediment concentrations in the lower layer of the computational grid are presented in Figure 1.

The large differences in suspended sediment concentration result in large differences in computed sediment fluxes (hence siltation rates) in the Maasmond area, as depicted in Table 1. The cross sections at which these fluxes have been computed are indicated in Figure 1. Table 1 shows that the net flux over a tidal cycle through cross section 1, Maasmond mouth, almost triples. This is the result of an increase in both the gross import and gross export, though the effect on the import is the larger of the two. The major differences between the two simulations are found near the bed: in the case of inclusion of sediment-fluid interaction, the concentration profile becomes highly stratified, forming a layer of fluid mud in the harbour basins. It is expected that if non-Newtonian effects in and/or consolidation of the fluid mud layers were accounted for, the difference between the two simulations would become even be larger as gross sediment export would decrease further.

These computations have been performed with an inflow suspended sediment concentration of 100 mg/l at the model boundaries. This is a characteristic value in the Dutch coastal zone in the North Sea for mild winter conditions. For typical summer conditions, with a boundary concentration of 10 to 50 mg/l, the effect of sediment-fluid interaction on the sediment fluxes is 10 % only. As the sediment-fluid interactions are highly non-linear, it may be expected that the increase in sediment flux would increase rapidly (by an order of magnitude) when the suspended sediment concentration at sea increases to several 100 mg/l, typical values in the Dutch coastal zone under storm conditions.

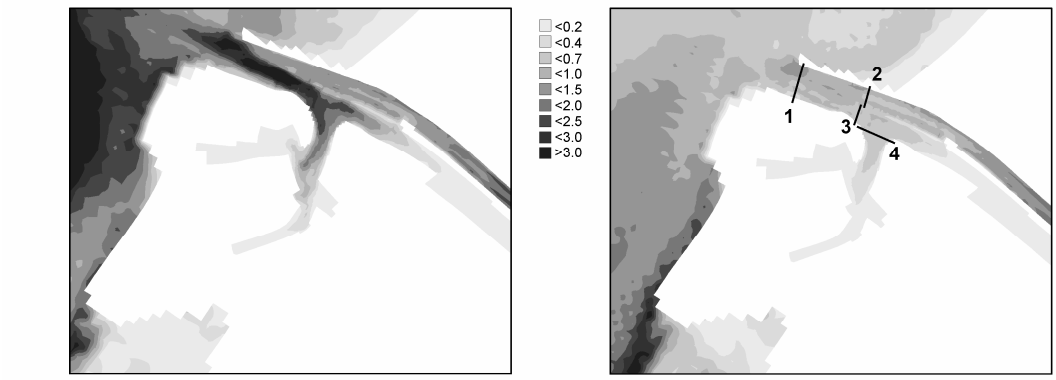

Figure 1 Sediment concentration [g/l] near the bed computed with (left panel) and without (right panel) sediment-fluid interactions. The transect lines refer to Table 1

Conclusions

In summary, we conclude that sediment-driven density currents resulting from highly non-linear sediment-fluid interaction may significantly affect the net sediment fluxes, hence siltation rates, in navigational channels and harbour basins. These density currents generate and feed the fluid mud layers observed in many basins throughout the world.

Under extreme conditions, siltation rates can be expected to become at least an order of magnitude larger than predicted with models that do not account for such sediment-fluid interactions.

Table 1 Water and sediment fluxes for Rotterdam harbour area; see Figure 1 for definition cross sections

		sediment flux [kg/s]			water flux [m^3/s]		
interact.	cross section	Tidal net	Gross import	Gross export	Tidal net	max. ebb	max. flood
yes	1. Maasmond	884	1503	-620	-1,264	-12,929	10,575
yes	2. R'dam Waterway	76	466	-390	-1,304	-9,067	5,490
yes	3. Calandkanaal	792	828	-35	0	-3,457	5,470
yes	4. Beerkanaal	-404	8.0	-413	0	-2,119	1,481
no	1. Maasmond	325	719	-395	-1,263	-12,886	10,298
no	2. R'dam Waterway	50	365	-315	-1,292	-8,959	5,476
no	3. Calandkanaal	263	307	-44	0	-3,518	5,452
no	4. Beerkanaal	-126	4.8	-131	0	-2,095	1,505

References

J.C. Winterwerp, 2001, Stratification effects by cohesive and non-cohesive sediment, Journal of Geophysical Research, Vol 106, No C10, pp 22559-22574.

J.C. Winterwerp and T. van Kessel, 2003, Siltation by sediment-induced density currents, Ocean Dynamics, Vol 53, pp 186-196.

2.8.4 EP23 - Algorithm for Stress History (Exposure Correction) on sand sediment threshold (SOES- Paphitis)

Aim To complete by laboratory testing data collection on the influence of exposure of sandy sediments to pre-threshold of sediment motion levels of flow and derive an algorithm to make predictions of the "exposure correction".

Background
The results of the stress history investigations, where the 'increase factors' in the critical shear velocity are plotted against the duration under which the sediment bed was exposed to the investigated pre-threshold velocities, are presented in Figure 1.

Algorithm
Utilising all the data an empirical formula for the calculation of the exposure correction factor (u_{*cc}/u_{*c}, where u_{*cc} is the corrected critical shear velocity) in the critical shear velocity is derived that includes the duration of exposure (E_D) and the percentage of pre-threshold velocity (u_*/u_{*c}) as explicit variables. Plotted on Figure 1 are the empirical curves (calculated using Eq. 1) for the pre-threshold velocity conditions investigated; the correlation coefficients of these curves were found to be over 0.83, with p-values of <0.001 at the 95% level of significance.

$$\frac{u_{*cc}}{u_{*c}} = 1.05\left(1 - 0.01e^{(-0.005E_D)}\right) + \left(0.005 + \left(\frac{u_*}{u_{*c}} - 0.7\right)0.1\right)\ln\left(E_D\right) + 0.06\left(10^{-7(0.97-\frac{u_*}{u_{*c}})}\right) \quad (1)$$

$$\text{for} \quad 0.70 \le \frac{u_*}{u_{*c}} \le 0.95 \quad \text{and} \quad E_D \le 120\,\text{min}$$

This formula can be used readily in practical applications, where the sediment bed under investigation has been exposed (for a known duration) to pre-threshold unidirectional currents.

Conclusion
The application of the proposed formulae will provide practitioners with an exposure correction factor (i.e. the critical shear velocity 'increase factor'), which needs to be applied to the critical shear velocity. This can be done prior to their inclusion in bedload transport formulae.

Validity
The formula is restricted to the conditions under which it has been derived i.e. sand-sized sediments, pre-threshold velocity ranging from 70% to 95% and for duration of exposure less than 120min. The sand grain sizes tested were 0.194 mm, 0.387 mm and 0.774 mm.

More information is presented in the paper by Paphitis and Collins (2005).

Reference
Paphitis, D. and Collins, M.B. 2005. Sand grain threshold, in relation to bed 'stress history': an experimental study. Sedimentology, 52, 827-838.

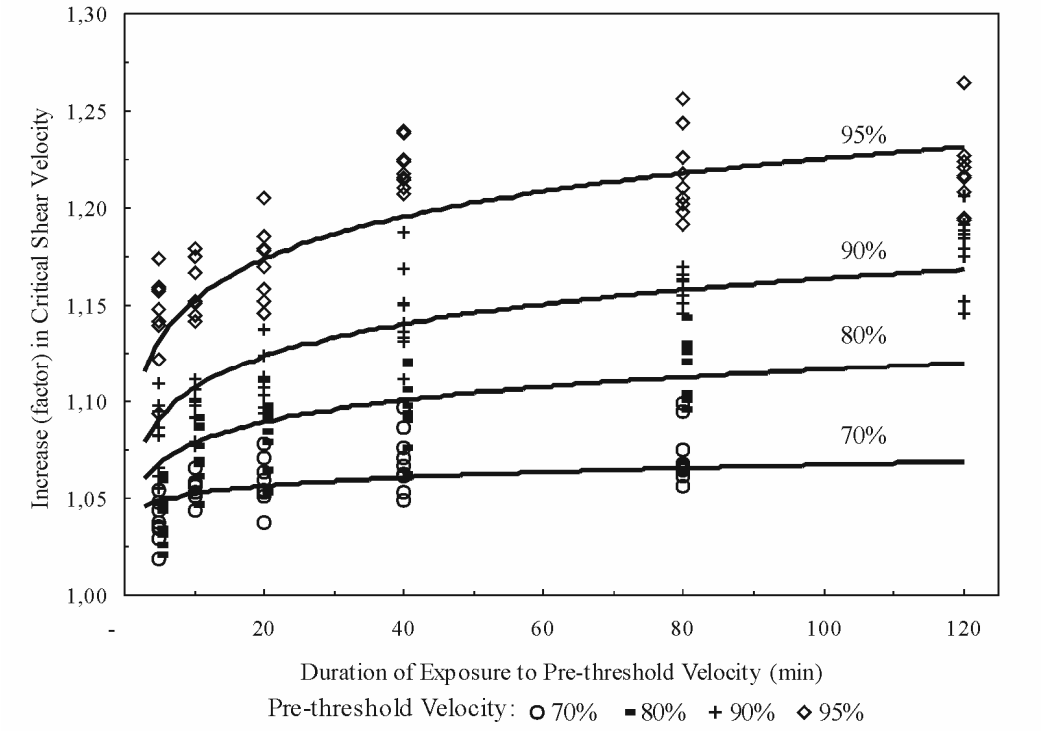

Figure 1 Threshold velocity increase factors plotted against the exposure duration to pre-threshold velocities. The series of curves were defined using Eq. 1 and they represent the different pre-threshold velocities investigated

2.8.5 EP24 - Algorithm for day-night stability of sandy sediment (SOES – Friend)

Aim This algorithm assesses day/night variations in sediment stability associated with erosion threshold, for sandy intertidal flats based on site measurements.

Method
Sediment stability measurements were made using a Cohesive Strength Meter (CSM) at a sandy intertidal flat station in southern England, over six consecutive day-night emersion periods during a period of relatively high microalgal biomass (mean: 4.4 μg gDW^{-1}) in the spring (Figure 1). Mean grain size was 150 μm (fine sand). The general procedure outlined by Tolhurst et al. (1999) was used for processing the CSM data. The index of biological stabilisation, based upon the ratio of the biotic to abiotic critical threshold of sediment motion was calculated using the algorithm for the objective definition of a biostabilisation index for sandy intertidal flats using the Cohesive Strength Meter (CSM).

Result
Coefficients of biostabilisation for night-time emersion periods (average 16.7) were significantly higher (paired t-test: $p = 0.011$) than day-time coefficients (average 10.5). This means the sandy sediments were more stable at night than during the day.

Applicability
This result applies to sandy intertidal sediments, similar work has been published for muddy intertidal sediments (Friend et al, 2005). The work for muddy sediments showed that sediments were more stable during the day than at night.

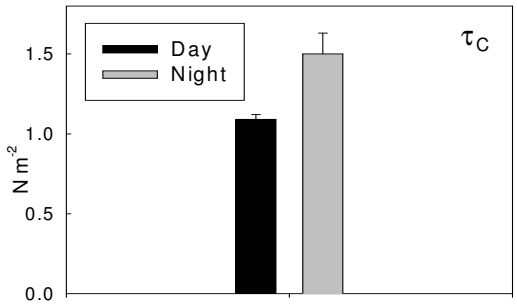

Figure 1 Mean critical erosion thresholds over six consecutive day-night emersion periods on a sandy intertidal flat in southern England

Reference
Friend, P.L., Lucas, C.H. and Rossington, K. (2005). Day-night variation of cohesive sediment stability. Estuarine, Coastal and Shelf Science, 64, 407-418.

Tolhurst, T.J., Black, K.S., Shayler, S.A., Mather, S., Black, I., Baker, K., and Paterson, D.M. (1999). Measuring the *in situ* Erosion Shear Stress of Intertidal Sediments with the Cohesive Strength Meter (CSM). *Estuarine, Shelf and Coastal Science* 49: 281-294.

2.8.6 EP25 - Algorithm for selecting Bed Update strategies in estuary models (WLD – Roelvink)

Aim To compare different bed updating strategies in a simple but realistic test case.

Scientific background
In Roelvink (2004) five methods of morphodynamic updating were discussed:

- 'Brute force' where the bed is updated during every transport step
- 'Tide averaging' where transport is averaged over tide before taking a bottom step
- 'Tide averaging with continuity correction', same as above but with intermediate steps where intra-tidal transport is recomputed based on a simple adjustment of velocities
- 'RAM' where tide-averaged transport is recomputed after each bottom step based on a very simple adjustment rule
- 'Morphological factor' where the bed updating takes place every timestep but is multiplied by the morphological factor.

Applying various methods on real-life test problems is very time-consuming and not always possible, as not all methods are usually available in a single model system. Therefore a simple test problem has been devised to compare the methods in principle.

Improvement in understanding
The test problem clarifies the effects of the various schemes and their problem areas.

Implementation
Let us consider a tidal channel that is gradually widening over a typical length scale *L*. The flow diverges during flood (positive direction) and converges during ebb tide. A mean discharge is added. The transport gradient can then be approximated by the transport itself divided by a length scale *L*, so:

$$\frac{\partial z_b}{\partial t} = -\frac{\partial S_x}{\partial x} \approx -\frac{S_x}{L} \tag{1.1}$$

Let us now assume that the discharge per unit width through the channel has a mean component $\overline{q}$ and an oscillatory component at the M2 frequency, $\tilde{q}$. This discharge is not sensitive to the depth *h*, until the depth becomes so shallow that the flow chooses another channel and the discharge goes to zero. This effect is added by means of a smooth tapering function; the discharge including all effects is now described by:

$$q = \left(\overline{q} + \tilde{q}\cos(\omega t)\right)\left(1 - \exp\left(-\left(\frac{h}{h_{sh}}\right)^2\right)\right) \tag{1.2}$$

where h_{sh} is a depth scale that governs the tapering of the discharge to zero. We assume that the transport rate S_x is a simple function of the velocity and thus:

$$S_x = a\left(|u|\right)^{b-1} u = a\left(\left|\frac{q}{h}\right|\right)^{b-1} \frac{q}{h} \tag{1.3}$$

where u is the flow velocity (= q/h), b is the power in the transport formulation and a the transport scaling coefficient.

With this simple set of formulas we can now test the various time integration schemes. We can do this by integrating equation (1.1) numerically for each of the schemes. The outline of the algorithms used for each scheme are shown below:

Brute force method (N=1) and morphological factor (N>1)

Given:

- *Initial depth h*
- *Number of time steps Nt*
- *Time step dt*
- *Tidal period*
- *Morphological factor N*

For timesteps 1 to Nt/N
Compute discharge using (1.2)
Compute velocity from q/h
Compute transport Sx according to (1.3), multiplied by N
Compute transport gradient according to (1.1)
Compute new bed level and water depth by means of Euler scheme
End loop

Tide-averaging with continuity correction

Given:

- *Initial depth h*
- *Number of time steps within tide Nttide*
- *Number of continuity correction steps Ncont*
- *Number of morphological steps Nmorf*
- *Time step dt*
- *Tidal period*

For morphologcial steps 1 to Nmorf
For time steps 1 to Nttide
Compute and store discharge rates
End full tide loop
For Continuity Correction steps 1 to Ncont
For time steps 1 to Nttide
Compute velocity from q/h
Compute transport Sx according to (1.3),
End simplified tide loop
Average transport Sx
Compute transport gradient according to (1.1)
Compute new bed level and water depth by means of Euler scheme
End loop continuity correction
End morphological loop

Tide-averaging with RAM

Given:

- *Initial depth h*
- *Number of time steps within tide Nttide*
- *Number of intermediate RAM steps*
- *Number of morphological steps Nmorf*
- *Time step dt*
- *Tidal period*

For morphological steps 1 to Nmorf

For time steps 1 to Nttide
Compute and store discharge rates
Compute velocity from q/h
Compute transport Sx according to (1.3),
End full tide loop
Average transport Sx
Compute coefficients a and b
For RAM steps 1 to Nram
*Compute transport according to simplified relation Sx=a*h^(-b)*
Compute transport gradient according to (1.1)
Compute new bed level and water depth by means of Euler scheme
End loop RAM
End morphological loop

Limits of applicability
This method is meant to demonstrate principles, not for direct application.

Validation
All methods converge to very similar solutions for small morphological factors, number of intermediate continuity correction steps or intermediate RAM steps.

References
Roelvink, 2004. Some strategies in morphodynamic modelling. EstProc. WL | Delft Hydraulics report Z3040, March 2004.

2.8.7 EP26 - Algorithm on Estuarine characteristics (POL – Prandle)

Aim Frameworks of characteristic estuarine values, as functions of depth, D, and tidal amplitude, $\hat{\zeta}$ are illustrated for the following parameters. This summarises results from a paper to appear in 'Progress in Oceanography'.

Background
The derived assumptions from the analysis are as follows: (see later for definition of symbols):

(a) **tidal current amplitude** $\hat{U}$ indicating a dependency on $\hat{\zeta}^{1/2}\, D^{1/4}\, f^{-1/2}$ in shallow water.

(b) **ratio of friction: inertia terms**, shown to be proportional to $10\,\hat{\zeta}/D$, the latter providing a demarcation of 'shallow water' in terms of friction predominating.

(c) **estuarine length, L,** proportional to $D^{5/4}/(f\,\hat{\zeta})^{½}$ with depth increasing axially at a rate $x^{0.8}$

(d) **stratification**, based on both the Simpson-Hunter criteria D/U^3 or on the time for vertical mixing by diffusion D^2/K_z, the latter giving an indication of intra-tidal stratification.

(e) **salinity intrusion, L_I**, proportional to $D^2/f\ U_o\ \hat{U}$ based on four independent approaches.

(f) **bathymetry**, definition of zone bounded by $L_I/L < 1$, $E_x/L < 1$ (E_x tidal excursion) and $D/U^3 > 55\ m^{-2}\ s^3$.

(g) **mean sediment concentration**, $\overline{C}$ time and depth-averaged values for fine sediments, proportional to $\hat{U}$.

(h) **flushing time**, F_T proportional to L_I/U_o

(i) **In-fill time I**, proportional to $F_T/\overline{C}$

Synchronous estuary
Frictional and energy conservation effects can combine in funnel-shaped bathymetry to produce a 'synchronous estuary' with constant tidal elevation amplitudes. For such partially-mixed, tidally dominated, estuaries, new theories have been developed and translated into characteristic responses for:

- tidal propagation, saline intrusion and sedimentation.

Moreover, by inter-relating these responses new expressions are derived linking bathymetry to dynamics.

Tidal dynamics – estuarine length
The dynamics of tidal propagation are examined for the particular case of a synchronous estuary with a triangular section and a predominant (M_2) tidal constituent. Incorporating these approximations into the cross-sectionally averaged governing equations, produces, for prescribed values of $\hat{\zeta}$ and D, an estimate of bed slope. Axial integration of this slope enables both the shape and length of the estuary to be determined.

$$\tan\theta = -\frac{F}{\omega} = \frac{S}{\frac{1}{2}Dk} \tag{1}$$

where $S = \partial D / \partial x$

$$\hat{u} = \hat{\zeta} gk \Big/ \left(\omega^2 + F^2\right)^{\frac{1}{2}} \tag{2}$$

$$k = \omega \Big/ \left(\frac{Dg}{2}\right)^{\frac{1}{2}} \tag{3}$$

u is velocity in the x direction, ζ is water level, D is water depth, H is the total water depth (H = D + ζ), f is the bed friction coefficient (≈ 0.0025), B is the channel breadth, A the cross sectional area, g gravitational acceleration, t time and θ the phase lag of currents to elevation

Utilising the values of S from eqn (1), the length, L, of an estuary is calculated by successively updating S as D reduces along the estuary (assuming a constant value of $\hat{\zeta}$).

By assuming $F >> \omega$, an equivalent simple analytical solution can be determined:

$$D = \left(\frac{5}{4} \frac{\left(\hat{\zeta} 1.46\, f\omega\right)^{\frac{1}{2}}}{(2g)^{\frac{1}{4}}} \right)^{\frac{4}{5}} x'^{\frac{4}{5}} \tag{4}$$

where $x' = L - x$

$$\text{or} \quad L = \frac{D_o^{\frac{5}{4}}}{\hat{\zeta}_o^{\frac{1}{2}}} \frac{4}{5} \frac{(2g)^{\frac{1}{4}}}{(1.46 f\omega)^{\frac{1}{2}}} \quad \approx \quad 2350 \quad \frac{D_o^{\frac{5}{4}}}{\hat{\zeta}_o^{\frac{1}{2}}} \qquad \text{for } f = 0.0025 \tag{5}$$

(units m, subscripts o denote values at the mouth).

Salinity intrusion, length and location

The related dynamics of saline intrusion were examined for the case of a vertically and temporally constant axial salinity gradient. An expression for the length of saline intrusion was derived.

The earlier derivation of tidal current amplitudes enables direct estimation of the Simpson-Hunter (1974) stratification parameter $D/\hat{U}^3$. The results indicate that estuaries with tidal elevation amplitudes $\hat{\zeta}$ > 1m will generally be mixed, exceeding the 55 m^{-2} s^3 demarcation separating mixed from stratified conditions.

Prandle (1985) derived the following expression for saline intrusion length, L_I,

$$L_I = 0.0016 \frac{D^2}{f \hat{U} U_o} \text{ (m)} \quad (6)$$

Sea-bed velocities
The following estimates of velocity components at the sea bed were derived:

associated with S_X, $U_{SO} = -0.029 \frac{g D^2 Sx}{f \hat{U}}$ (7)

associated with depth-mean river flow U_o, $U_{oo} = 0.7 U_o$ (8)

A simple hypothesis for the limit of upstream intrusion of salt is the position where these upstream and downstream velocity components balance, i.e. where:

$$L_I = \frac{0.011 D^2}{f \hat{U} U_O} (m) \quad (9)$$

Utilising a derived criterion of minimum landward intrusion and incorporating the earlier derivations for both estuarine length and saline intrusion length, an expression for U_o , the river-flow component of residual velocity at the centre of the intrusion, was derived in terms of the depth, D_i.

$$U_o = D_i^{1/2} / 333 \quad m\ s^{-1} \quad (10)$$

The expression indicates values of U_o, the residual component of river flow at the centre of the intrusion, ranging from 0.006 to 0.012 m s^{-1} for D_i from 4 to 16 m. These estimates for U_o are independent of : tidal range , bed friction coefficient and steepness of side slopes Moreover, these values for U_o accord well with observed values which are invariably around 1 cm s^{-1}.

Bathymetry as a function of river flow
These latter analyses were extended further to provide an expression for estuarine depth, D_o, at the estuarine mouth in terms of the river flow and side slope , a , of the triangular cross section.

$$D_o = 12.8 (Qa)^{0.4} \quad (11)$$

Combining this result with eqn (5), the estuarine length, L, is given by:

$$L = 2850 \left(\frac{Qa}{f \hat{\zeta}} \right)^{1/2} \quad (12)$$

The results for U_o, eqn (10) and D_o, eqn (11) are independent of both the friction coefficient, *f*, and the tidal amplitude, $\hat{\zeta}$. However, the expression for estuarine length , eqn (12) , is dependent on the inverse square root of both of these parameters.

Examination of a UK observational data set indicated that: 0.02 > a > 0.002, eqn (11) then corresponds to

$$2.68\ Q^{0.4} > D_o > 1.07\ Q^{0.4} \tag{13}$$

i.e. an estimate for D_o directly in terms of Q (again independent of either tidal range or bed friction coefficient). Comparison of the associated envelope of D as a function of Q again accords sensibly with observed values. Thus, this study provides a complete description of estuarine bathymetry (i.e. depth, length and axial shape) in terms of Q, $\hat{\zeta}$ and f, i.e. an obvious set of 'natural' boundary conditions.

Sedimentation

Erosion formulae generally take the form:

$$ER(t) = \rho\ \gamma f\ (U(t) - U_c)^P \tag{14}$$

For a tidally dominated regime, erosion rate ER(t) is relatively insensitive to either the power P (over the commonly encountered range of 2 to 5) or the critical erosion threshold U_c (for $U_c < 0.5\ \hat{U}$). Hence for simplicity we adopt:

$$P = 2, \quad \gamma = 0.0001\ m^{-1}\ s \text{ and } U_c = 0 \tag{15}$$

The corresponding time and depth averaged concentrations are given by

$$C = \gamma\ \rho\ f\ \frac{\hat{U}^2}{2} \Big/ D\ \alpha \tag{16}$$

Estimates of in-fill times

Utilising existing theories on the nature of locally resuspended sediment regimes in tidally dominated regimes, it was shown that significant estuarine siltation is most likely to occur via the entrainment of fine marine sediments. Moreover, the transport of such sediments in estuaries (of the kind considered) approximates that of a conservative tracer such as salt.

For the conditions of $\frac{\partial S}{\partial x} = S_x$ (constant), assumed above, and eq (9) for L_I, we can arrive at an estimate of salinity flushing times,

$$F_T = \frac{0.5\ (L_I/2)}{U_o} = \frac{0.0013\ D^2}{f\ \hat{U}\ U_o^2} \tag{17}$$

Thence by combining theoretical estimates of time and depth averaged sediment concentrations with flushing times arrives at an expression for maximum rates of estuarine in-filling estimated as

$$I = \rho\ F_T \Big/ 0.69\ \overline{C} \tag{18}$$

This indicates **minimum** infill times, ranging from around 25 years in shallow estuaries with high tidal ranges up to thousands of years in deep estuaries with small tides. Observed capture rates of available marine sediments are generally only a few percent of the total flux, suggesting these minimum in-fill times might be increased by at least an order of magnitude. Hence these results suggest that bathymetric changes over decadal time scales are likely to be minor for all but the shortest and shallowest of estuaries.

Validation

These algorithms are undergoing further validation in project FD2107. They are provided to indicate estuarine behaviour.

See papers at http://www.pol.ac.uk/erp/fd2107/documents.html

Reference

Prandle, D. 1985. On salinity regimes and the vertical structure of residual flows in narrow tidal estuaries. Estuarine Coastal & Shelf Sciences, 20, 615-633.

Prandle,D. 2004. How tides and river flows determine estuarine bathymetries. To appear in Progress in Oceanography

Simpson, J.H. & Hunter, J.R. 1974. Fronts in the Irish Sea. Nature, 250, 404-406.

2.9 Biological process parameters that effect stability, erodibility and deposition of sediments

2.9.1 EP27 - Algorithm for Sediment-Biology Interaction (ABP – Jackson)

Aim To determine a method to assist with the preliminary assessment of the importance of sediment parameters in contributing to prediction of species abundance.

Background
The flow diagram below details the proposed algorithm. The accompanying text provides an illustration of how this technique has been applied on the Humber Estuary. More detail on this approach is provided in ABPmer (2004).

Stages 1 and 2

A 3-dimensional hydrodynamic model of the Humber Estuary has been developed by ABPmer and WL | Delft Hydraulics (ABPmer and WL | Delft Hydraulics, 2002). This allows the determination of physical parameters throughout the Humber Estuary in a series of grid cells.

Physical parameters derived from the model include:

- Salinity;
- Current (m/s);
- Bed shear stress (N/m^2);
- Elevation (m); and
- Water level.

These values were extracted from the model over three spring and neap tides. An average spring and neap value for each of the parameters was then derived for each grid cell within the model. To avoid distortion the average values were only calculated for the period when the grid cell is covered in water. The elevations for the intertidal area of the grid were refined using LiDAR data.

LiDAR data, at a resolution of 10m x 10m grid cells was available for almost the entire intertidal zone of the Humber Estuary. Each of the model grid cells were therefore divided into a number of smaller cells corresponding to the LiDAR grid. The physical attributes of the numerical model grid were therefore assigned to each of the LiDAR grid cells within each model grid cell. The end result is a model of the intertidal area of the Humber Estuary divided into 10m x 10m grid cells with each cell containing a unique set of physical attributes.

Stage 3
The Humber Estuary was first divided into four broad scale assemblages, each characterised by a suite of intertidal species. This was done based on historic data collected by the Environment Agency (EA).

Stages 4 and 5
The invertebrate composition of three of the identified assemblages were characterised in more detail in 2000 and 2003. The organic content, particle size analysis, erosion thresholds and shear strength were also collected in the field. Once this was completed, physical data was extracted through GIS from model grid cells for all corresponding sampling points and used as described below in a rule-based analysis on selected intertidal species.

Stage 6
Investigation of the relationship between the biotic and abiotic parameters required application of the AnswerTree™ analytical software. This creates classifications displayed in decision trees. As an exploratory analysis tool, it attempts to relate predictive attributes to values of a continuous variable. It also creates rules that can then be tested to predict future events. The resulting trees provide a means of representing hierarchical structure in the data. On the Humber these have been used to define a series of rules for predicting the distribution of intertidal species based on physical parameters.

Stages 7 to 10
The rule-based predictions can then be used to produce predicted abundance maps for a given species in a given estuary. On the Humber Estuary these predicted maps have been compared to observed data to test the predictions that have been made. As new data has been collected this has been used to further refine the rules that have been developed.

Reference
ABPmer and WL | Delft Hydraulics (2002). Humber Estuary Shoreline Management Plan – Stage 2. Hydrodynamic Model Calibration Report.

ABPmer (2004). A Study into the Significance of Sediment Data in the Prediction of Invertebrate Biology on the Humber Estuary, Report R.1077.

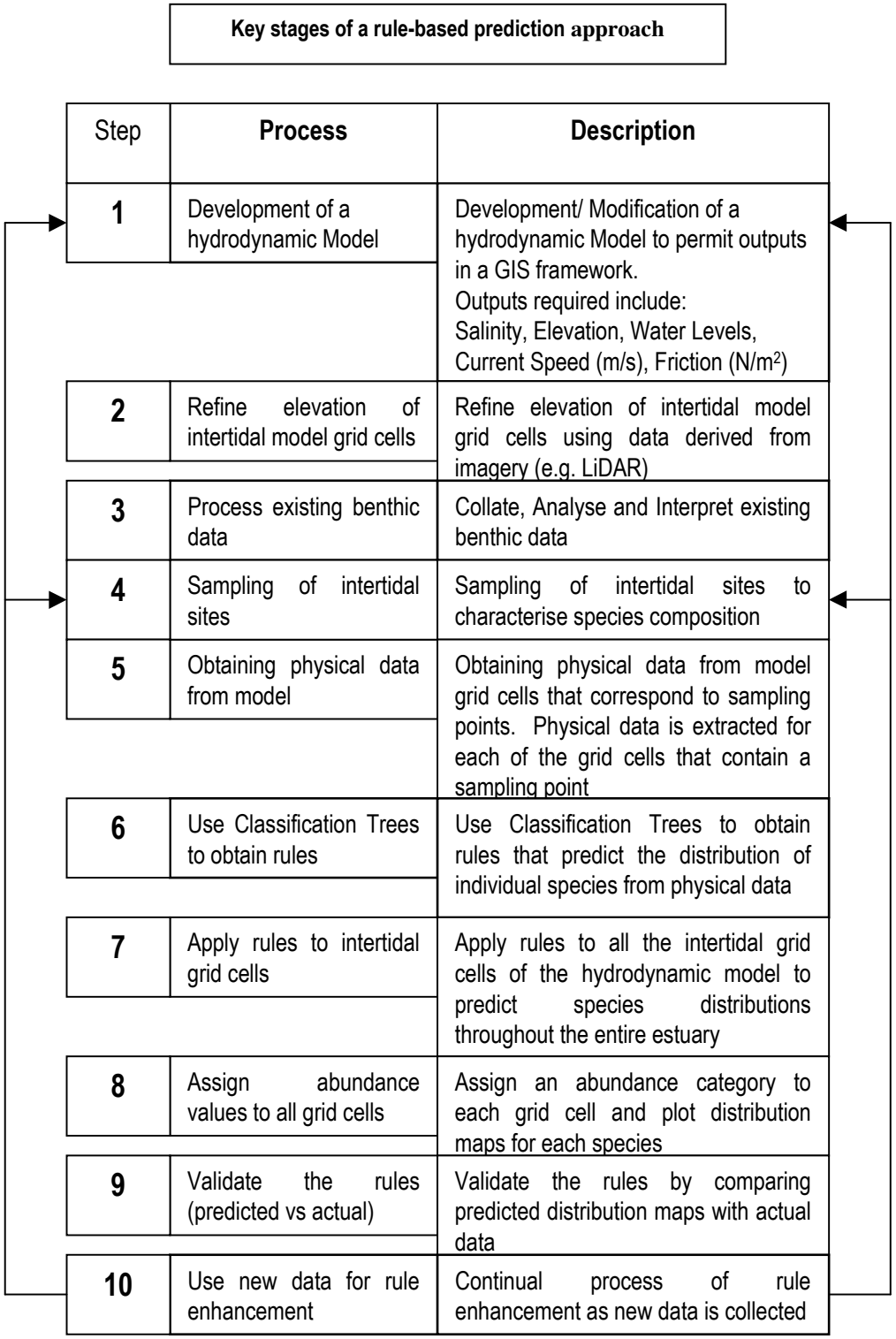

Figure 1 Flow diagram for a rule-based approach for predicting species abundance in estuaries

2.9.2 EP28 - Algorithm for biological process parameters that affect stability, erodibility and deposition of sediments (PML – Widdows)

Aim To incorporate the impact of key intertidal biota and biological processes on sediment stability / erodibility and deposition into numerical models of estuarine sediment dynamics and morphology.

Scientific Background
A wide range of biota are known to modify sediment stability / erodibility and sediment deposition rates through a variety of biological processes which characterise two functional groups:- bio-stabilisers and bio-destabilisers. These processes include:-

Biostabilisation
1) Enhanced sediment cohesion (e.g. microphytobenthos)
2) Filamentous binding (e.g. *Cladophora*)
3) Armouring / biofiltration / biodeposition (e.g. mussel beds)
4) Vegetation inducing attentuation of near-bed flows and waves

Bio-destabilistion
1) Burrowing activity increasing bed roughness and sediment water content (e.g. bivalves)
2) Bioresuspension (e.g. mysids, *Corophium*)
3) Corrasion by saltating shell material

Sediment stability is ultimately dependent on the balance between the bio-stabilisers and the bio-destabilisers and this will vary spatially (e.g. height on shore and along salinity gradient) and temporally (e.g. seasonally and inter-annually).

Improvement in Understanding
Numerical models of estuarine sediment dynamics and morphology need to incorporate biological as well as physical processes in order to represent the natural estuarine environment. Biota can significantly influence near-bed flows, turbulence, thresholds for sediment erosion, erosion rates and deposition rates. For example, biota can alter the erosion rate by > 2 orders of magnitude, particularly when there is a temporal (interannual) shift from bio-stabilised to a bio-destabilised sediment. These changes need to be incorporated into the next generation of models. A summary of results is included in Table 1. A row is included for *Spartina* but the data is not fully analysed for inclusion in EstProc.

Table 1 Summary of scale of impact of key intertidal biota on sediment stability / erodibility

Biological process	Species	Density range	$\Delta \bar{U}_{crit}$ m s^{-1}	Δ Erosion rate	Δ Sedimentation rate	Comments
Bio-stabilisation	Benthic diatoms	10 - 50 µg Chloro *a* g^{-1}	+ 0.15	10-fold reduction	0	Cohesive sediments (mud to mud-sand)
Bio-stabilisation Bio-deposition	Mussels	0 – 2600 m^{-2}	0	8-fold reduction	40-fold	Cohesive and non-cohesive sediments
Bioturbation	*Macoma balthica* Clam	0 - 1,500 m^{-2}	- 0.05	4-fold increase	0	Cohesive sediments (mud to mud-sand) Max density in field 10,000 m^{-2}
Bio-stabilisation	*Enteromorpha* Macroalga	0 – 100 g dw m^{-2}	+0.05	10-fold reduction	1.5-fold	Found on range of sediments but only non-cohesive sediments studied
Bio-stabilisation	*Cladophora* Filamentous alga		+ 0.15	10-fold reduction	0	Cohesive mud
Bio-stabilisation	*Spartina anglica* Saltmarsh	400 – 1200 stems m^{-2}		10-fold reduction	0	Reduced erosion due to 5-fold reduction in near-bed flows
Bio-resuspension in upper estuary	*Neomysis integer* Mysid	0 – 2000 m^{-2}	- 0.13	4-fold increase	0	Active bio-resuspension of up to 28g m^{-2} at <0.05 m s^{-1} (i.e. no flow induced erosion)

$\Delta \bar{U}_{crit}$ (m s^{-1}) - Expressed relative to a natural undisturbed sediment with minimal biotic influence which has a $\bar{U}_{crit}$ of 0.18 to 0.20 m s^{-1}

Implementation
The majority of experimental flume studies have quantified the impact of biota density on the relationship between sediment erodibility and near-bed current velocity or bed shear stress.

In these studies, biota density is expressed as individuals m^{-2}, or biomass (g m^{-2}), or a proxy for density such as microphytobenthic chlorophyll *a* (µg g dry $^{-1}$ sediment). Sediment erodibility is expressed in terms of sediment mass eroded (g m^{-2}), and / or erosion rate (g m^{-2} s^{-1}) and the threshold for erosion, either in terms of critical erosion velocity (U_{crit}; m s^{-1}) or threshold of shear-stress for erosion (τ_b; N m^{-2}).

Algorithms

Inputs
- Near-bed current velocity, either depth averaged over 15 cm or U at a height of 0.1m (U_{10}), or bed shear stress (τ_o), calculated using ADV to measure the turbulent kinetic energy (TKE).
- Density of biota.

Outputs
- Sediment mass eroded (g m^{-2})
- Erosion rate (g m^{-2} s^{-1})
- Critical erosion velocity (U_{crit}) or critical bed shear stress for erosion (τ_{cr}; N m^{-2})

The non-linear relationships describing the impact of biota density on sediment erodibility in relation to current speed cannot be accurately represented by response surface analysis (primarily due to critical erosion thresholds creating an inflection). Therefore the relationships are simply presented as a series of regression equations for a series of current velocities or bed shear stresses.

Relationship between current speed and bed shear stress (Already presented as algorithm EP15)
The conversion of near-bed current speed (U_{10}) to bed shear stress for relatively smooth mud is described by the following equation:

$$\text{Bed shear stress (Pa)} = 0.4702U_{10}^3 + 1.152U_{10}^2 + 0.1553U_{10} \qquad r^2 = 0.99$$

where U_{10} is velocity in m s^{-1} at 10cm above the bed.
This relationship was established in the flume and field using an ADV for measuring currents and bed shear stress (TKE method).

It is important to note that many of the algorithms presented below include the current velocity measured at 10cm above the bed. For application in studies it will be necessary to calculate the velocity at 10cm above the bed directly, or through appropriate correction of velocities measured further away from the bed.

EP28.1) Microphytobenthos / Benthic diatoms
Microphytobenthos have a major influence on the cohesiveness and stability of the sediment.

This is achieved through the production of mucus-like carbohydrates or EPS (extracellular polymeric substances). Their intertidal distribution ranges from below mid-tide to above the mean neap high tide level, and from fully marine to the upper estuary at low salinities (0-1). Microphytobenthos are present throughout the year ranging from 2 µg g^{-1} dry sediment in the winter to 60 µg g^{-1} in June (summer). The main effect on sediment stability is through increasing the critical threshold for erosion (i.e. u_{*crit} or U_{crit}).

Relationship between u_{*crit} and chlorophyll *a* concentration – a proxy parameter for microphytobenthic density - has been measured in laboratory and *in situ* annular flumes by Sutherland et al (1998a,b). It has been consistently demonstrated in other field studies involving flumes.

Critical shear velocity u_* (m s^{-1}) = 0.0058 + 0.0001(*chl*) r^2=0.96

where chl = concentration of chlorophyll a in to top 2mm of sediment, measured in µg g^{-1} dry sediment.

Assuming that u* is 3.6% of U_{10} then there is good agreement between Sutherland et al (1998a,b) and U_{crit} derived from PML's annular flume measurements in field studies (Widdows et al. 2000a).

Limitations
The algorithm is dependent on the accuracy of the bed shear stress determinations.

The algorithm is based on fine cohesive sediments, however, a similar relationship is also observed for mud-sand mixtures (Westerscheldt; Widdows et al. 2000a, 2004). In the Westerscheldt the U_{crit} and τ_b values are similar to the fine mud but the mass eroded and erosion rates were higher due to the nature of the sediment.

Validation
Field measurements in various estuaries including the Humber and Blackwater (fine muds), and the Westerscheldt and Wadden Sea (mud-sand mixtures), have consistently shown a significant relationship between U_{crit} or τ_b and chlorophyll *a* or carbohydrates (extracellular polymeric substances). Modelling of sediment dynamics over the Skeffling mudflat (Humber) and the Molenplaat tidal flat (Westerscheldt) has demonstrated that biota (microphytobenthos) can play an important role in sediment erosion, transport and deposition (Wood and Widdows, 2002; Widdows et al. 2004). The output from the models showed good agreement with field data, both in terms of SPM and accretion rates.

References
Sutherland, T.F., Amos, C.L., & Grant, J. 1998a. The effect of buoyant biofilms on the erodibility of sublittoral sediment of a temperate microtidal estuary. Limnology and Oceanography, 43, 225-235.

Sutherland, T.F., Grant, J., & Amos, C.L. 1998b. The effect of carbohydrate production by the diatom *Nitzschia curvilineata* on the erodibility of sediment. Limnology and Oceanography, 43, 65-72.

Widdows, J., A. Blauw, C.H.R., Heip, P.M.J. Herman, C.H. Lucas, J.J. Middelburg, S. Schmidt, M.D. Brinsley, F. Twisk, H. Verbeek. 2004. Role of physical and biological processes in sediment dynamics (sedimentation, erosion and mixing) of a tidal flat in Westerschelde estuary, S.W. Netherlands. (MEPS In press).

Widdows. J. & Brinsley, M.D. 2002. Impact of biotic and abiotic processes on sediment dynamics and the consequences to the structure and functioning of the intertidal zone. *Journal of Sea Research* 48, 143-156.

Widdows, J. Brinsley, M.D., Salkeld, P.N. and Lucas, C.H. 2000a. Influence of biota on spatial and temporal variation in sediment erodibility and material flux on a tidal flat (Westerschelde, Netherlands). Marine Ecology Progress Series, 194, 23-37.

Wood, R. & Widdows, J. 2002. A model of sediment transport over an intertidal transect, comparing the influences of biological and physical factors. *Limnology and Oceanography* 47, 848-855.

EP28.2) <u>*Macoma balthica*</u>

Macoma is a small clam that can occur at high densities (>10,000 individuals m^{-2}) in estuarine sediments ranging from fine mud to mud-sand mixtures. It is a surface deposit feeder, grazing on the microphytobenthos, thereby loosening the surface sediments, increasing bed roughness and water content.

Annular flume studies examined the effect of 5 *Macoma* densities (0, 250, 500, 1000, 1500 clams m^{-2}) on sediment mass eroded (g m^{-2}) at 7 different current speeds (Widdows et al. 1998a). Sediment mass eroded reached a near steady state after 20 minutes at each current speed. Relationships between sediment mass eroded and *Macoma* density (x as number m^{-2}) for different current speeds (U_{10}) are described by the following equations:-

U_{10} @ 0.10 m s^{-1}	Mass eroded (g m^{-2}) = $3E\text{-}06x^2 - 0.0015x + 1.5624$	r^2=0.998
U_{10} @ 0.15 m s^{-1}	Mass eroded (g m^{-2}) = $-1E\text{-}05x^2 - 0.0536x + 6.774$	r^2=0.989
U_{10} @ 0.20 m s^{-1}	Mass eroded (g m^{-2}) = $-2E\text{-}05x^2 - 0.1653x + 86.095$	r^2=0.998
U_{10} @ 0.25 m s^{-1}	Mass eroded (g m^{-2}) = $-8E\text{-}05x^2 - 0.3362x + 283.63$	r^2=0.977
U_{10} @ 0.31 m s^{-1}	Mass eroded (g m^{-2}) = $-0.0002x^2 - 0.5569x + 503.2$	r^2=0.975
U_{10} @ 0.37 m s^{-1}	Mass eroded (g m^{-2}) = $-0.0001x^2 - 0.5401x + 564.13$	r^2=0.986
U_{10} @ 0.45 m s^{-1}	Mass eroded (g m^{-2}) = $-0.0002x^2 - 0.5502x + 596.72$	r^2=0.986

Macoma reduced U_{crit} by at least 0.05 m s^{-1} (i.e. 0.15 to 0.10 m s^{-1}) at all densities and there was no apparent density dependent relationship.

Limitations

The range of *Macoma* density studied (0-1500 m^{-2}) was lower than the observed range in the field (0-10,000 m^{-2}). However, there is evidence that the enhanced sediment resuspension at 1500 *Macoma* m^{-2} may be reaching an asymptote and that further destabilisation of the sediment may be limited at higher densities due to the re-working of the whole sediment surface.

This study may have slightly underestimated the full impact of *Macoma* on sediment stability because the sediment was sieved of macrofauna and allowed to settle /

consolidate in the flume over a period of 45 days before the beginning of the experiment. The stability of the 'control' sediment, without *Macoma* (U_{crit} = 0.15 m s^{-1}), was probably slightly lower than natural undisturbed sediment with minimal biotic influence (U_{crit} = 0.18 to 0.20 m s^{-1}).

Validation

The laboratory derived relationship between *Macoma* density and increased sediment erodibility, measured in terms of lower U_{crit} and an increase in erosion rate (Widdows et al. 1998a), has been observed in several field studies (e.g. Humber, Widdows et al 1998b, 2000b; Westerscheldt, Widdows et al 2000a).

References

Widdows, J., Brinsley, M.B., Salkeld, P.N. and Elliott, M. 1998a. Use of annular flumes to determine the influence of current velocity and biota on material flux at the sediment-water interface. *Estuaries* 21, 552-559.

Widdows, J., Brinsley, M.D. and M. Elliott. 1998b. Use of *in situ* flume to quantify particle flux (deposition rates and sediment erosion) for an intertidal mudflat in relation to changes in current velocity and benthic macrofauna. *In*: Black, K.S., Paterson, D.M. and Cramp, A. (eds) *Sedimentary Processes in the Intertidal Zone*. Geological Society. London, Special Publications, 139, 85-97.

Widdows, J. Brinsley, M.D., Salkeld, P.N. and Lucas, C.H. 2000a. Influence of biota on spatial and temporal variation in sediment erodibility and material flux on a tidal flat (Westerschelde, Netherlands). Marine Ecology Progress Series, 194, 23-37.

Widdows, J., Brown, S., Brinsley, M.D., Salkeld, P.N. and Elliott, M. 2000b. Temporal changes in intertidal sediment erodibility: influence of biological and climatic factors. Continental Shelf Research, 20, 1275-1289.

EP28.3) Mussels

a) Sediment erodibility

Mussel beds extend from below the low spring tide level up to the mid tide level. Extensive mussel beds represent important biogenic reefs physically protecting the bed from erosion by tidal currents and waves. However, the effectiveness of this armouring depends on the mussel density and the nature of the sediment (Widdows et al. 1998a; 2002b). Experimental flume studies have shown reduced sediment erodibility with increasing mussel density (i.e. surface coverage %) for cohesive muddy sediments.

Annular flume studies examined the effect of 4 mussel densities (0, 10, 50, 100% cover, where 100% cover was equivalent to 2600 mussels m^{-2}) on sediment mass eroded (g m^{-2}) at 6 different current speeds (Widdows et al. 1998a). Relationships between sediment mass eroded and mussel density (x = % cover) for different current speeds (U_{10}) are described by the following equations:-

U_{10} @ 0.15 m s^{-1}	Mass eroded (g m^{-2}) = $0.7281e^{0.0028x}$	r^2= 0.018
U_{10} @ 0.20 m s^{-1}	Mass eroded (g m^{-2}) = $5.5664e^{-0.0038x}$	r^2= 0.069
	(i.e. no significant erosion @ <0.20 m s^{-1})	
U_{10} @ 0.25 m s^{-1}	Mass eroded (g m^{-2}) = $42.86e^{-0.0147x}$	r^2=0.88
U_{10} @ 0.30 m s^{-1}	Mass eroded (g m^{-2}) = $126.93e^{-0.0164x}$	r^2=0.98

U_{10} @ 0.35 m s^{-1}	Mass eroded (g m^{-2}) = $304.48e^{-0.0195x}$	r^2=0.94
U_{10} @ 0.40 m s^{-1}	Mass eroded (g m^{-2}) = $501.37e^{-0.0206x}$	r^2=0.96

Algorithms are for cohesive muds.

b) Biodeposition

Suspension feeders filter small suspended particles (2 – 500 µm) from the water column and convert them into larger mucus bound packages or biodeposits (mm scale) comprised of pseudofaeces and faeces. These biodeposits have a higher settling velocity and sink rapidly to the bed. The gradual accumulation of biodeposits produced by mussel beds usually results in increases in bed height of 1-2 m and this can have a major impact on estuarine morphology.

Mussels are suspension feeders that have high pumping and filtration rates. For example, an individual mussel of 5cm shell length can pump ~ 3 L h^{-1} through its gills at low SPM concentrations (5mg l^{-1}) and this declines linearly with SPM and eventually ceasing pumping at ~ 300 mg l^{-1}. All particles >2µm are filtered from the water with 100% efficiency. However, in polluted estuaries the pumping rates of mussels may be 50% lower (i.e. 1.5 to 2 L h^{-1}).

Mussel filtration rate (mg h^{-1}) = Pumping rate (L h^{-1}) * SPM (mg l^{-1}).

In turbid estuarine water a large proportion of the filtered material is rejected as pseudofaeces (after sorting by the gills and labial palps and before ingestion) and the proportion rejected increases with SPM. This material is deposited to the bed at current speeds (U_{10}) of <0.15 m s^{-1} and resuspended at currents >0.2 m s^{-1}. Mussels settle and grow in dynamic environments with good water exchange, and therefore only a small proportion of the total material biodeposited over slack water will be accumulated in the sediments. The bulk of the material deposited during slack water will be resuspended and transported away by the higher currents (i.e. >0.20 m s^{-1}) on the flood and ebb tides. The proportion of biodeposits trapped and deposited by the mussel bed in the long-term will be dependent on prevailing currents and bed density (no quantitative information available).

Relationship between filtration rates (net biodeposition rate) and mussel bed density (0-1400 individuals m^{-2}) at low current speeds (U_{10}<0.10 m s^{-1}):

$$\text{Filtration or Biodeposition rate (g } m^{-2} h^{-1}) = 0.042x + 4.3152 \qquad r^2 = 0.99$$

where x is the density of individuals m^{-2}.

Biodeposition rates are highly dependent on the density of mussels, at least up to a density of 1400 mussels m^{-2} (Widdows et al. 1998a). Above this density there is evidence of a decline probably due to inhibitory effects on feeding at the high densities (i.e. physical interference due to overcrowding and seston depletion near the bed).

Limitations
Flume experiments have shown more marked non-linear relationship for sediment resuspension as a function of mussel density for sandy sediments (Widdows et al. 2002). This is primarily due to increased scouring and resuspension of sediment and biodeposits around mussel clumps at low density. However, it is not possible to derive an equation with an adequate fit to represent these non-linear relationships.

Validation
The laboratory derived relationships between mussel density and sediment erodibility for both cohesive and non-cohesive sediments are consistent with field observations (Humber and Exmouth) of increased erosion and scouring at low mussel density in contrast to well protected and elevated beds at high density.

References
Widdows, J., Brinsley, M.B., Salkeld, P.N. and Elliott, M. 1998a. Use of annular flumes to determine the influence of current velocity and biota on material flux at the sediment-water interface. *Estuaries* 21, 552-559.

Widdows, J., Lucas, J.S., Barrett, C., Brinsley, M.D., Salkeld, P.N. and Staff, F.J. 2002. Investigation of the effects of current velocity on mussel feeding and mussel bed stability using an annular flume. Helg. Mar. Res. 56, 3-12.

EP28.4) *Enteromorpha*
The macroalga, *Enteromorpha,* forms extensive algal mats on the midshore of many estuaries and is often regarded as a nuisance alga with deleterious ecological consequences. *Enteromorpha* density varies seasonally, growing rapidly during the spring and summer and then dies back during the winter. The growth and persistence of macroalgae in estuaries may be due in part to the positive feedback that it induces. *Enteromorpha* has been shown to lower near-bed flow, thus reducing sediment resuspension and turbidity, which in turn increases light penetration, and this will enhance its growth potential. Experimental flume studies have shown that near-bed flow is reduced by 14% to 46%, and sediment erodibility is reduced from 2 to 10-fold, with increasing *Enteromorpha* density from 10 to 60% (% defined as percentage cover when air exposed). The presence of *Enteromorpha* also significantly enhanced sedimentation rates of fine mud by ~50% at 60% cover.

Annular flume studies quantified the impact of different *Enteromorpha* densities on sediment mass eroded at different flume speeds. The data set has had to be normalised due to the influence of a number of factors that could not be controlled throughout the series of experiments. The studies were carried out during the period from spring to autumn when there were different natural densities from bare sediment (0), 8 g dry mass m^{-2}, 22 g m^{-2} and 106 g m^{-2}. The highest density was equivalent to ~60% coverage of sediment surface during aerial exposure. Sediment mass eroded increased with increasing flume speed (rpm), and sediment erosion and near-bed flows were significantly reduced with increasing *Enteromorpha* density (Romano et al. 2003). The erodibility of the sediment was also found to vary seasonally. Hence the data has been normalised to sediment mass eroded from bare sediment at near-maximum flume speed (67rpm).

Relationships between sediment mass eroded at different *Enteromorpha* densities, normalised to bare sediment, and expressed relative to flume speed (x; rpm) are described by the following equations:

0 (bare)	Mass eroded relative to bare sediment at 67rpm = $2.4E\text{-}08x^{4.1928}$	$r^2 = 0.996$
8 g m^{-2}	Mass eroded relative to bare sediment at 67rpm = $3E\text{-}12x^{6.1691}$	$r^2 = 0.988$
22 g m^{-2}	Mass eroded relative to bare sediment at 67rpm = $4E\text{-}07x^{3.0149}$	$r^2 = 0.981$
106 g m^{-2}	Mass eroded relative to bare sediment at 67rpm = $8E\text{-}09x^{3.8128}$	$r^2 = 0.988$

The normalisation of the data to bare sediment at 67rpm was equivalent to a sediment mass eroded of 350 g m^{-2} in July.

Near-bed flows are reduced by the increased drag induced by the *Enteromorpha*. Relationships between flume rpm (range from 8 to 75rpm) and depth averaged current speed ($\bar{U}$, m s^{-1}) between 1 and 12 cm above sediment with and without *Enteromorpha* are described by the following equations:-

0 (Bare)	$\bar{U} = 0.00522$ (rpm)	$r^2 = 0.99$
8 g m^{-2} Entero	$\bar{U} = 0.00447$ (rpm)	$r^2 = 0.97$
22 g m^{-2} Entero	$\bar{U} = 0.00388$ (rpm)	$r^2 = 0.99$
106 g m^{-2} Entero	$\bar{U} = 0.00279$ (rpm)	$r^2 = 0.90$

For example, at the highest *Enteromorpha* density (106 g m^{-2}) currents were reduced by 46% and the bed erosion was reduced by 90% at the high flows (67 rpm).

Limitations

The algorithms apply to sandy non-cohesive sediment (125-250 µm).
ADV measurements were not available at the time of this study so there are no estimates of shear stress.

Validation

None to date, but consistent with general field observations.

Application

A number of the algorithms described above have been applied in computational models, as described in EstProc Consortium (2004) – see Sections 3.2 and 4.2 of that report.

References

EstProc Consortium (2004). Integrated Research Results on Hydrobiosedimentary Processes in Estuaries. Final Report of the Estuary Process Research Project (EstProc). R&D Technical Report prepared by the Estuary Process Consortium for the Fluvial, Estuarine and Coastal Processes Theme. Report No FD1905/TR2 – Synthesis Report

Romano, C., Widdows, J., Brinsley, M.D., Staff, F.J. 2003. Impact of *Enteromorpha* on near-bed currents and sediment dynamics: Flume studies. *Marine Ecology Progress Series* 256, 63-74.

2.9.3 EP29 - Algorithm for the objective definition of a biostabilisation index for sandy intertidal flats using the Cohesive Strength Meter (CSM) (SOES – Friend)

Aim To estabilish a biostabilisation index for use with measurements made using the Cohesive Strength Meter. [One of the devices for determining the erosion threshold condition for cohesive sediments, Black and Paterson, 1997]

Method
An index of biological stabilisation based upon the ratio of the biotic to abiotic critical threshold of sediment motion, is a useful way of comparing the effect of biostabilisation by animals and plants between different sites and different erosion instruments. For cohesive sediments, a lack of an understanding of the physics of particle erosion and the selection of a suitable abiotic control site mean that indices are relative; as such, they are dependent upon qualitative decisions made by the erosion device operator. For example, indices based upon 'biofilm' and 'non-biofilm' areas are likely to underestimate the extent of biostabilisation.

For non-cohesive sediments equations are available to describe the critical shear stress for the initiation of motion and the suspension of abiotic sands. *In situ* field measurements can be compared with measurements undertaken in a laboratory flume, using the same sediment after removal of all the organic material. Whilst this approach provides a truly abiotic comparison, determination of initial motion is still somewhat subjective, depending on definitions such as 'first grain movement', 'shear stress at which significant sediment transport occurs', and 'shear stress at which 10 or more aggregates simultaneously initiate motion in the field of view'. Furthermore, it is not usual that such studies replicate the seawater temperature and salinity that occur in the field, leading to errors in the calculation of settling velocities.

This algorithm provides an objective method of deriving (biotic/abiotic) biostabilisation coefficients from field data on sandy intertidal flats using the CSM. The method is easily repeatable elsewhere, allowing direct comparison of biostabilisation coefficients between non-cohesive intertidal flats. The general procedure outlined by Tolhurst et al. (1999) should be used for processing CSM data. In addition, by recording the temperature and salinity of the ambient seawater at the time of CSM deployment, and by measuring the mean grain-size of sediment immediately adjacent to the test area, the theoretical abiotic suspension threshold can be calculated, using the equations of Bagnold (1966) and McCave (1971), for the resuspension of sand. Note that the settling velocity equation of Soulsby (1997) should be used in preference to the equations of Gibbs et al. (1971) and Baba and Komar (1981).

References
Baba, J. and Komar, P.D., (1981). Measurements and analyses of settling velocities of natural quartz sand grains. *Journal of Sedimentary Petrology* 51(2): 631-640.

Bagnold, R.A., (1966). An approach to the sediment transport problem from general physics. U.S.Geological Survey. Professional Paper 422-I.

Black, K.S. and Paterson, D.M., (1997). Measurement of the erosion potential of cohesive marine sediments: a review of current in-situ technology. *J. Marine Env. Engng*. 4: 43-83.

Gibbs, R.J., Matthews, M.D., and Link, D.A., (1971). The relationship between sphere size and settling velocity. *Journal of Sedimentary Petrology* 41(1): 7-18.

McCave, I.N., (1971). Sand waves in the North Sea off the coast of Holland. *Marine Geology* 10: 199-225.

Soulsby, R., 1997. Dynamics of marine sands: a manual for practical applications. Thomas Telford, London. 249pp.

Tolhurst, T.J., Black, K.S., Shayler, S.A., Mather, S., Black, I., Baker, K., and Paterson, D.M., (1999). Measuring the *in situ* Erosion Shear Stress of Intertidal Sediments with the Cohesive Strength Meter (CSM). *Estuarine, Shelf and Coastal Science* 49: 281-294.

2.10 Linkages between biological processes and morphology

2.10.1 EP30 - Algorithm for relationship between incident wave energy and marsh edge configuration (CCRU – Moeller)

Aim To provide a quantitative indication of the threshold wave energy dictating the erosional form of the seawards saltmarsh boundary.

Scientific Background
A better understanding of the morphological evolution of estuaries, and the better assessment of the relative importance of human interventions versus natural process-driven change in determining estuarine morphology, requires not only an understanding of estuarine channel dynamics but also of the interlinked intertidal mudflat and saltmarsh systems which characterise estuarine margins. Historical data on the extent of mudflats and saltmarshes within UK estuaries confirms a widespread, progressive loss of these habitats over the last one hundred years. However also contained within some of these records are large-scale oscillations between periods of rapid mudflat accretion and saltmarsh progradation and phases of mudflat lowering and saltmarsh retreat. It is currently unclear (a) how such patterns of mudflat and saltmarsh areal change might be explained, and (b) what controls the varying 'types' of erosion (e.g. lateral marsh edge erosion versus internal marsh loss)?

Over the last decade traditional models of estuarine dynamics, based largely on tidal hydrodynamics, have been supplemented by a greater awareness of the importance of wave-tide interactions within estuaries and the role of wind-waves in re-shaping estuarine margins and, through their influence on sediment transport, their affect on estuary-wide sediment budgets and morphological change. Nonetheless the precise nature of the linkages between changes in wind-wave climate and the position of mudflats and saltmarshes remain poorly specified. Various broad correlations have been proposed (e.g. Pye 2000) between changing tidal wetland extent and a range of environmental controls (including changes in sea level and water levels within estuaries, storminess and the prevalence of different weather types and the wave fields associated with them) but these have not been systematically tested either empirically or through mathematical modelling.

However at the *within* estuary scale, considerable progress has been made in understanding the morphodynamic feedbacks between surfaces (often vegetated) and input conditions over a range of space and time scales. At this scale, mudflats and saltmarshes constitute a delicately balanced system between hydrodynamic forcing on the one hand and ecological, sedimentological, and morphological responses on the other. Such intertidal surfaces influence tidal currents and incident waves and significantly dissipate the hydrodynamic energy available for sediment erosion, re-suspension and transport. Knowledge of the feedback mechanisms by which mudflats and vegetated marsh surfaces achieve such energy dissipation, and the thresholds at which these dissipative controls are exceeded, is a key factor in understanding the morphological response of mudflats and marshes to sea-level rise and associated changes in incident wave type/energy. Recent field studies have quantified changes in significant wave heights and total spectral energy across densely vegetated macro-tidal saltmarshes (Moeller et al. 1996, Möller *et al*. 1999, 2002).

Benefits from EstProc
Within the EstProc project, this data has been further analysed to reveal, *inter alia,* broad correlations between incident wave energy and saltmarsh margin type (Möller and Spencer 2002, 2003) showing (Table 1).

Table 1 Relations between maximum observed incident wave energy and saltmarsh – mudflat boundary type at 3 UK East Coast locations in North Norfolk (Stiffkey) and Essex (Tillingham, Bridgewick)

	Edge Configuration	Maximum observed incident wave energy (J/m^2)
Stiffkey, North Norfolk	smooth transition	277
Tillingham, Dengie	mud-mounds	464
Bridgewick, Dengie	cliff	715

Implementation of algorithm
The observed relationship should be used as a guideline and basis for the future determination of more clearly defined hydrodynamic thresholds that mark the transition from one morphological configuration to another.

Limits of applicability
The algorithm is limited in applicability due to the (necessarily) limited extent of data on which it is based. Whilst observations were made near-continuously for a period of at least 12 months at each of the sites, it is possible that it is extreme events, with a return period of less than 1 per year, which are critical in determining morphological change and marsh edge configurations.

Gaps in knowledge
There is a significant gap in our knowledge of the erosion thresholds that once surpassed lead to marsh edge configuration changes. Once a change has been initiated, morphology-process feedbacks become operational and control the further evolution of the marsh/mudflat boundary. Further studies aimed at better defining these thresholds are thus critical.

References
Möller, I. and Spencer, T. 2002. Wave dissipation over macro-tidal saltmarshes: Effects of marsh edge typology and vegetation change. Journal of Coastal Research SI36, 506-521.

Möller, I. and Spencer, T. 2003. Wave transformations over mudflat and saltmarsh surfaces on the UK east coast – Implications for marsh evolution. Proceedings, International Conference on Coastal Sediments 2003 (ASCE, World Scientific Publishing Corp. and East Meets West Productions : Corpus Christi Texas).

Möller, I., Spencer, T. and Rawson, J. 2002. Spatial and temporal variability of wave attenuation over a UK East-coast saltmarsh. Proceedings of the 38th International Conference on Coastal Engineering, Cardiff, July 2002.

Möller, I., Spencer, T., French, J.R., Leggett, D.J. and Dixon, M. 1999. Wave transformation over salt marshes: A field and numerical modelling study from North Norfolk, England. *Estuarine, Coastal and Shelf Science* 49, 411-426.

Moeller, I., Spencer, T. and French, J.R. (1996) Wind wave attenuation over saltmarsh surfaces: Preliminary results from Norfolk, England, *Journal of Coastal Research* 12(4), 1009-1016.

Pye, K. 2000. Saltmarsh erosion in southeast England: mechanisms, causes and implications. in:- B.R. Sherwood, B.G. Gardiner and T. Harris T (eds) British Saltmarshes. Forrest Text / Linnean Society of London : Cardigan / London, 359-396.

Smooth transition topography, Stiffkey

Mud-mound topography, Tillingham

Cliff topography, Bridgewick

2.10.2 EP31 - Algorithm for relationship between saltmarsh accretion, distance from creek and surface elevation in minerogenic marshes (CCRU – Spencer)

Aim The algorithm is presented to illustrate the different time and space controls on estuarine margins and how different scales of process can be linked.

Scientific Background:

Intertidal surfaces evolve over time under the spatial and temporal (individual tide to inter-annual change) patterns of sedimentation that results from tidal flooding. Whereas short-term sedimentation measurements suggest the key control of distance to feeder creek as the prime control on sedimentation rate (Reed et al. 1999), extended monitoring assigns prime importance to surface elevation (through its control on the number of submergences in the longer term) (Figures 1 and 2).

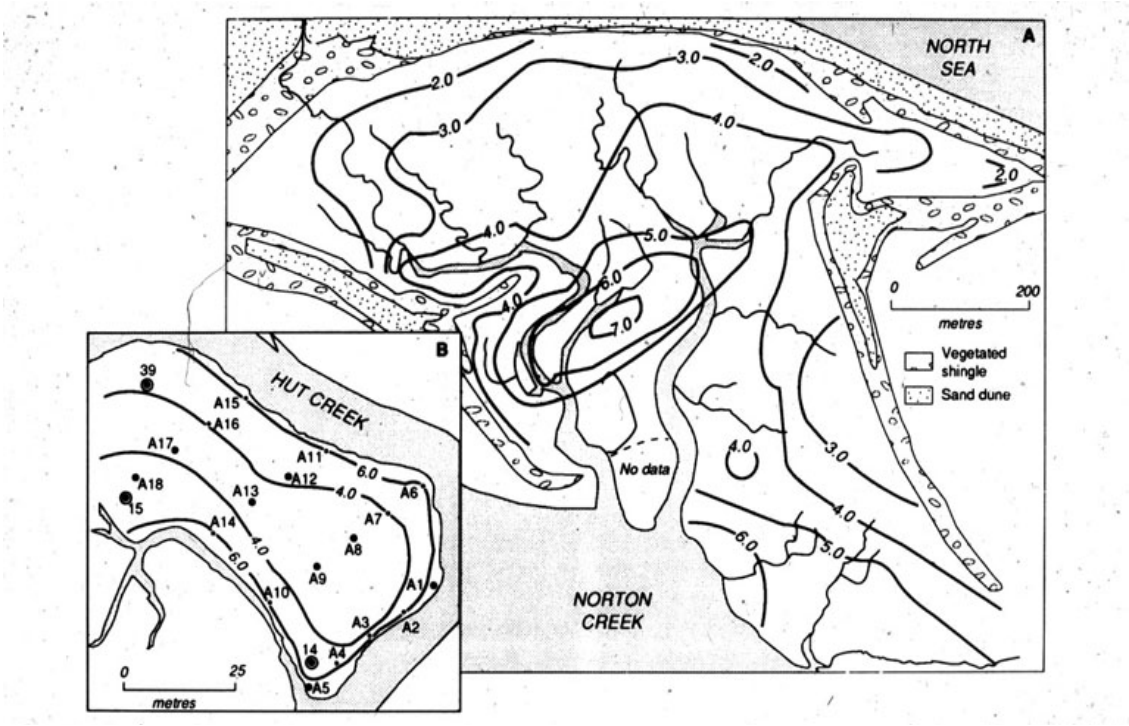

Figure 1 (A) Five year mean accretion isolines (1986-1991; mm a^{-1}) from extensive network (sites 1-83) of sand layer marker horizons, Hut Marsh, Scolt Head Island, N. Norfolk. (B) Five year mean accretion isolines for saltmarsh surface sites A1-A18 adjacent to Hut Creek (after French and Spencer 1993)

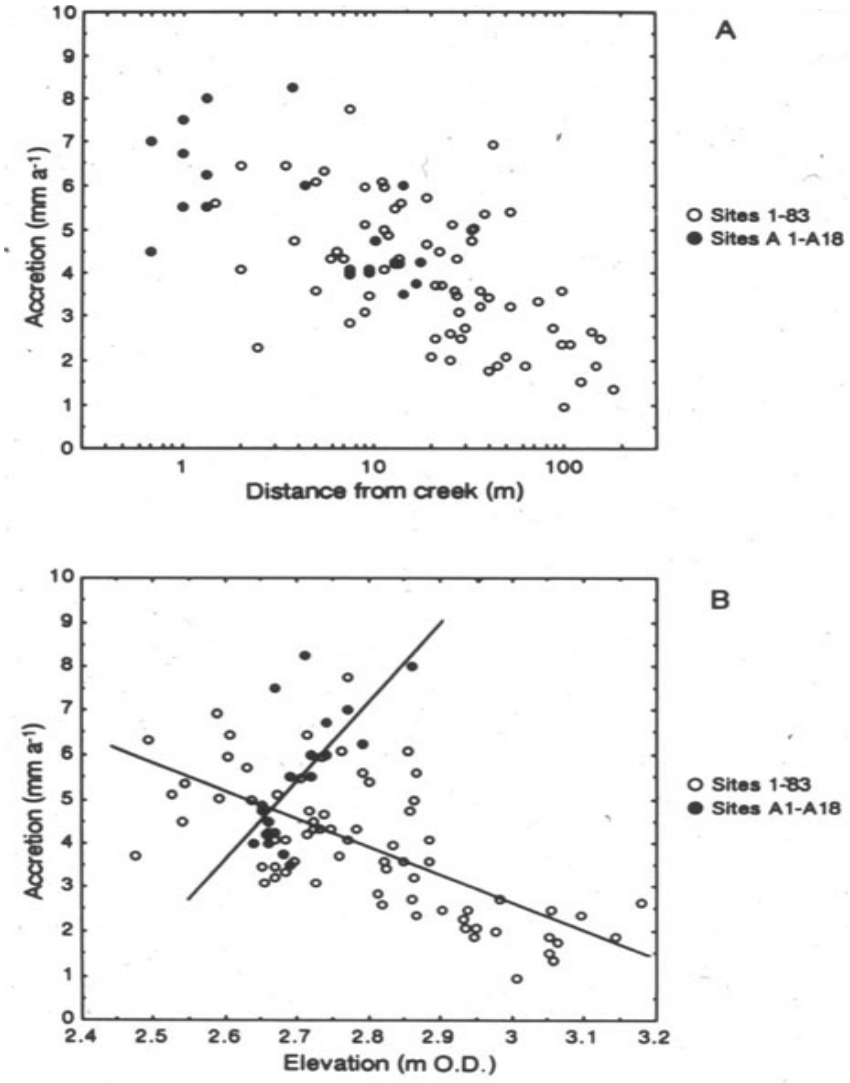

Figure 2 Five year mean accretion plotted against (A) distance to feeder creek and (B) surface elevation

Note: positive relationship of accretion to elevation in area adjacent to creek (sites A1-A18; see Figure 1 for position) and negative relationship at a marsh-wide scale (sites 1-83). (French and Spencer 1993)

Benefits from EstProc

Such studies sit in the EstProc framework of establishing the different time and space controls on estuarine margin processes and contribute to the discussion of linkages between such different scales.

Implementation of algorithm

The observed relationships should be used as a guideline for patterns of sedimentation in saltmarshes dominated by external inputs of mineral sediments delivered by dendritic creek systems. The presentation of data in the figure is illustrative rather than definitive.

Limits of applicability

Patterns of sedimentation and accretion change as marsh surfaces develop from broadly convex surfaces between creek systems relatively low in the tidal frame to horizontal surfaces (or slightly concave surfaces between creek bank levees) on 'mature' marshes

relatively high in the tidal frame. Hut Marsh is an example of a mature marsh and patterns of sedimentation and accretion observed in this system should not be transferred to marsh surfaces at earlier stages of development.

At-a-point measurements of surface elevation change using the Sedimentation-Erosion Table (SET) show *inter-annual* variations in elevation change which relate to both sediment supply and surface consolidation processes (Cahoon *et al.* 2000).

The example presented makes it clear that the question is not simply one of declining sedimentation rate away from a source. Many salt marshes on estuarine margins support tidal channels and therefore this case is appropriate in many estuarine settings. The example is illustrative of processes within saltmarshes and therefore relevant to understanding the dynamics of estuarine margins.

Gaps in knowledge

The establishment of sediment volume change through time for whole-marsh systems has yet to be satisfactorily achieved. Knowledge of such volumetric changes are necessary to establish the sediment demand of marsh systems at different stages of development and to investigate whether mature marsh systems will be able to adjust to changing sediment demands consequent upon near-future sea-level rise.

References

Cahoon, D., French, J.R., Spencer, T., Reed, D.J. and I Möller, I. 2000. Vertical accretion versus elevational adjustment in UK saltmarshes: An evaluation of alternative methodologies. in:- Coastal and estuarine environments: Sedimentology, geomorphology and geoarchaeology K. Pye and J.R.L. Allen (eds) London: Geological Society of London Special Publication 175, 223-238.

French, J.R. and Spencer, T. 1993. Dynamics of sedimentation in a tide-dominated backbarrier salt marsh, Norfolk, UK. Marine Geology 111, 315 - 331.

Reed, D.J., Spencer, T., Murray, A.L., French, J.R., and Leonard, L. 1999. Marsh surface sediment deposition and the role of tidal creeks: Implications for created and managed coastal marshes. Journal of Coastal Conservation 5, 81-90.

APPENDICES

Appendix 1

Project bibliography

The following reports and papers were produced directly with funding from the EstProc project. The outputs are listed by organisation.

HR Wallingford

Whitehouse, R.J.S. (2003). Estuary process research project linking hydrodynamics, sediments and biology (EstProc). Defra conference paper, 02.2.1 to 02.2.12.

Soulsby, R.L. and Clarke, S. (2004). Bed shear-stresses under combined waves and currents on smooth and rough beds. HR Wallingford report, TR137, Rev1.0.

Tozer, N.P., Grey, S.M. and Ellam, T.J. (2004). Wave modelling in estuaries with regard to changes in wave activity occurring over the tide, HR Wallingford Report TR141, May 2004.

Spearman, J.R., Baugh, J. and McCoy, M.J. (2004). Use of sub-grid approaches in the modelling of estuaries with salt marsh systems. HR Wallingford report, TR138, Rev1.0, January 2004.

Manning, A.J. (2004). The development of new algorithms to parameterise the mass settling flux of flocculated estuarine sediments. HR Wallingford report TR145, Rev1.0, August 2004.

Spearman, J. (2004). Note on the use of algorithms for modelling mud transport on tidal flats. HR Wallingford report TR144, Rev1.0, August 2004.

Baugh, J. (2004). Implementation of Manning algorithm for settling velocity in an estuarine numerical model. HR Wallingford report TR146, Rev 1.0, August 2004.

Proudman Oceanographic Laboratory

Lane, A. (2004). Bathymetric evolution of the Mersey Estuary, UK, 1906–1997: causes and effects. Estuarine, Coastal and Shelf Science, 59, 249–263.

Lane, A. and Manning, A. (2004). A Sticky Question. p25 in NERC Planet Earth. Spring edition, 2004.

Lane, A. (2004). The Dee, Mersey and Ribble estuaries (UK) – so near, yet so different, Extended abstract for PECS Conference, Merida, Mexico, October 2004.

Lane, A. (2004). Bathymetric evolution of the Mersey Estuary, UK, 1906–1997: causes and effects. Estuarine, Coastal and Shelf Science, 59, 249–263.

Lane, A. and Manning, A. (2004). A Sticky Question. p25 in NERC Planet Earth. Spring edition, 2004.

Lane, A. (2004). The Dee, Mersey and Ribble estuaries (UK) – so near, yet so different, Extended abstract for PECS Conference, Merida, Mexico, October 2004.

Lane, A. (2003). Dynamics, sediment transport and bathymetry in the Mersey Estuary. Paper at: RCEM 2003, 3rd IAHR Symposium on River, Coastal and Estuarine Morphodynamics.

Paphitis, D. and Collins, M.B. (2005). Sand grain threshold in relation to bed 'stress history: An experimental study. Sedimentology, 52, 827-838.

Prandle, D. and Lane, A. (2003). Equilibra between estuarine bathymetries and tides, river flow and sediment supply. 38th Defra Flood and Coastal Management Conference.

Prandle, D. (2003). How tides and saline intrusion control estuarine bathymetries. Keynote paper at: RCEM 2003, 3rd IAHR Symposium on River, Coastal and Estuarine Morphodynamics.

Prandle, D. (2003). Relationships between tidal dynamics and bathymetry in strongly convergent estuaries. Journal Physical Oceanography, 33(12), 2738–2750.

Prandle, D. (2004). Salinity intrusion in partially mixed estuaries. Estuaries, Coastal & Shelf Sciences, (59), 385–397.

Prandle, D. (2004). Sediment trapping, turbidity maxima and bathymetric stability in tidal estuaries: Journal Geophysical Research, V 109, C8.

Prandle, D. (2004). How tides and river flows determine estuarine bathymetries. To appear in: Progress in Oceanography.

Wolf, J. (2003). Parametric Modelling of waves in Liverpool Bay & Dee estuary. POL Internal Document No. 162.

University of Plymouth

List of papers either: formally acknowledging EstProc funding or other papers produced within EstProc project duration (2001-2004)

Bass, S.J.; **Manning, A.J.** and **Dyer, K.R.**, 2004. Preliminary findings from a study of the upper reaches of the Tamar Estuary, UK, throughout a complete tidal cycle: Part I. Linking sediment and hydrodynamic cycles. *In: J.P.-Y. Maa, L.P. Sanford and D.H. Schoellhamer (eds), Coastal and Estuarine Fine Sediment Processes, Proc. in Mar. Sci., INTERCOH-2003, Elsevier,* (in press).

Dyer, K.R., Bale, A.J., Christie, M.C., Feates, N., Jones, S., and **Manning, A.J.,** 2002. The turbidity maximum in a mesotidal estuary, the Tamar Estuary, UK. Part I: Dynamics of suspended sediment, In: J.C. Winterwerp and C. Kranenburg, (eds.), *Fine Sediment Dynamics in the Marine Environment* - Proc. in Mar. Sci. 5., Amsterdam: Elsevier, pp. 203-218, ISBN: 0-444-51136-9.

Dyer, K.R., Bale, A.J., Christie, M.C., Feates, N., Jones, S., and **Manning, A.J.**, 2002. The turbidity maximum in a mesotidal estuary, the Tamar Estuary, UK. Part II: The floc

properties, In: J.C. Winterwerp and C. Kranenburg, (eds.), *Fine Sediment Dynamics in the Marine Environment* - Proc. in Mar. Sci. 5., Amsterdam: Elsevier, pp. 219-232, ISBN: 0-444-51136-9.

Dyer, K.R.; Christie, M.C., and **Manning, A.J.**, 2004. The effects of suspended sediment on turbulence within an estuarine turbidity maximum. *Estuarine, Coastal and Shelf Science*, **59**, 237-248.

Gratiot, N. and **Manning, A.J.**, 2004. An experimental investigation of floc characteristics in a diffusive turbulent flow. In: P. Ciavola, M. B. Collins and C. Corbau (eds), Sediment Transport in European Estuaries, *Journal of Coastal Research Special Issue*, **SI 41**, (in press).

Lane, A. and **Manning, A.J.**, 2004. A sticky question: What controls the shape of estuaries? Natural Environmental Research Council (NERC) publications - Planet Earth, Spring 2004 edition, pp. 25 + front cover.

Maggi, F.; **Manning, A.J.** and **Winterwerp, J.C.**, 2004. Mud flocs – part 2, On the characterisation of floc geometry and floc dynamics. *Journal of Hydrological Processes* (*in press*).

Manning, A.J., (2004). The development of new algorithms to parameterise the mass settling flux of flocculated estuarine sediments, HR Wallingford Technical Report No. TR 145, 26 pp.

Manning, A.J., (2004). The observed effects of turbulence on estuarine flocculation. In: P. Ciavola and M. B. Collins (eds), *Sediment Transport in European Estuaries*, *J. Coast. Res.*, SI 41, 90-104.

Manning, A.J., (2004). Observations of the properties of flocculated cohesive sediment in three western European estuaries. In: P. Ciavola and M. B. Collins (eds), *Sediment Transport in European Estuaries*, *J. Coast. Res.*, SI 41, 70-81.

Manning, A. J.; Bass, S.J., Experimental and predictive modelling observations of cohesive sediment settling fluxes in high energy tidal estuarine environments, In: Tidalites: Tidal Sedimentology *Special Edition of Marine Geology* (*in press*).

Manning, A. J.; Bass, S.J., Observations of spectral mud floc properties during a tidal cycle in a macrotidal estuary, *Estuarine, Coastal and Shelf Science*, (*in preparation*).

Manning, A.J.; Bass, S.J. and **Dyer, K.R.**, 2004. Preliminary findings from a study of the upper reaches of the Tamar Estuary, UK, throughout a complete tidal cycle: Part II. *In-situ* floc spectra observations. *In: J.P.-Y. Maa, L.P. Sanford and D.H. Schoellhamer (eds), Coastal and Estuarine Fine Sediment Processes, Proc. in Mar. Sci., INTERCOH-2003, Elsevier,* (in press).

Manning, A.J. and **Dyer, K.R.**, 2002. The use of optics for the in-situ determination of flocculated mud characteristics, *Journal of Optics A: Pure and Applied Optics*, Institute of Physics Publishing, **4**, S71-S81.

Manning, A.J. and **Dyer, K.R.**, 2002. A comparison of floc properties observed during neap and spring tidal conditions, In: J.C. Winterwerp and C. Kranenburg, (eds.), *Fine Sediment Dynamics in the Marine Environment* - Proc. in Mar. Sci. 5., Amsterdam: Elsevier, pp. 233-250, ISBN: 0-444-51136-9.

Manning, A.J. and **Dyer, K.R.,** 2004. Mass settling flux of fine sediments: measurements and predictions. *Journal of Geophysical Research*, (in press).

Manning, A. J.; **Dyer, K.R.** and Bass, S.J., Neap and spring tidal floc population variations observed in a mesotidal estuary using the video based INSSEV instrument, In: Tidalites: Tidal Sedimentology *Special Edition of Marine Geology* (*in press*).

Manning, A.J., Dyer, K.R., Lafite, R. and Mikes, D., (2004). Flocculation measured by video based instruments in the Gironde Estuary during the European Commission SWAMIEE project. In: P. Ciavola and M. B. Collins (eds), *Sediment Transport in European Estuaries*, *J. Coast. Res.*, SI 41, 58-69.

Manning, A. J.; **Friend, P.L.**; Prowse, N. and Amos, C.L., A Study of Medway Estuary (UK) Natural Mud Floc Properties Using a Laboratory Miniflume, In: EC BIOFLOW project *Special Edition of Cont. Shelf Res*. (*under review*).

Manning, A.J.; Gratiot, N. and **Dyer, K.R.**, An study of floc characteristics in dilute mud suspensions using a laboratory diffusive turbulent grid tank, Marine Geology (*submitted*).

Mory, M., Gratiot, N., **Manning, A.J.**, and Michallet, H., 2002. CBS layers in a diffusive turbulence grid oscillation experiment, In: J.C. Winterwerp and C. Kranenburg, (eds.), *Fine Sediment Dynamics in the Marine Environment* - Proc. in Mar. Sci. 5., Amsterdam: Elsevier, pp.139-154, ISBN: 0-444-51136-9.

Petersen, O., Vested, H.J., **Manning, A.J.**, Christie, M.C., and **Dyer, K.R.**, 2002. Numerical modelling of mud transport processes in the Tamar Estuary, In: J.C. Winterwerp and C. Kranenburg, (eds.), *Fine Sediment Dynamics in the Marine Environment* - Proc. in Mar. Sci. 5., Amsterdam: Elsevier, pp. 643-654, ISBN: 0-444-51136-9.

Winterwerp, J.C., Bale, A.J., Christie, M.C., **Dyer, K.R.**, Jones, S., Lintern, D.G., **Manning, A.J.**, and Roberts, W., 2002. Flocculation and settling velocity of fine sediment, In: J.C. Winterwerp and C. Kranenburg, (eds.), *Fine Sediment Dynamics in the Marine Environment* - Proc. in Mar. Sci. 5., Amsterdam: Elsevier, pp. 25-40, ISBN: 0-444-51136-9.

Conference Abstracts:

Manning, A.J., and Bass, S.J., 2004. Experimental and predictive modelling observations of cohesive sediment settling fluxes in high energy tidal estuarine environments. Tidalites International Conferences on Tidal Sedimentology, University of Copenhagen, Denmark, August 2004.

Manning, A.J., 2004. A review of the recent advances in the study of estuarine mud flocculation in European tidal waters. Tidalites International Conferences on Tidal Sedimentology, University of Copenhagen, Denmark, August 2004.

Graham, G., and **Manning, A.J.**, 2004. Floc Characteristics & Mass Settling Flux Modifications During Marsh Inundation: Initial Laboratory Investigations, Poster presentation at the Biennial Challenger Society for Marine Science International Conference 2004 held at University of Liverpool and *the NERC* Proudman Oceanographic Laboratory.

Graham, G., **Manning, A.J.**, **Friend, P.L.**, Thompson, C. and Amos, C.L., 2004. The influence of Spartina anglica on the flocculation of cohesive sediments: a laboratory investigation, Poster presentation, Proceedings of the 3rd EC funded BIOFLOWresearch project Workshop, Venice International University, Venice, Italy.

Manning, A.J., Bass, S.J. and **Dyer, K.R.**, 2003. Preliminary findings of a study of the upper reaches of the Tamar Estuary, UK, throughout a complete tidal cycle: Part I. The in-situ floc spectra observations, Oral presentation at the 7th International Conference on Cohesive Sediment Transport - INTERCOH, Virginia Institute of Marine Science, Virginia, USA, October 2003.

Bass, S.J., **Manning, A.J.** and **Dyer, K.R.**, 2003. Preliminary findings of a study of the upper reaches of the Tamar Estuary, UK, throughout a complete tidal cycle: Part II. Linking sediment and hydrodynamic cycles, Oral presentation at the 7th International Conference on Cohesive Sediment Transport - INTERCOH, Virginia Institute of Marine Science, Virginia, USA, October 2003.

Manning, A.J., 2002. The effects of turbulence on estuarine flocculation, Key Note Speaker at the International Conference on Sediment Transport in European Estuaries (University of Ferrara, Italy), September 2002.

Manning, A.J., 2002. Observations of the properties of flocculated cohesive sediment in three western European estuaries, Poster presentation at the International Conference on Sediment Transport in European Estuaries (University of Ferrara, Italy), September 2002.

Manning, A.J., **Dyer, K.R.**, Lafite, R. and Mikes, D., 2002. Flocculation measured by video based instruments in the Gironde Estuary during the European Commission SWAMIEE project, Oral presentation at the International Conference on Sediment Transport in European Estuaries (University of Ferrara, Italy), September 2002.

Manning, A.J. and **Dyer, K.R.**, 2002. The use of optics for the in-situ determination of flocculated mud characteristics, Oral presentation at UNDERWATER OPTICS 6 scientific workshop, 9, The Institute of Physics (London), 2001.

Reports

Manning, A.J., 2004. The development of new algorithms to parameterise the mass settling flux of flocculated estuarine sediments, HR Wallingford Technical Report No. TR 145, 26 pp.

Bass, S.J., and **Manning, A.J.**, 2004. Project: Cycles in estuarine hydrodynamic conditions in relation to cycles in near-bed flocculating suspensions, NERC Research Grant & Fellowship Final Report for Award Ref Number: NER/M/S/2002/00108, April 2004.

Bass, S.J., and **Manning, A.J.**, 2004. Project: Cycles in estuarine hydrodynamic conditions in relation to cycles in near-bed flocculating suspensions, Digital on-line report, NERC Research Outputs Database (ROD) input for Award Ref Number: NER/M/S/2002/00108, March 2004.

Internet Websites

EstProc website link placed of following URL: www.coastalprocesses.org

This is the home page for the School of Earth, Ocean and Environmental Sciences, University of Plymouth's Coastal Processes Research Group which is headed by Prof. David Huntley.

St Andrews University, Gatty Marine Laboratory

Defew, E.C., Tolhurst, T.J. & Paterson, D.M. (In press) Site-specific feature influence sediment stability of intertidal flats. *Hydrology & Earth System Science*.

Defew, E.C., Tolhurst, T.J., Paterson, D.M. & Hagerthey, S.E. (In press). Can the stability of intertidal mudflats be predicted from proxy parameters? An *in situ* investigation. *Estuarine Coastal Sciences Association*.

ABP Marine Environmental Research

ABPmer. (2004a). Hydrodynamic cellular models of tidal regimes. ABP Marine Environmental Research report R.1091.

ABPmer. (2004b). Modelling moveable seabed roughness under random waves. ABP Marine Environmental Research report R1092.

ABPmer. (2004c). A study into the significance of sediment data in the prediction of invertebrate biology on the Humber estuary. ABP Marine Environmental Research report R.1077.

WL | Delft Hydraulics

Bouma, T.J., De Vries, M.B., Low, E., Kusters, L., Herman, P.M.J., Tánczos, I.C., Hesselink, A., Temmerman, S., Meire, P., van Regenmortel, S. (2005). Hydrodynamic measurements on a mudflat and in salt marsh vegetation: identifying general relationships for habitat characterizations. Hydrobiologia. 540. 259-274.

Bouma, T.J., De Vries, M.B., Low, E., Peralta, G., Tánczos, I.C., van de Koppel, J., Herman, P.M.J. (2005). Trade-offs related to ecosystem engineering: A case study on stiffness of emerging macrophytes. Ecology 86, 2187-2199.

Knaapen, M.A.F., H. Holzhauer, S.J.M.H. Hulscher , M.J. Baptist, M.B. de Vries, M. van Ledden, M. (2003). On the modelling of biological effects on morphology in estuaries and seas. In (Ed.), Proceedings third IAHR Symposium on River, Coastal and Estuarine Morphodynamics 2003, pp 773-783.

Mol, A., (2004). Wave attenuation by vegetation. WL | Delft Hydraulics report, Z2837/Z3040, March 2004.

Winterwerp, J.C. (2004). The transport of fine sediment in the Humber Estuary. WL | Delft Hydraulics research report, Z3040, January 2004.

Plymouth Marine Laboratory

Roast, S.D., Widdows, J., Pope, N.D. and Jones, M.J. (2004). Sediment / biota interactions: the role of mysid feeding behaviour on turbidity and sediment erodibility. Marine Ecology Progress Series (in press).

Romano, C., Widdows, J., Brinsley, M.D. and Staff, F.J. (2003). Impact of Enteromorpha on near-bed currents and sediment dynamics: Flume studies. *Marine Ecology Progress Series* 256, 63-74.

Uncles, R.J., Bale, A.J., Brinsley, M.D., Frickers, P.E., Harris, C., Lewis, R.E., Pope, N.D., Staff, F.J., Stephens, J.A., Turley, C.M., Widdows, J. 2003. Intertidal mudflat properties, currents and sediment erosion in the partially mixed Tamar estuary, UK. Ocean Dynamics, 53, 239-251.

Uncles, R.J., Stephens, J.A., Harris, C. In press (a). Runoff and tidal influences on the estuarine turbidity maximum of the highly turbid Humber Estuary, UK. Marine Geology.

Uncles, R.J., Stephens, J.A., Law, D.J. In press (b). Turbidity maximum in the macrotidal, highly turbid Humber Estuary, UK: flocs, fluid mud, stationary suspensions and tidal bores. Estuarine, Coastal and Shelf Science.

Uncles, R.J., Stephens, J.A., Harris, C. In press (c). Properties of suspended sediment in the estuarine turbidity maximum of the highly turbid Humber Estuary, UK. Ocean Dynamics.

Widdows, J., (2001). The inter-tidal zone. In: Huntley DA, Leeks GJL, Walling DE (eds) Land Ocean Interaction: Measuring and modelling fluxes from river basins to coastal seas. IWA Publishing, London, p 184-208.

Romano, C., Widdows, J., Brinsley, M.D. and Staff, F.J. (2003). Impact of Enteromorpha on near-bed currents and sediment dynamics: Flume studies. *Marine Ecology Progress Series* 256, 63-74.

Widdows, J., Wood, R.G., Pope, N.D., Brinsley, M.D. and Staff, F.J. (2003). Impact of biota and dredged material on intertidal sediment dynamics. Defra Final Contract Report (AE0259) 23pp.

Widdows, J., Blauw, A., Heip, C.H.R., Herman, P.M.J., Lucas, C.H., Middelburg, J.J., Schmidt, S., Brinsley, M.D., Twisk, F. and Verbeek, H. (2004). Role of physical and biological processes in sediment dynamics (sedimentation, erosion and mixing) of a tidal flat in Westerschelde estuary, S.W. Netherlands. Marine Ecology Progress Series, 274, 41-56.

Widdows, J., Brinsley, M.D. and Elliott, M. (1998). Use of *in situ* flume to quantify particle flux (deposition rate and sediment erosion) for an intertidal mudflat in relation to changes in current velocity and benthic macrofauna. In: Black KS, Paterson DM, Cramp A (eds) Sedimentary processes in the intertidal zone. Geological Society, Special Publications, London, p 85-97.

Widdows, J., Brinsley, M.D., Salkeld, P.N. and Lucas, C.H. (2000). Influence of biota on spatial and temporal variation in sediment erodibility and material flux on a tidal flat (Westerschelde, Netherlands). Marine Ecology Progress Series 194:23-37.

Wood, R. & Widdows, J. 2002. A model of sediment transport over an intertidal transect, comparing the influences of biological and physical factors. *Limnology and Oceanography* 47, 848-855.

University of Cambridge, Cambridge Coastal Research Unit

Cahoon, D. R., Spencer, T. and Santilan, N. (in press) 'Toward a global model of coastal wetland response to sea level rise'. In:- Verhoeven, J.T.A., Beltman, B., Bobbink, R. and Whigham, D.F. (eds) *Wetlands as a natural resource. Volume 1. Wetlands and natural resource management*. Berlin: Springer-Verlag

Elsner, P. H., Smith, G. M., Möller, I. and Spencer, T. (2003) 'Multi-temporal airborne imaging spectroscopy – A novel approach for monitoring intertidal sediment dynamics'. Abstracts Volume, *Coastal Sediments 2003 – Crossing Disciplinary Boundaries*, Clearwater Beach, Florida, USA, May 18-23, 484-485.

McRobie, A., Spencer, T. and Gerritsen, H. (eds) (2005) The Big lood: North Sea storm surge. Philosophical Transactions of the Royal Society 363A, 1261-1491.

Möller, I. (2002): 'Land Reclamation from Seas'. In: Munn, T. (ed.) *Encyclopedia of Global Environmental Change*. Volume 3: Douglas, I. (ed.) *Causes and consequensces of global environmental change*. John Wiley & Sons Ltd., 424-430.

Möller, I. and Spencer, T. (2003) 'Wave transformations over mudflat and saltmarsh surfaces on the UK East coast – Implications for marsh evolution'. *Proceedings of the International Conference on Coastal Sediments 2003*. Corpus Christi, Texas: World Scientific Publishing Corp. and East Meets West Productions.

Möller, I. and Spencer, T. (2002) 'Wave dissipation over macro-tidal saltmarshes: Effects of marsh edge typology and vegetation change'. *Journal of Coastal Research* SI36, 506-521.

Möller, I., Spencer, T., and Rawson, J. (2002) 'Spatial and temporal variability of wave attenuation over a UK East-coast saltmarsh'. *Proceedings of the 38th International Conference on Coastal Engineering*, Cardiff, July 2002. London: Thomas Telford Publishing, 362.

Smith, G.M., Thomson, A.G., Möller, I. and Kromkamp, J.C. (2004) 'Using hyperspectral imaging for the assessment of mudflat surface stability'. *Journal of Coastal Research* 20, 1165-1175.

Smith, G. M., Thomson, A. G., Möller, I. and Kromkamp, J. C., (in press) 'Hyperspectral imaging for mapping sediment characteristics'. *Estuarine and Coastal Sciences Association Bulletin.*

Turner, R., Möller, I., Spencer, T. and Booij, N. (2003). Application of the SWAN model to vegetated surfaces. Report prepared by Cambridge Coastal Research Unit for Defra contract number FD1905. October 2003.

University of Southampton, School of Ocean and Earth Sciences

Friend, P.L., Collins, M.B. and Holligan, P.M. (2003). Day-night variation of intertidal flat sediment properties in relation to sediment stability. Estuarine, Coastal and Shelf Science, 58, 663-675.

Paphitis, D. and Collins, M.B. (2005). Sand grain threshold in relation to bed 'stress history: An experimental study. Sedimentology, 52, 827-838.

Digital Hydraulics Holland

Booij, N. (2004). A model for wave dissipation due to flexible vegetation. Report prepared for EstProc (included in EstProc Consortium Final Report FD1905/TR3).

Centre for Environment, Fisheries and Aquaculture

Bolam, S.G. (2003). Spatial patterns of estuarine macrobenthic assemblages: relationships with hydrodynamic regime. Report prepared by CEFAS for EstProc project. Report No: FD1905/CEFAS1. March 2003.

Bolam, S.G. (2004). Sediment stability of fine-grained beneficial use schemes: the role of recolonizing macrofaunal communities. Report prepared by CEFAS for EstProc project. Report No: FD1905/CEFAS2. June 2004.

Schratzberger, M. (2004). The role of meiofauna in estuarine processes. Report prepared by CEFAS for EstProc project. Report No: FD1905/CEFAS3. August 2004.

Appendix 2

Contact details for EstProc research project team

HR Wallingford
Richard Whitehouse/Richard Soulsby/Mike Dearnaley/Jeremy Spearman/Nigel Tozer/Alison Houghton/ Stephen Grey
Email: r.whitehouse@hrwallingford.co.uk ; rls@hrwallingford.co.uk ; mpd@hrwallingford.co.uk
Tel: +44 (0)1491 835381
www.hrwallingford.co.uk

Proudman Oceanographic Laboratory
David Prandle/Andrew Lane/Judith Wolf
Email: davidprandle@hotmail.co.uk ; ale@pol.ac.uk
Tel: +44 (0)151 795 4800
www.pol.ac.uk

University of Plymouth
Keith Dyer/Andrew Manning
Email: keith-r-dyer@supanet.com ; andymanning@yahoo.com
Tel: + 44 (0)1823 401 125
www.coastalprocesses.org

St Andrews University, Gatty Marine Laboratory
David Paterson/Kevin Black/Emma Defew
Email: d.paterson@st-andrews.ac.uk
Tel: +44 (0)1334 463 467
www.st-andrews.ac.uk/~serg/

ABP Marine Environmental Research
Ian Townend/Paul Norton/John Harris/Chris Jackson/Richard Swift
Email: itownend@abpmer.co.uk ; pnorton@abpmer.co.uk
Tel: +44 (0)2380 711840
www.abpmer.co.uk

WL | Delft Hydraulics
Han Winterwerp/Dano Roelvink/Mindert de Vries/Andries Roelfzema
Email: Han.Winterwerp@wldelft.nl ; mindert.devries@wldelft.nl
Tel: +31 152 858 813
www.wldelft.nl

Plymouth Marine Laboratory
Reg Uncles/John Widdows
Email: rju@pml.ac.uk ; JWID@pml.ac.uk
Tel: +44 (0)1752 633441
www.pml.ac.uk

University of Cambridge, Cambridge Coastal Research Unit
Tom Spencer/Iris Moeller/Roz Turner
Email: ts111@cam.ac.uk ; im10003@cam.ac.uk
Tel: +44 (0) 1223 339775
http://ccru.geog.cam.ac.uk/

University of Southampton, School of Ocean and Earth Sciences
Mike Collins/Doros Paphitis/Patrick Friend
Email: mbc@noc.soton.ac.uk ; plf1@noc.soton.ac.uk
Tel: +44 (0) 23 8059 6666
www.noc.soton.ac.uk

Digital Hydraulics Holland
Leo Holthuijsen/Nico Booij
Email: info@digitalhydraulics.com
Tel: + 31 10 442 4768
www.digitalhydraulics.com

Centre for Environment, Fisheries and Aquaculture
Stefan Bolam/Michaela Schratzberger
Email: s.g.bolam@cefas.co.uk
Tel: +44 (0) 1621 787200
www.cefas.co.uk

Contact information is also held at the project website www.estproc.net

PB 11546

Nobel House,
17 Smith Square,
London SW1P 3JR

www.defra.gov.uk